

ISSN en trámite



# Geofísica Internacional

Revista Trimestral Publicada por el Instituto de Geofísica de la  
Universidad Nacional Autónoma de México



México

Volume 56 Number 3  
July - September  
2017

# — Geofísica Internacional —

Dr. Hugo Delgado Granados  
**Director of Instituto de Geofísica**

Dra. Xyoli Pérez Campos  
**President of Unión Geofísica Mexicana**

## Editor Chief

Dr. Servando De la Cruz-Reyna  
Instituto de Geofísica, UNAM  
[sdelacrr@geofisica.unam.mx](mailto:sdelacrr@geofisica.unam.mx)

## Technical Editor

Mtra. Andrea Rostan Robledo  
Instituto de Geofísica, UNAM  
[arostan@igeofisica.unam.mx](mailto:arostan@igeofisica.unam.mx)

## Editorial Board

Donald Bruce Dingwell  
Earth and Environment  
Ludwig Maximilian University of Munich,  
Germany

Eric Desmond Barton  
Departamento de Oceanografía  
Instituto de Investigaciones Marinas, Spain

Jorge Clavero  
Amawta Consultores, Chile

Gerhardt Jentzsch  
Institut für Geowissenschaften  
Friedrich-Schiller-Universität Jena, Germany

Peter Malischewsky  
Institut für Geowissenschaften  
Friedrich-Schiller-Universität Jena, Germany

François Michaud  
Géosciences Azur  
Université Pierre et Marie Curie, France

Olga Borisovna Popovicheva  
Scobeltzine Institute of Nuclear Physics  
Moscow State University, Rusia

Jaime Pous  
Facultad de Geología  
Universidad de Barcelona, Spain

Joaquín Rui  
UA Science  
University of Arizona, United States

Angelos Vourlidas  
Solar Physics Branch  
NASA Goddard Space Flight Center, United States

Théophile Ndougsa Mbarga  
Department of Physics  
University of Yaounde I, Cameroon

Associate Editors  
José Agustín García Reynoso  
Atmospheric Science Centro de Ciencias de la  
Atmósfera UNAM, Mexico

Tereza Cavazos  
Atmospheric Science  
Departamento de Oceanografía Física CICESE,  
Mexico

Dante Jaime Morán-Zenteno  
Geochemistry  
Instituto de Geología, UNAM, Mexico

Margarita López  
Geochemistry  
Instituto de Geología UNAM, Mexico

Avto Gogichaisvili  
Geomagnetism And Paleomagnetism  
Instituto de Geofísica UNAM, Mexico

Jaime Urrutia-Fucugauchi  
Geomagnetism And Paleomagnetism  
Instituto de Geofísica, UNAM, Mexico

Felipe I. Arreguín Cortés  
Hydrology  
Instituto Mexicano de Tecnología del Agua IMTA,  
Mexico

William Lee Bandy  
Marine Geology And Geophysics  
Instituto de Geofísica UNAM, Mexico

Fabian García-Nocetti  
Mathematical And Computational  
Modeling  
Instituto de Investigaciones en Matemáticas  
Aplicadas y en Sistemas UNAM, Mexico

Graciela Herrera-Zamarrón  
Mathematical Modeling  
Instituto de Geofísica, UNAM, Mexico

Ismael Herrera Revilla  
Mathematical And Computational  
Modeling  
Instituto de Geofísica UNAM, Mexico

Rene Chávez Segura  
Near-Surface Geophysics  
Instituto de Geofísica UNAM, Mexico

Juan García-Abdeslem  
Near-Surface Geophysics  
División de Ciencias de la Tierra CICESE, Mexico

Alec Torres-Freyermuth  
Oceanography  
Instituto de Ingeniería, UNAM, Mexico

Jorge Zavala Hidalgo  
Oceanography  
Centro de Ciencias de la Atmósfera UNAM,  
Mexico

Shri Krishna Singh  
Seismology  
Instituto de Geofísica, UNAM, Mexico

Xyoli Pérez-Campos  
Seismology  
Servicio Sismológico Nacional, UNAM, Mexico

Blanca Mendoza Ortega  
Space Physics  
Centro de Ciencias de la Atmósfera, UNAM,  
Mexico

Inez Staciari Batista  
Space Physics  
Pesquisador Senior Instituto Nacional de Pesquisas  
Espaciais, Brazil

Roberto Carniel  
Volcanology  
Laboratorio di misure e trattamento dei segnali  
DPIA - Università di Udine, Italy

Miguel Moctezuma-Flores  
Satellite Geophysics  
Facultad de Ingeniería, UNAM, Mexico

## Assistance

Elizabeth Morales Hernández,  
Management  
[eliedit@igeofisica.unam.mx](mailto:eliedit@igeofisica.unam.mx)



**GEOFÍSICA INTERNACIONAL**, Año 56, Vol. 56, Núm. 3, julio - septiembre de 2017 es una publicación trimestral, editada por la Universidad Nacional Autónoma de México, Ciudad Universitaria, Alcaldía Coyoacán, C.P. 04150, Ciudad de México, a través del Instituto de Geofísica, Circuito de la Investigación Científica s/n, Ciudad Universitaria, Alcaldía Coyoacán, C.P. 04150, Ciudad de México, Tel. (55)56 22 41 15. URL: <http://revistagi.geofisica.unam.mx>, correo electrónico: [revistagi@igeofisica.unam.mx](mailto:revistagi@igeofisica.unam.mx). Editora responsable: Andrea Rostan Robledo. Certificado de Reserva de Derechos al uso Exclusivo del Título: 04-2022-081610251200-102, ISSN: en trámite, otorgados por el Instituto Nacional del Derecho de Autor (INDAUTOR). Responsable de la última actualización Saúl Armendáriz Sánchez, Editor Técnico. Fecha de la última modificación: 30 de junio 2017, Circuito de la Investigación Científica s/n, Ciudad Universitaria, Alcaldía Coyoacán, C.P. 04150, Ciudad de México.

El contenido de los artículos es responsabilidad de los autores y no refleja el punto de vista de los árbitros, del Editor o de la UNAM. Se autoriza la reproducción total o parcial de los textos siempre y cuando se cite la fuente completa y la dirección electrónica de la publicación.



Esta obra está bajo una Licencia Creative Commons Atribución-NoComercial-SinDerivadas 4.0 Internacional.

## Contents

Integration of geoelectric and geochemical data in the evaluation of natural attenuation in a diesel contaminated site in São Manuel (Brazil).

**César A. Moreira, Livia Portes Innocenti Helene, Ariane R. P. Côrtes**

229

---

New insight on the recent instrumental seismic activity along the Serghaya fault, Syria.

**Abdul-Wahed M. K., J. Asfahani**

243

---

Paleoseismological uncertainty estimation in the Acambay region, Central Mexico.

**Quetzalcoatl Rodríguez-Pérez, F. Ramón Zúñiga, Pierre Lacan**

255

---

Observations of remotely triggered seismicity in Salton Sea and Coso geothermal regions, Southern California, USA, after big (MW>7.8) teleseismic earthquakes.

**Raúl R. Castro, Robert Clayton, Egill Hauksson, Joann Stock**

269

---

Paleomagnetism and Aeromagnetic Survey From Tancitaro Volcano (Central Mexico) - Paleo-Secular Variation at Low Latitudes During the Past 1 Ma.

**Rafael García-Ruiz, Avto Gogutchiaichvili, Hector-López Loera, Miguel Cervantes-Solano, Jaime Urrutia-Fucugauchi, Juan Morales-Contreras, Rafael Maciel-Peña, José Rosas-Elguera**

287

---

Evaluation of geochemical data by two different XRF spectrometers in sediments from the Santiaguillo Basin (state of Durango, Mexico).

**Jesús David Quiroz-Jiménez, Priyadarsi D. Roy**

305

---

## Integration of geoelectric and geochemical data in the evaluation of natural attenuation in a diesel contaminated site in São Manuel (Brazil)

César A. Moreira\*, Lívia Portes Innocenti Helene and Ariane R. P. Côrtes

Received: April 13, 2016; accepted: May 24, 2017; published on line: July 01, 2017

### Resumen

La geofísica es de gran importancia en relación con los análisis químicos en el proceso de diagnóstico de la contaminación en el medio geológico. En este trabajo se presentan los resultados de los métodos geofísicos de Resistividad Eléctrica y Polarización Inducida en un área contaminada por diesel debido a un accidente ferroviario ocurrido en 1999 en el que no se implementaron sistemas de remediación. Los procesos de atenuación natural prevalecientes en la zona resultaron en una reducción gradual de los niveles de hidrocarburos en las aguas subterráneas, como lo demuestra una serie histórica de análisis. La disolución y neoformación mineral son productos de este proceso que en la disponibilidad de elementos como Fe y Mn en suelos tropicales, a menudo resultan en la cristalización de sulfuro. Perfiles 2D y los modelos geofísicos 3D revelan una zona central de alta resistividad y alta capacidad de carga en un área con remanentes de contaminación cuantificados en 2008, asociados a hidrocarburos residuales. Además, los datos de carga elevada proporcionan una visión general de la mineralización del hidrocarburo como resultado de su degradación. Los datos indican la posibilidad de utilizar estos métodos como herramienta en sistemas de remediación de contaminación por hidrocarburos, por la posibilidad de realizar investigaciones sobre suelos secos y subterráneos, además de monitorear la mineralización de metales, productos relacionados con la degradación de hidrocarburos en el entorno geológico.

Key words: hidrocarburos, atenuación natural, resistividad eléctrica, cargabilidad.

### Abstract

Geophysics is a very relevant investigation tool in conjunction with chemical analysis, during the diagnosis and monitoring of contamination in the geological environment. This paper presents the results of DCdefine resistivity and Induced Polarization geophysical methods in an area contaminated by diesel due to a railway accident that occurred in 1999 in which no remediation systems were implemented. The processes of natural attenuation prevailing in the area resulted in gradual reduction of the levels of hydrocarbons in groundwater, as demonstrated by a historic series of analyses. The dissolution and neoformation mineral are products of this process that in the availability of elements such as Fe and Mn in tropical soils, often result in the crystallization of sulphide. 2D profiles and 3D geophysical models reveal a central zone of high resistivity and high chargeability in an area with remnants of contamination quantified in 2008, associated to residual hydrocarbons. Besides, the high chargeability data provides an overview of the mineralization of the hydrocarbon as a result from its degradation. The data indicates the possibility of using these methods as an auxiliary tool in systems for remediation of contamination by hydrocarbons, by the possibility of investigations into dry soil and groundwater, and in monitoring metal mineralization, products related to the degradation of hydrocarbons in the geological environment.

Palabras clave: hydrocarbon, natural attenuation, resistivity, chargeability.

C. A. Moreira\*  
Departamento de Geologia Aplicada  
Instituto de Geociências e Ciências Exatas  
Univ. Estadual Paulista  
Av. 24-A, 1515, Bela Vista  
ZIP 13506-900, Rio Claro  
São Paulo State, Brazil

\*Corresponding author: [moreirac@rc.unesp.br](mailto:moreirac@rc.unesp.br)

L. Portes Innocenti Helene  
A. R. P. Côrtes  
Instituto de Geociências e Ciências Exatas  
Univ. Estadual Paulista  
Av. 24-A, 1515, Bela Vista  
ZIP 13506-900, Rio Claro  
São Paulo State, Brazil

## Introduction

Contemporaneous with the process of economic development, contamination of the environment occurs as a result of lack of planning and inadequate management of raw materials, products and hazardous waste which, at concentrations above the recommended values, pose risks to health, to the quality of life and to the environment.

The logistics of hydrocarbons transportation in southeastern Brazil involves oil pipelines linking production fields to refining plants, which subsequently make use of highways for short distances and railroads for long distances. Rail transport is particularly relevant due to the possibility to move large volumes at relatively low cost. In this context, railway accidents often result in the contamination of great extent and significant environmental impact. Brazilian railways belong to the Brazilian Federal Government and are operated by private companies through a concession system.

The origin of the contamination of soil and water environments by hydrocarbons usually occurs due to transport accidents, breakage of pipes or improper storage. The main groups of contaminants found in these areas are the aromatic solvents, represented by BTEX compounds (benzene, toluene, ethylbenzene and xylenes), polycyclic aromatic hydrocarbons (PAH), chlorinate solvents and metals.

The groundwater contamination by organic chemical products is a recurring issue. Given the variability in terms of density and solubility in water, leakage from the surface may form contamination plumes and turn the groundwater a non-potable resource for human consumption.

For a long time the contamination of soil and groundwater has been neglected due to the difficulty of its characterization. When in contact with the physical environment, the transport of organic contaminants can be modeled according to two stages. The first comprises all those that occur entirely above the water level in the vadose zone; the second considers the transport processes inside the aquifer, soluble/dissolved or insoluble/supernatant, characterized by means of chemical analysis of water samples from monitoring wells (Sara, 2003; Berkowitz *et al.*, 2008).

Investigation techniques through direct methods such as physical and chemical analysis

of samples are common in the diagnosis of these areas, given the possibility of quantifying the levels (Redd and Adams, 2015). The main disadvantage of this procedure is its sparse sampling and poor representation in spatial terms, in a condition where the analyzed object is mobile and dynamic.

Particularly in the context of contamination by hydrocarbons that occurred several years ago, changes in terms of content, with dispersion, dilution and degradation of the compounds by the action of various agents present in the geological environment are expected. In many cases of areas contaminated by hydrocarbons, reduction of levels occurs without remedial actions. This natural attenuation comprises a set of remediation processes of contamination by hydrocarbons in the geological environment, through the action of physical, chemical and biological processes (Alvarez and Illman, 2006).

The degradation of contaminants by the action of microorganisms, is one of the main mechanisms responsible for the consumption of contaminants with long periods of residence in the environment. The efficiency of this process depends on a combination of factors such as the presence of electrical receptors ( $O_2$ ,  $SO_2^{-4}$ ,  $Fe^{+3}$ ,  $Mn^{+4}$ ,  $NO^{-3}$ ), adequate conditions of pH, Eh, temperature and low levels of contamination (Suthersan and Paine, 2005; Twardowska *et al.*, 2006; Romero-Zerón, 2012).

This process is specifically important in the degradation of hydrocarbons, which may be converted by organisms found in nearly all environments. Various BTEX compounds can be biodegraded under environmental conditions (Alvarez and Illman, 2006, Bhandari *et al.*, 2007). The generation of organic acids, dissolution and mineral neof ormation are consequences of this process.

The use of geophysics as a noninvasive investigation tool, with low cost and wide coverage in spatial and temporal terms, is used increasingly in recent years by supervisory agencies as a diagnostic tool in the management of contaminated sites (Sara, 2003; Knödel *et al.*, 2007). Electrical and electromagnetic geophysical methods are particularly relevant in this type of investigation due to the frequent contrast in physical properties between contaminated and uncontaminated soil or rock

Several studies demonstrate the effectiveness, benefits and limitations when applied in the diagnosis and geophysical monitoring of

contamination by hydrocarbons (Sauck, 2000; Batayneh, 2005; Shevvin *et al.* 2005; Delgado-Rodriguez *et al.*, 2014).

Facing the possibility of delimitation of contaminants in soil and groundwater, geophysical methods allow the analysis of the evolution and persistence of hydrocarbon as a technique for monitoring the natural attenuation of the contaminant.

This paper performs an analysis of geochemical and geophysical data (DC Resistivity and Induced Polarization, IP, methods) over a benzene-contaminated area from a railway accident, which is currently being monitored for natural attenuation processes.

### Study area

The area of study is located on a farm named Ribeirão do Paraíso, near São Manuel city, São Paulo State, southern Brazil. The area can be accessed by the highway Marechal Rondon (SP 300) (Figure 1).

In December 1999 a rail accident occurred involving the railway company Ferroban - Ferrovias Bandeirantes - which resulted in the derailment and overturning of three tank cars carrying fuel oil between the segment from Rubião Junior to Bauru with spilling and leakage of about 240,000 liters of diesel (CETESB, 2011).

The property where the accident occurred received from Ferroban the first responses for recovery and containment of the material retained on the surface. The scattering of large quantities of oil impacted the groundwater and surface waters, with contamination of Igualdade creek, which has its course near the accident site.

The contaminated area was approximately 30,000 m<sup>2</sup>. Furthermore, Ferroban was made responsible for the environmental impact report, the risk assessment of the area and also for the delivery of such documents to the supervision of the Environmental Agency of the São Paulo State - Companhia de Tecnologia de Saneamento Ambiental (CETESB), responsible

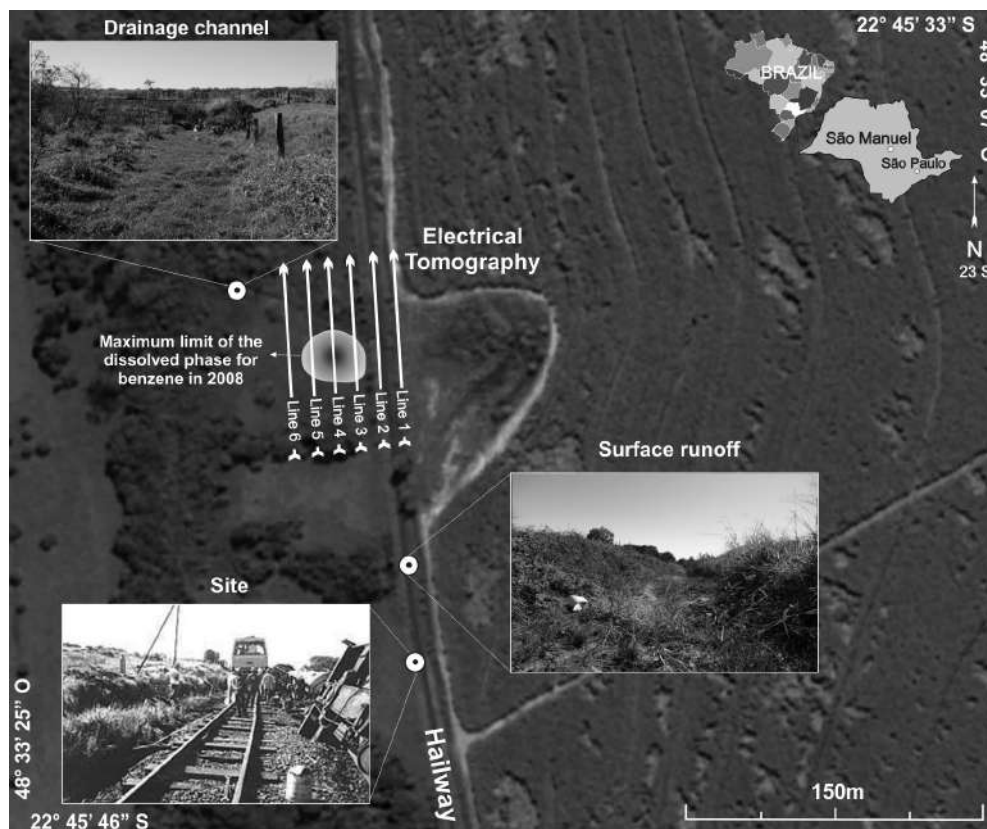


**Figure 1.** Study area, with site, surface runoff, drainage channel under railway, lines of geophysical investigation and maximum limit of the dissolved phase for benzene in 2008.

for this type of occurrence (CETESB, 2011). Probing carried out on site and the installation of monitoring wells allowed for a geological and hydrogeological characterization of the area. In the profiles surveyed sandy-clay soils were identified, with the presence of organic matter, having a thickness of 0.3 to 1.0 m, superimposed on fine sandstones belonging to the Adamantina Formation, Bauru Group, sequence of the Paraná Sedimentary Basin.

Near the drainage, there are outcrops of Quaternary Age alluvial sediments consisting of medium to coarse quartz sand. The hydrogeological data show that the level of the water table is shallow, with a maximum depth of 4.2m in the highest region of the topography, and sub-cropping near the drainage. The results of permeability measurements indicate maximum hydraulic conductivity of  $7.663 \times 10^{-4}$ cm/s and minimum of  $5.783 \times 10^{-5}$ cm/s. The maximum speed of flow calculated was 0.135m/d (CETESB, 2011). The groundwater flow follows the local topography, from southeast to northwest, towards Igualdade creek (Figure 2).

The analytical results of the historical series of groundwater monitoring (at the accident) indicate the presence of BTEX compounds (Benzene, Toluene, Ethylbenzene and Xylene), especially benzene with greater temporal persistence (Table 1).

### Natural attenuation processes

Once the petroleum-derived hydrocarbons reach the ground, they can undergo evaporation or penetrate and reach the groundwater. When in contact with these waters, they are subject to dissolution or remain in the residual free phase, named non-aqueous phase liquids (NAPL), which can fill the pores of the soil so that they become a continuous source for the contamination of the aquifer (Suthersan and Paine, 2005; Haritash and Kaushik, 2009).

Reaching the aquifer, the NAPLs are divided according to their relative density to water in light phase LNAPL (Light Non-Aqueous Phase Liquids) represented by compounds BTEX (Benzene, Toluene, Ethylbenzene and Xylenes) and dense phase DNAPL (Dense Non-Aqueous Phase Liquids), consisting of the group of polyaromatic hydrocarbons (PAH). The NAPLs compounds have great potential for contamination in soils and groundwater.

Without human intervention and under favorable environmental conditions, organic compounds undergo a reduction in their mass, toxicity, volume and concentration through physical, chemical and biological processes (Samanta *et al.*, 2002). This process of natural attenuation occurs both in the saturated and unsaturated zone. These processes include, beside biodegradation, mechanisms of dispersion, dilution, evaporation and adsorption.

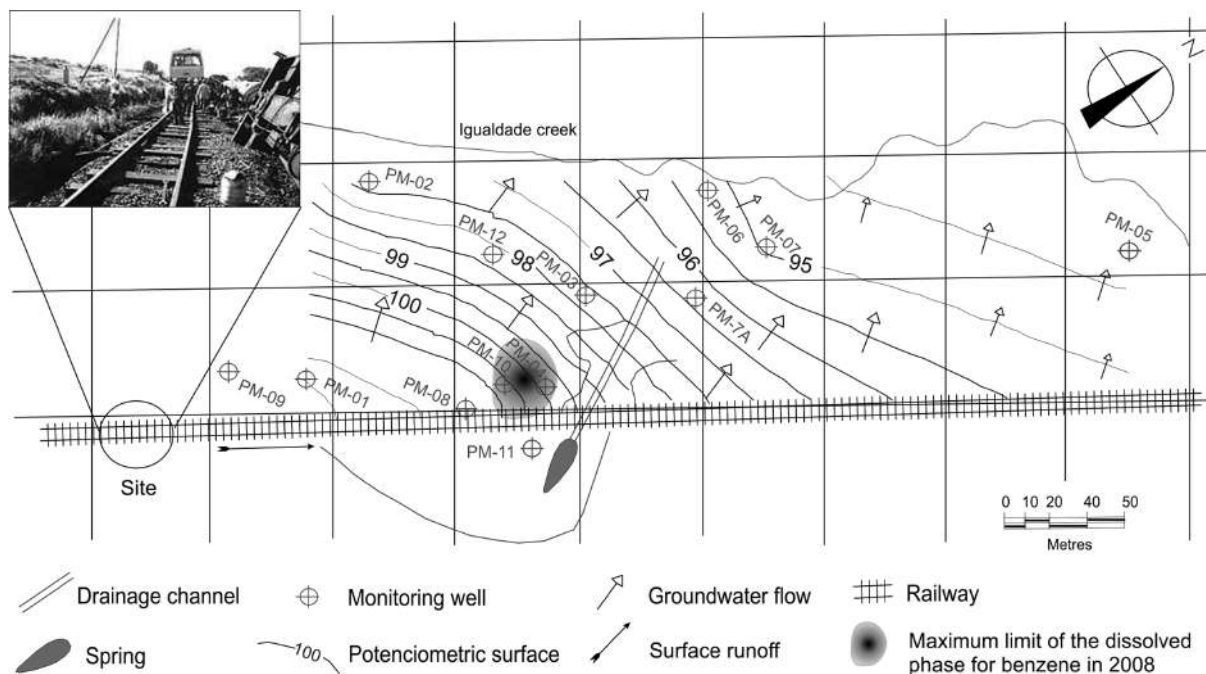


**Figure 2.** Groundwater flow with electrical resistivity tomography lines.

**Table 1.** Evolution of the benzene in aquifer (in µg/l) (CETESB, 2011).

Well	Date								
	11/2000	12/2003	08/2006	03/2008	10/2008	06/2009	11/2009	10/2010	03/2011
PM-01	<L.D	<L.D.	<L.D.	<L.D.	<L.D.	<L.D.	<L.D.	*	<5,0
PM-02	<L.D	<L.D.	<L.D.	<L.D.	<L.D.	<L.D.	<L.D.	<5,0	*
PM-03	<L.D	<L.D.	<L.D.	<L.D.	<L.D.	<L.D.	<L.D.	<5,0	<5,0
PM-04	420	76	55,1	15	2,81	5,7	4,1	<5,0	5,8
PM-05	<L.D	<L.D.	<L.D.	*	*	*	*	*	*
PM-06	-	<L.D.	<L.D.	*	<L.D.	<L.D.	<L.D.	<5,0	<5,0
PM-07	-	<L.D.	<L.D.	<L.D.	<L.D.	<L.D.	<L.D.	<5,0	<5,0
PM-08	-	-	24,3	<L.D.	<L.D.	<L.D.	<L.D.	<5,0	<5,0
PM-09	-	-	<L.D.	<L.D.	<L.D.	<L.D.	<L.D.	<5,0	<5,0
PM-10	-	350	20,1	28,3	5,3	3	<L.D.	<5,0	<5,0
PM-11	-	-	<L.D.	<L.D.	<L.D.	*	*	*	*
PM-12	-	-	<L.D.	<L.D.	<L.D.	<L.D.	<L.D.	<5,0	<5,0

L.D.: Limit of detection \* Destroyed well.

Dispersion and dilution of contaminants depend almost exclusively on the physical characteristics of the aquifer, such as hydraulic conductivity, which influences the transport of groundwater. This conductivity, when high, increases the extent of contamination, but decreases the average concentration due to dilution. Thus, at lower concentrations, microorganisms meet the most favorable environments for the performance of the natural degradation processes (Wilson and Jones, 1993).

Volatilization of compounds is relatively low, because the surface area between the contaminant on residual or dissolved phase with the atmosphere is small, often neglected in diagnostics. Several studies showed that less than 5% of the dissolved phase of BTEX is converted into gas by volatilization (Romero-Zerón, 2015).

Another common destiny for contaminants are the pores present in the soil. Due to the hydrophobicity of the hydrocarbon molecules and to the mechanisms of sorption caused mainly by clay minerals, organic matter and oxides and sulfites of iron and manganese from the soil, these compounds tend to be trapped in these pores or in fractures of rocks at the surface (Thomas and Ward, 1989).

The affinity of the contaminant with the soil matrix may not be sufficient to isolate the contaminant from the permanent groundwater. Sorption does not remove the mass of contaminant, only retards its migration, and depending on the rate of desorption, it can reach the groundwater (Wilson and Jones, 1993; Thomas and Ward, 1989).

The main mechanism of natural attenuation of hydrocarbons in soil and groundwater is biodegradation, where microorganisms convert hydrocarbons to organic acids or promote the complete oxidation and mineralization (Hiebert and Bennett, 1992; Bezalel *et al.*, 1996a; Bezalel *et al.*, 1996b; Hofrichter *et al.*, 1999). The generation of these acids in large amounts results in mineral dissolution and ion release to the saturated zone of the aquifer (Hiebert and Bennett, 1992). In this manner the electrical conductivity of the impacted zone can be greatly increased.

This transformation is mainly limited by the availability of electron receptors and hydrocarbons that assume the role of electron donors to the degradation, and therefore need to be biochemically accessible to microorganisms. Additionally, other parameters such as pH, temperature, salinity and redox potential are also important for biodegradation. Under aerobic conditions, where dissolved oxygen is the electron acceptor, biodegradation is more effective and allows complete conversion of hydrocarbons into non-toxic products such as CO<sub>2</sub>, CH<sub>4</sub> and H<sub>2</sub>O (Haritash and Kaushik, 2009).

## Method

The geophysical methods applied were DC Resistivity and Induced Polarization through six lines of Electrical Resistivity Tomography (ERT) in a Wenner-Schlumberger arrangement with 104m length for each row, placed parallel to the railway with 12.5m spacing, and 2m spacing between electrodes (Figure 1). Due to a greater induction on potential electrodes, this arrangement presents a great signal to noise ratio and satisfactory sensitivity to analyze

structures for vertical flow in the geological environment (Furman *et al.*, 2003; Okpoli, 2013; Moreira *et al.*, 2016).

The geophysical equipment used was the Terrameter LS resistivity meter, manufactured by ABEM Instrument (Sweden), which consists in a single module of transmission and reception of signals. During the acquisition, non-polarizable electrodes based on copper sulfate solution (Cu-CuSO<sub>4</sub>) were used, characterized by a copper wire inside and a porous base, which allows solution percolation in the soil. This procedure reduces contact resistance and minimizes the generation of parasitic currents generated by the use of metal electrodes during readings.

The equipment has an automatic acquisition through previous programming in a multi-cable system, with 250 W, resolution of 1  $\mu$ V and maximum current of 2.5 A. It enables the performance of spontaneous potential (SP), DC resistivity (R) and induced polarization (IP) by means of periodic cycles of transmission and reception of signals, automated calculation of the contact resistivity and standard deviation from the measurement set (ABEM, 2012). This equipment was calibrated with the following parameters to the IP time domain method: transmission of 400mA for 1.0s in each measure; two window lectures with 100 ms each and a delay time of 0.4 s.

The positioning of the lines was based on the latest geochemical data available relating to the monitoring of groundwater required by the environmental agency (Figure 1). These data describe the presence of benzene with maximum values of 2.8  $\mu$ g/l for the dissolved phase in well PM-04 and 5.3  $\mu$ g/l for PM-08 in 2008 (Table 1).

The field measurements were processed with the software Res2dinv and resulted in profile sections, with logarithmic graphical scale and intervals of interpolation of values in colors. This is a software that determines automatically a two-dimensional model of the subsurface (Griffiths and Barker, 1993). It divides the pseudo-section into rectangular blocks, which models the pseudo-section by the adjustment of data until the model produces values that match the field measurements. This optimization aims to reduce the difference between the apparent resistivity/chargeability values, calculated from the model and the one measured in the field, with the combined differences expressed in RMS (root-mean-square) (Loke and Barker, 1996).

The data generated after the 2D inversion were gathered into a single file, which unites the position of the readings along the lines (variable "x"), spacing among lines (variable "y"), depth modeled by the inversion (variable "z") and the value of resistivity/chargeability (variable "M"), later used as a database for generating 3D pseudo-modeling maps.

This spreadsheet was used for the generation of 3D pseudo-models, in a routine of basic steps adopted in mineral research. In this case, the sampling plan is frequently defined from statistic, structural criteria, spatial placement of a mineral accumulation, among other (Moon *et al.*, 2006). A simple procedure consists in sampling by a set of perforations perpendicular to the main axis of the structure, followed by a parallel set of perforation lines.

This process was developed in the Oasis Montaj platform where 2D inversion results obtained from the Res2Dinv were interpolated and modeled using the kriging method, for enhancement of extreme values in a model of three-dimensional blocks, where electrical tomography lines were positioned. Geophysical 3D pseudo-models generated from 2D sections provide a very wide comprehension of the complexity of geological and hydrogeological structures (Chambers *et al.*, 2006; Aizebeokhai *et al.*, 2011, Moreira *et al.*, 2016; Vieira *et al.*, 2016; Côrtes *et al.*, 2016).

## Results and discussion

The processed data reveal a range of values for resistivity between 17  $\Omega$ .m and 1965  $\Omega$ .m, with a predominance of high values in the near-surface portions and gradual reduction on values with increasing depth. The portion of high resistivity in lines 3, 4 and 5 coincides with the delimitation of benzene plume carried out in 2008 based on chemical analysis of groundwater collection from wells. The same occurred for the chargeability data, which ranged from 0.01 mV/V to 21.6 mV/V, and has a zone of high chargeability in the middle of lines 3 and 4 (Figure 3 and 4).

The field work occurred during summer, after long periods of rain; which conditioned a low contact resistance between the electrodes and the soil. In this way the data quality enabled a favorable processing with low RMS to the tomography profiles.

The high resistivity values in the proximity to the area with higher concentrations of hydrocarbons in the aquifer may be an indicative of the presence of residual phase in

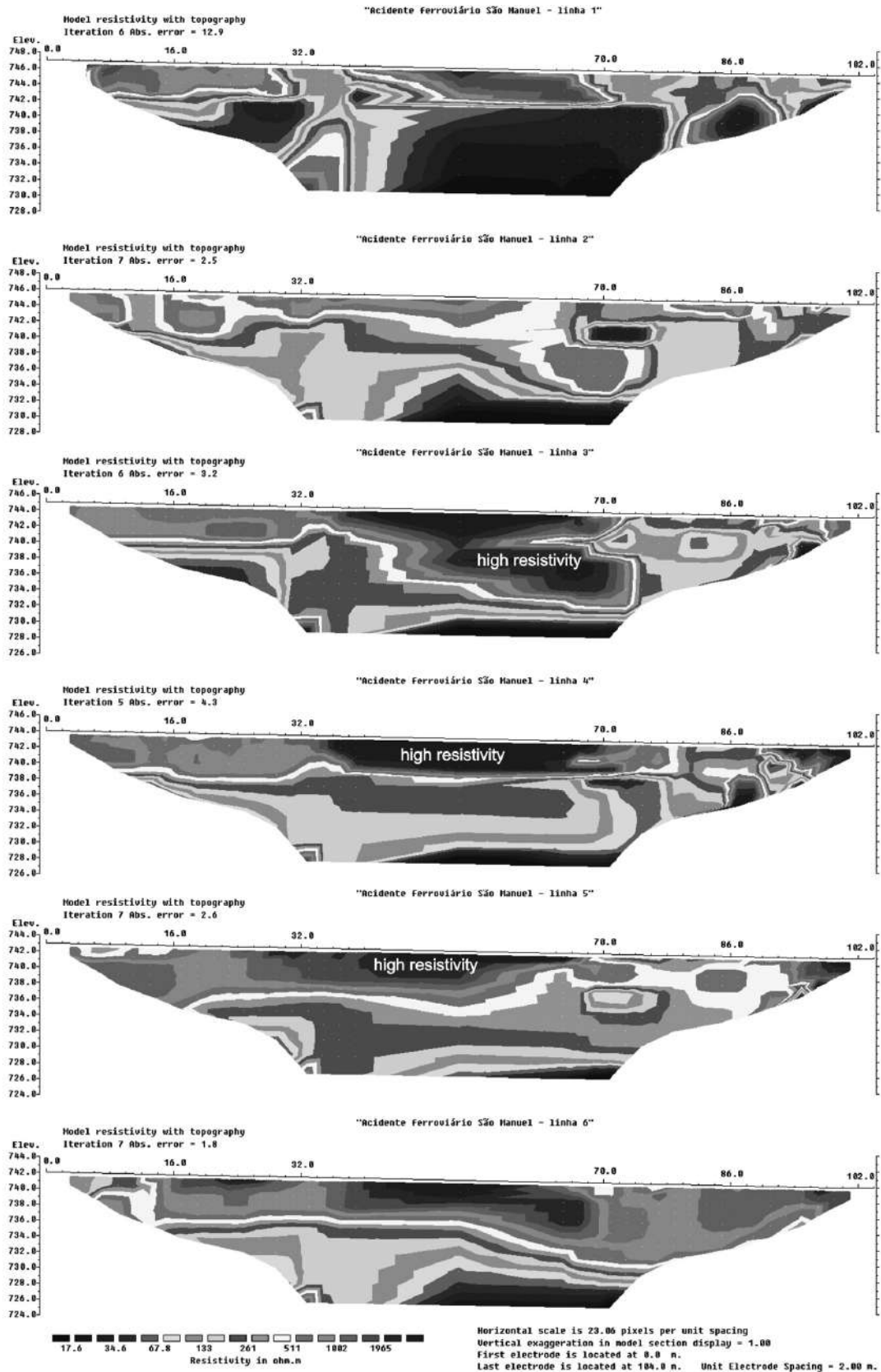


Figure 3. 2D resistivity sections with featuring to high resistivity values.

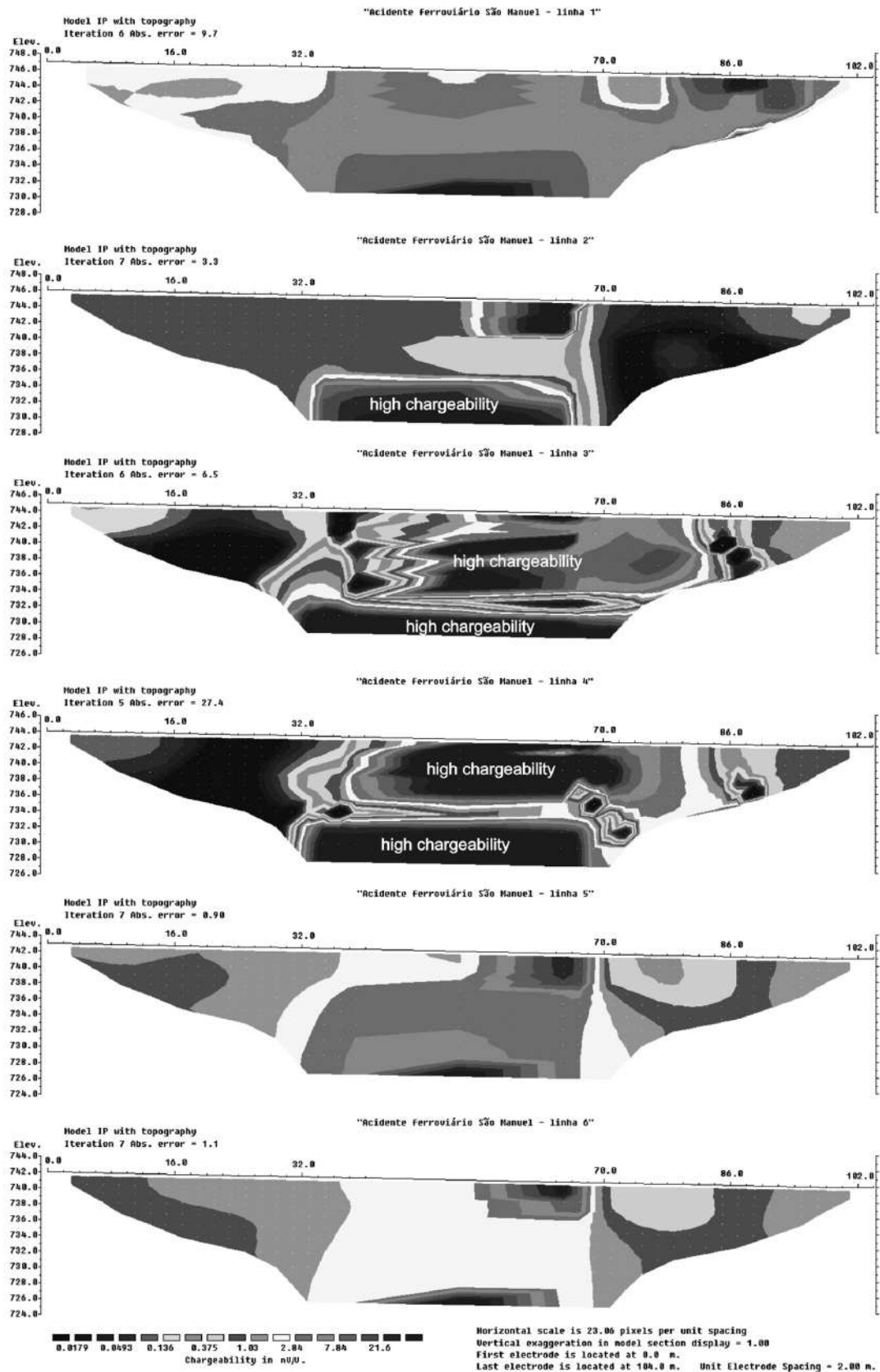


Figure 4. 2D chargeability sections with featuring to high chargeability values.

intermediate conditions of degradation. The gradual decrease in resistivity of lines 5 and 6 may indicate the more effective conversion of residual phase to the dissolved phase, besides the gradual return to the natural conditions of the area through the complete consumption of hydrocarbons by the action of natural attenuation processes.

Chargeability data points out to the residual contamination, however, there are anomalies of high chargeability that do not have the high resistivity corresponding values. Once a large volume of diesel spilled (240.000 liters), it contaminated great areas, hence, the high chargeability values indicates zones that correspond to the dissolved phase and the potential subproducts of biodegradation.

In sequence, the initial data were modeled from the minimum curvature method, for smoothing the core values in relation to the limits of the investigated area, and the range of 1800  $\Omega$ .m to resistivity and 20 mV/V for chargeability values was modeled as a 3D surface in an attempt to assess the shape of the high chargeability zone, where the water level and the ground/saprolite contact were also shown (Figure 5).

The 3D surface generated for values of 1800  $\Omega$ .m provides a perspective view and the chargeability surface for 20 mV/V allows for an integrated vision of the data and the shape of an elongated body in the direction of the local groundwater flow that crosses the lines of electrical imaging. This chargeability body has a double-conical shape, with reversed and opposite larger bases and smaller overlapping ends, whereas the resistivity body has a large format in the unsaturated zone and a conical shape in the aquifer (Figure 5).

The site is at a sandy aquifer with saprolite clay matrix that increase with depth, and consists of a water column of about 6 m thickness.

The intervals in the unsaturated zone, mainly between depths of 2 and 4 m are characterized by a horizon enhanced in clay, originating from weathering processes and surface conduction for this depth interval, by dissolution and rainfall infiltration into the soil. In the zone of quartz sandstone with clay matrix, the high polarization values obtained in a center of residual contamination in soil/saprolite may reflect products related to the degradation of the leaked hydrocarbons, formed by the action of natural attenuation processes.

The action of organic acids on mineral grains can cause the dissolution and availability of chemical elements in the dissolved phase, due to conditions of pH and Eh artificially generated in the region of the hydrocarbon degradation processes. The mineralization is one of the final steps in this process, which involves the conversion of cations and anions initially dissolved, into forms of higher chemical stability, as secondary minerals (Hiebert and Bennett, 1992; Bezael *et al.*, 1996a; Bezael *et al.*, 1996b; Hofrichter *et al.*, 1999).

In this context, the clay minerals can make a decisive contribution as a source of chemical elements. The Fe and Mn are the main cations of low mobility present in clay minerals of tropical soils. These elements tend to remain in the alteration profile and often form structures named laterites, which in many places serve as guides to prospecting for mineral deposits of oxides and sulfides (Moon *et al.*, 2006; Taylor, 2011; Moreira *et al.*, 2014).

Some of these minerals are electrically polarizable based on the phenomenon of electronic polarization, which involves the accumulation of electric charges in metallic materials by artificially induced electric current (Keller and Frisknecht, 1966), the accumulation of which allows the generation of distinguishable contrast in IP surveys.

In the zone above the water table there is a bottleneck in the high chargeability body with an increase in depth, possibly due to the increased water content. In this case, a gradual reduction in aerobic conditions due to the unavailability of atmospheric oxygen and a concomitant increase in anaerobic conditions, i.e., decrease in Eh with depth occurs. It is probable that sulphide predominate in unsaturated locations, gradually converted to hydroxides with the increase in moisture (Govett, 2000).

In the aquifer zone, the body of high chargeability presents the smallest lateral thickness, where sulphide probably predominate in the most reducing locations. The continuous supply of water by lateral groundwater flow in an aquifer of high permeability should oxygenate this horizon and cause changes in the physicochemical conditions that are likely to result in instability of mineral and dissolution, preserving only the most reduced central zone.

The saprolite interval is characterized by a relatively low permeability and decreasing oxygenation with an increase in depth, present

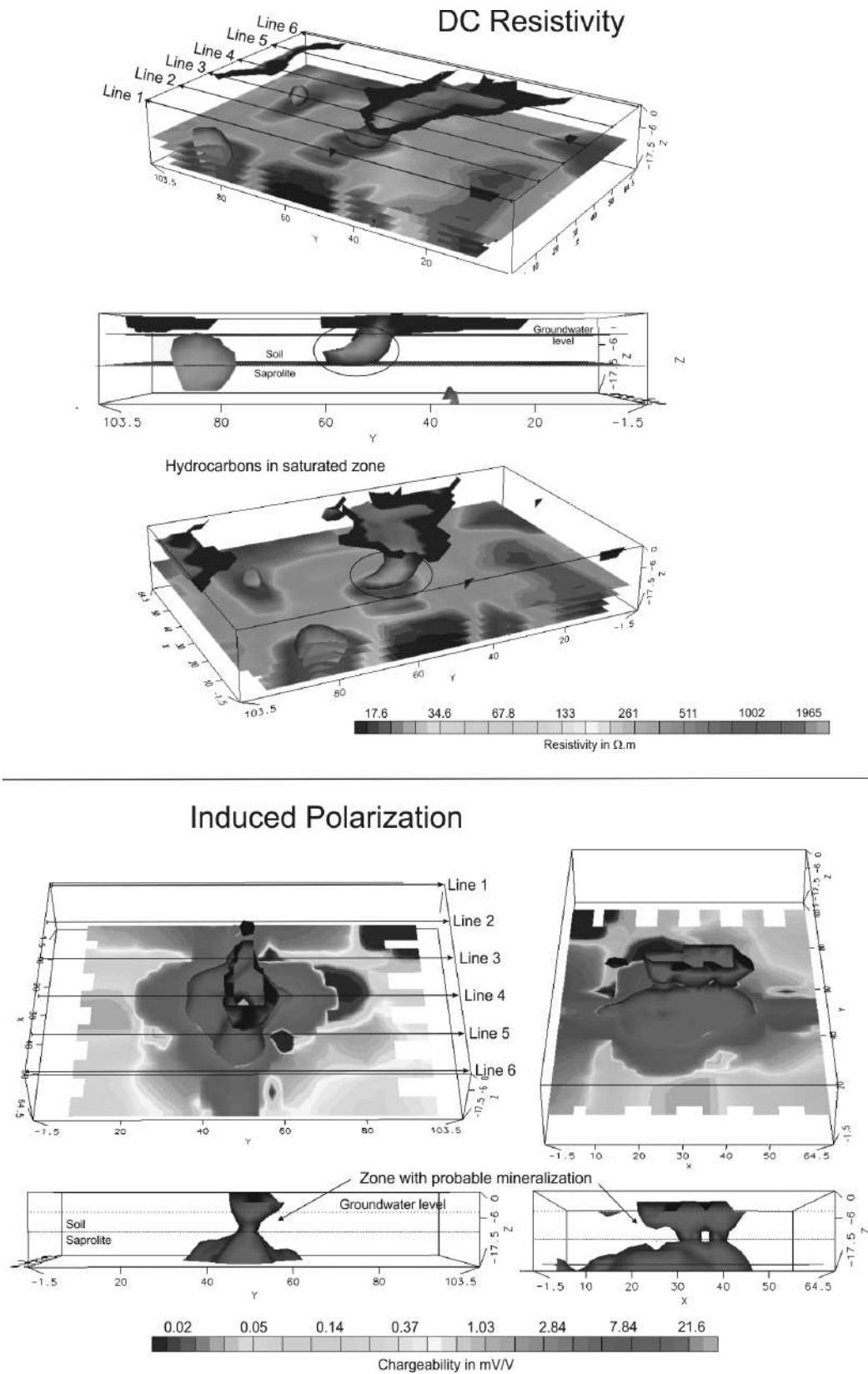


**Figure 5.** Geophysical integration data. a) Resistivity 3D isosurface modeling of 1800  $\Omega.m$  b) Chargeability 3D isosurface modeling of 20 mV/V, with groundwater level and the soil/saprolite contact.

favorable conditions for the preservation of potential sulphide e residual hydrocarbons.

Within this set of processes, the zone of high chargeability associated with the central area of residual contamination must reflect the presence of oxides/sulphide and eventually disseminated sulphide, having available sulfur, crystallized by recombination of chemical elements originated from the mineral dissolution by the attack of organic acids produced during the degradation of hydrocarbons.

## Conclusions

The history of events in the area points to a leakage of a large volume of diesel in the railway right-of-way, with surface runoff and impoundment in a drainage channel under the railway, where infiltration occurred for part of the leaked volume, which resulted in the contamination of soil and groundwater. The monitoring of groundwater by chemical analysis indicates a downward trend in the levels over the subsequent years, with moments of slight increase with sporadic input of hydrocarbons into the aquifer.

In the absence of systems for treatment and remediation of the area by invasive techniques, dispersion, dilution and consumption of contaminants occur in the area by the action of natural attenuation processes that act on the physical structure of hydrocarbons and cause their fragmentation and final reduction to methane and water. The generation of organic acids, dissolution and mineral neoformation are consequences of these processes.

Both phases of hydrocarbons were subject to recognition by means of the DC resistivity method, contrasting with the uncontaminated environment. The region with the highest levels of dissolved phase was characterized by high resistivity values ( $> 1000 \Omega.m$ ), indicative of the presence of high concentrations of residual phase, in face of the typical high resistivity of low degraded hydrocarbons.

The signature of high chargeability in the areas contaminated by hydrocarbons is a clear indication of the accumulation of metallic minerals, in contrast with the native materials, suggesting their origin from the natural attenuation processes occurring in the area. Thus, the induced polarization method allows the detection of contrasts in physical properties caused indirectly by the presence of hydrocarbons in soil and groundwater.

Low values of chargeability in areas with signs of contamination do not necessarily indicate the absence of contaminants, whereas high values of chargeability also do not necessarily indicate the presence of these compounds. In many cases, the hydrocarbon may have been completely consumed in old contaminations, and only the by-products of the process remained in the environment, as mineral neoformations subjected to polarizability.

The application of this geophysical method in conjunction with direct techniques for remediation of hydrocarbon contaminated areas can contribute in increasing the efficiency of the site characterization process, especially giving the possibility of geophysical scans in the unsaturated zone and the monitoring of areas of accumulation of metallic minerals, indicative of the effective remediation of contaminant hydrocarbons.

Another important aspect is the great geochemical affinity that sulphides have for a number of metal elements during the crystallization of secondary minerals. This feature is exploited in studies of prospecting and exploration of mineral deposits, as laterites which eventually cover a non-outcropping mineral deposit can incorporate metallic elements directly associated with the deposit (Moon *et al.*, 2006; Taylor, 2011; Aal *et al.*, 2014).

In this regard, in complex contamination events involving hydrocarbons and metals, the detection of metallic mineralization originated by the presence of hydrocarbons is something desirable and should be considered in decontamination activities, taking into account the high capacity for retention of metals during the crystallization of sulphide in soils and groundwater.

## References

- ABEM, 2012, Terrameter LS – Instruction Manual. Sundbyberg: ABEM Instrument.
- Aal G.Z.A., Estella A., Atekwana A., Revil A., 2014, Geophysical signatures of disseminated iron minerals: A proxy for understanding subsurface biophysicochemical processes. *J. Geophys. Res.*, Biogeosciences, 119, 1831–1849.
- Aizebeokhai A.P., Olayinka A.I., Singh V.S., Uhuegbu C.C., 2011, Effectiveness of 3D geoelectrical resistivity imaging using parallel 2D profiles. *Int. J. Phys. Sci.*, 6, 5623-5647.

- Alvarez P.J.J., Illman W.A., 2006, Bioremediation and natural attenuation: process fundamentals and mathematical models. John Wiley & Sons, Hoboken, 614 pp.
- Batayneh A.T., 2005, 2D Electrical Imaging of an LNAPL Contamination, Al Amiriyya Fuel Station, Jordan. *J. Appl. Sci.*, 5, 52-59.
- Berkowitz B., Dror I., Yaron B., 2008, Contaminant Geochemistry - Interactions and Transport in the Subsurface Environment. Springer, Berlin, 413pp.
- Bezalel, L. Hadar Y., Fu P., Cerniglia C., 1996a, Mineralization of Polycyclic Aromatic Hydrocarbons by the White Rot Fungus *Pleurotus ostreatus*. *Appl. Environ. Microb.*, 62, 292-295.
- Bezalel L., Hadar Y., Fu P., Freeman J., Cerniglia C., 1996b, Initial Oxidation Products in the Metabolism of Pyrene, Anthracene, Fluorene, and Dibenzothiophene by the White Rot Fungus *Pleurotus ostreatus*. *Appl. Environ. Microb.*, 62, 2554-2559.
- Bhandari A., Surampalli R.Y., Champagne P., Ong S.K., Tyagi R.D., Lo I.M.C., 2007, Remediation Technologies for Soils and Groundwater. *Am. Soc. Civ. Engin.*, Reston, 441 pp.
- Chambers J.E., Kuras O., Meldrum P.I., Ogilvy R.D., Hollands J., 2006, Electrical resistivity tomography applied to geologic, hydrogeologic, and engineering investigations at a former waste-disposal site. *Geophysics*, 71:231-239.
- CETESB, COMPANHIA DE TECNOLOGIA DE SANEAMENTO AMBIENTAL, 2011, Ferrobarragem Bandeirantes S.A. Monitoramento Hidrogeológico, 6ª campanha. São Manuel – SP. São Paulo: Secretaria do Meio Ambiente.
- Côrtes A.R.P., Moreira C.A., Veloso D.I.K., Vieira L.B., Bergonzoni F.A., 2016, 528 Geoelectrical prospecting for a copper-sulfide mineralization in the Camaquã 529 sedimentary basin, Southern Brazil. *Geofísica Internacional*, 55, 3, 107-117.
- Delgado-Rodríguez O., Flores-Hernández D., Amezcua-Allieri M.A., Shevnin V., Rosas-Molina A., Marín-Córdova S., 2014, Joint interpretation of geoelectrical and volatile organic compounds data: a case study in a hydrocarbons contaminated urban site. *Geofísica Internacional*, 53, 183-198.
- Furman A., Ferre T.P.A., Warrick A.W., 2003, A sensitivity analysis of electrical resistivity tomography array types using analytical element modeling. *Vadose Zone J.*, 2, 416-423.
- Govett G.J.S., 2000, Handbook of Exploration Geochemistry. Elsevier, Amsterdam, 549pp.
- Griffiths D.H., Baker R.D., 1993, Two-dimensional resistivity imaging and modeling in areas of complex geology. *J. Appl. Geophys.*, 29, 211-226.
- Haritash A.K., Kaushik C.P., 2009, Biodegradation aspects of Polycyclic Aromatic Hydrocarbons (PAHs): A review. *J. Hazard. Mat.*, 169, 1-15.
- Hiebert F.K., Bennett P.C., 1992, Microbial control of silicate weathering in organic-rich groundwater. *Science*, 258, 278-281.
- Hofrichter M., Vares T., Kalsi M., Galkin S., Scheibner K., Fritsche W., Hatakka A. (1999). Production of Manganese Peroxidase and Organic Acids and Mineralization of <sup>14</sup>C-Labelled Lignin (<sup>14</sup>C-DHP) during Solid-State Fermentation of Wheat Straw with the White Rot Fungus *Nematoloma frowardii*. *Appl. Environ. Microb.*, 65, 1864-1870.
- Keller G.V., Frishknecht F., 1966, Electrical Methods in Geophysical Prospecting. Pergamon Press, Oxford, 517pp.
- Knödel K., Lange G., Voigt H.J., 2007, Environmental Geology: Handbook of fields methods and case studies. Springer, Hannover, 1357pp.
- Loke M.H., Baker R.D., 1996, Rapid least-squares inversion of apparent resistivity pseudosections by quasi-Newton method. *Geophys. Prosp.*, 44, 131-152.
- Moon C.J., Whateley M.E.G., Evans A.M., 2006, Introduction to mineral exploration. Australia: Blackwell Publishing.
- Moreira C.A., Borges M.R., Vieira G.L., Malagutti Filho W., Fernandes M.M.A., 2014, Geological and geophysical data integration for delimitation of mineralized areas in a supergene manganese deposits. *Geofísica Internacional*, 53, 199-210.
- Moreira C.A., Lapola M.M., Carrara A., 2016, Comparative analyzes among electrical resistivity tomography arrays in the

- characterization of flow structure in free aquifer. *Geofísica Internacional*, 55, 2, 119-129.
- Okpoli C.C., 2013, Sensitivity and resolution capacity of Electrode configurations. *Int. J. Geophys.*, 2013, 12p
- Redd K.R., Adams J.A., 2015, Sustainable remediation of contaminated sites. Momentum Press, New York, 268pp.
- Romero-Zerón L., 2012, Introduction to enhanced oil recovery (EOR) processes and bioremediation of oil-contaminated sites. InTech, Rijeka, 328pp.
- Samanta S.K., Singh O.V., Rakesh K.J., 2002, Polycyclic aromatic hydrocarbons: environmental pollution and bioremediation. *TRENDS in Biotechnology*, 20, 6, 243-248.
- Sara M., 2003, Site assessment and remediation handbook. 2<sup>o</sup>ed., Lewis Publishers, Florida, 1161 pp.
- Sauck W.A., 2000, A model for the resistivity structure of LNAPL plumes and their environs in sandy sediments. *J. Appl. Geophys.*, 44, 51-165.
- Shevnin V., Delgado-Rodríguez O., Fernández-Linares L., Zegarra-Martinez H., Mousatov A., Ryjov A.A. 2005. Geoelectrical characterization of an oil contaminated site in Tabasco, Mexico. *Geofísica Internacional*, 44, 3, 251-263.
- Suthersan S.S., Paine F.C., 2005, In Situ Remediation Engineering. CRC Press, Boca Raton, 602pp.
- Taylor R., 2011, Gossans and Leached Cappings – Fields Assessment. Springer-Verlag, Heidelberg, 165 pp.
- Twardowska I., Allen H.E., Häggblom M.H., 2006, Soil and water pollution: monitoring, protection and remediation. *Nato Sci. Ser.*, Springer, Krakom, 662 pp.
- Vieira L.B., Moreira C.A., Côrtes A.R.P., Luvizotto G.L., 2016, Geophysical modeling of the manganese deposit for Induced Polarization method in Itapira (Brazil). *Geofísica Internacional*, 55, 2, 107-117.
- Thomas J.M., Ward C.H., 1989, In situ bioremediation of organic contaminants in the subsurface. *Environ. Sci. Tech.*, 23, 760–766.
- Wilson S.C., Jones K.C., 1993, Bioremediation of soils contaminated with Polynuclear Aromatic Hydrocarbons (PAHs): a review. *Environ. Pollut.*, 81, 229–249.

## New insight on the recent instrumental seismic activity along the Serghaya fault, Syria

Abdul-Wahed M. K.\* and J. Asfahani

Received: August 22, 2016; accepted: February 24, 2017; published on line: July 01, 2017

### Resumen

En este trabajo se presentan observaciones y análisis basados en datos instrumentales de actividad sísmica a lo largo de la falla Serghaya. La actividad sísmica registrada por estaciones de período corto entre 1995 y 2009, muestra una actividad significativa que se ha asociado con trazos superficiales conocidos de "steps-over" a lo largo de la falla Serghaya. Los enjambres espaciales podrían relacionarse con el "step-over" de la falla, por ejemplo en Deir el Acheir y Ham. Algunos enjambres se observaron en la región de Hermel, pudiéndose relacionar con una posible extensión de la falla Serghaya en el NE de Líbano. La zona sismogénica pudo coincidir con la supuesta localización de unión desde la falla Serghaya hasta las fallas de Jhar y Bishri. Esta evidencia completa los resultados de estudios anteriores que demostraron que el último sismo destructivo se localizó en la falla Serghaya y pudo ser anterior a los sismos de la falla Yammouneh. La falla Serghaya es probablemente la fuente más plausible de riesgo sísmico en Siria y Líbano.

Palabras clave: alla Serghaya, sistema de fallas del Mar Muerto, snjambres de sismos, falla "steps-over".

### Abstract

This study presents detailed observations and analyses based on the recent instrumental seismic activity along the Serghaya fault. The earthquake activity, recorded by short period stations between 1995 and 2009, reveals significant activity often associated with known surface traces of steps-over along Serghaya fault. Spatial clusters could be related to the fault steps-over; e.g., at Deir el Acheir and Ham. Some clusters have been observed in the Hermel region, and could be related to a probable extension of Serghaya fault in the NE of Lebanon. This seismogenic zone could coincide with the suggested location of linkage from Serghaya fault to the Jhar and Bishri faults. Such evidence completes the findings of previous studies, which have demonstrated that the latest destructive earthquake was located on the Serghaya fault and could be younger than the earthquakes of Yammouneh fault. Therefore, Serghaya fault is, probably, the most plausible source of earthquake hazard in Syria and Lebanon.

Key words: Serghaya fault, Dead Sea fault system, earthquake clustering, steps-over fault.

---

Abdul-Wahed M. K.\*  
J. Asfahani  
Dept. of Geology  
Atomic Energy Commission of Syria  
P.O. Box. 6091, Damascus- Syria  
\*Corresponding author: [cscientific@aec.org.sy](mailto:cscientific@aec.org.sy)

## Introduction

Serghaya fault is a branch segment of the main Dead Sea Fault System (DSFS) in south-western Syria (Figure 1). Until 1995, it has not been considered as active branch since the Pliocene (Butler *et al.*, 1997) and our knowledge of this part of DSFS was relatively limited. However, the results of paleoseismological trenching (Gómez *et al.*, 2001; 2003; Nemer *et al.*, 2008) strongly exhibit that this fault could be capable to generate a destructive earthquake and could be an important element in the regional seismic hazard assessment. The seismic potential of Serghaya fault in areas adjacent to major cities, such as Damascus, justifies the necessity and the need of characterizing the seismic activity of this fault. Asfahani and Abdul-Wahed (2013) have established an instrumental earthquake catalogue for the Serghaya fault for the period

from 1995 to 2009. They point out that the seismicity related to the Serghaya fault, during the study period, displays a remarkable clustering of low-magnitude earthquakes ( $M_c$ : 2.2-3.9). These findings will be used in the present paper to establish where the Serghaya fault has seen such clustering. Therefore, the recent instrumental seismicity is correspondingly investigated by analysis of the epicenter distribution along the Serghaya fault. The published catalogue will be the objective for more detailed analysis to investigate the seismicity patterns for this fault than was possible earlier. The importance of this research is to use the instrumental seismicity, which has been observed by all the stations operating in the area on both sides of Serghaya fault in Syria and Lebanon covering the period from 1995 to 2009.

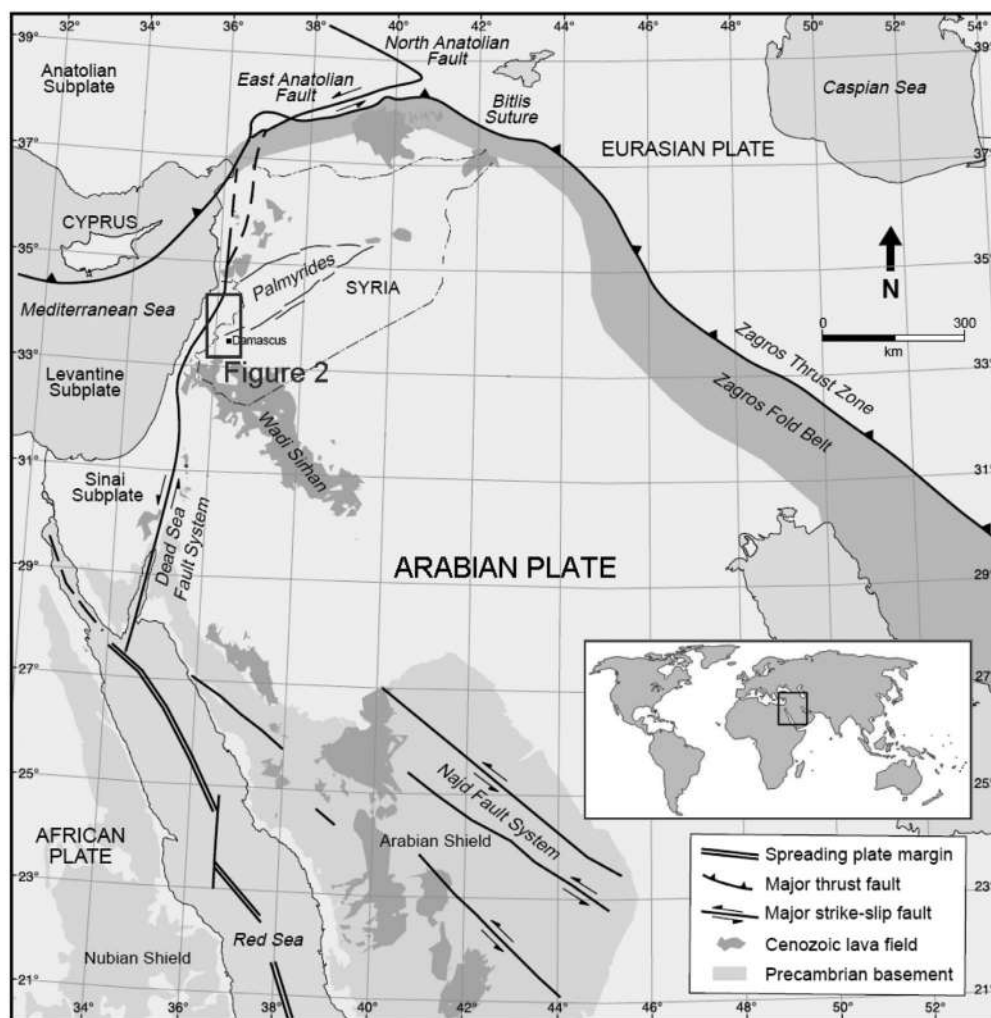


**Figure 1.** Regional tectonic map of the northern Arabian Plate and surrounding regions (modified from Brew *et al.*, 2001). The rectangle shows the location of Figure 2.

## Tectonic Setting of the region

The DSFS constitutes a plate boundary separating the Arabian plate from the African one, and contains their comparative motion as a system of sinistral fault branches (Figure 1). The northward movement of the Arabian Plate is faster than the African Plate, where the GPS measurements predict the total relative motion at the restraining bend to be  $\sim 6.8 \text{ mm yr}^{-1}$  (McClusky *et al.*, 2003). This relative motion of the two plates is taken up by the DSFS. Even though, there are many observed focal mechanisms all through the DSFS, however, the analysis of fault plane solutions of the main earthquakes confirms the left lateral nature of the DSFS (Salamon *et al.*, 2003). A set of deep pull-apart basins have been developed by the extensional mechanism associated with the prevailing of the left lateral motion of the DSFS. Such basins can be created in topographical lower areas (Ben-Avraham and Schubert, 2006). In fact, the DSFS could be divided into three main sections including the southern part, a 200 km long Lebanese restraining bend, and the northern part, which meets northwards with the East Anatolian Fault in southern Turkey (Figure 1).

Five fault segments are branching out within the restraining bend from the DSFS; these are: the Yammouneh, Roum (in South Lebanon), Hasbaya, Rachaya, and Serghaya faults (Figure 2) (e.g., Walley, 1988; Heimann and Ron, 1993). The northern DSFS, in Lebanon and Syria, has been considered as a sequence of transpressional steps-over, along which the left-lateral slip is apparently slower than the relative plate motion (Westaway, 1995; Gómez *et al.*, 2007). The DSFS has not been regarded as a transform fault zone since 1995 (Westaway, 1995).

### Local tectonic setting

The Serghaya fault branches out from the DSFS near Lake Tiberias (32.75 N, 35.60 E in the South-West of Syria) and extends along the Syrian–Lebanese border with a general trend of N30°E (Dubertret, 1955) (Figure 2). Many geomorphic expressions have been observed along Serghaya fault such as the alignment of linear valleys and large stream valley deflections, which indicate a clear leftward deflection (Gómez *et al.*, 2003). The young fault scarps and other features, such as offset streams, attest to recent coseismic ruptures (Nemer *et al.*, 2008). The geometries of left-stepping faults are systemically seen at the elongated basins through the Serghaya fault zone, suggesting a pull-apart mechanism for

the basins formation (Gómez *et al.*, 2001, 2003; Nemer *et al.*, 2008). The largest examples of such geometry are the fault steps-over at Deir el Acheir and Ham (Figure 2). Since the pull-apart basins that are developed along the concerned fault, their presence in a regional compressive system basically results from local left stepping and/or bending of the main left-lateral motion (Nemer *et al.*, 2008). The shear indicators in deformed upper Pleistocene lacustrine sediments in the southern Zebadani basin (Figure 2) predominantly demonstrate the left-lateral slip along this portion of the Serghaya fault (Gómez *et al.*, 2001; 2003). According to Gómez *et al.* (2001; 2003), an apparent strike-slip duplex led to the development of the Hermon mountain block, including the Serghaya and Rachaya faults segments (Figure 2). It is believed that these two faults are structurally interconnected as movement on one fault may enhance the corresponding movement on the other one (Nemer *et al.*, 2008). Consequently, the Serghaya and Rachaya faults could delineate together an active seismogenic fault system with respect to restraining bend of Lebanon. On the other hand, the Serghaya fault can be traced approximately for about 125 km through the upper cretaceous carbonate bedrocks of the Anti-Lebanon Mountains to the eastern edge of the Bekaa Valley (Figure 2). Along the Serghaya fault, many important field evidences for Quaternary strike-slip faulting have been observed as far north as the Lebanese village of Arsal (Figure 2) (Dubertret, 1955; Gómez *et al.*, 2003). The trace of the Serghaya fault is obscure towards the North of this point, where it disappears near the Baalbek city within the western edge of Anti-Lebanon mountain range (Dubertret, 1955). Its northern termination proposes a probable connection with the Jhar fault (Figure 1) as an oblique ramp or tear fault that bounds the Palmyrides fold belt (Walley, 1998; Gómez *et al.*, 2003; 2006). Moreover, it has been proposed by Walley (1998) that the Serghaya fault may extend towards NNE inside Syria, passing through Al Qusayr (34.50 N, 36.6 E) before splitting into the Jhar and Bishri faults within the Palmyrides fold belt (Figure 1). However, the fault could not be detected in the vicinity of Al Qusayr (e.g., Kozlov *et al.*, 1963; Ponikarov *et al.*, 1966), and nothing has been noticed during the recent fieldwork in this area (Bridgland *et al.*, 2003). This might be due to the presence of a thick cover of recent formation. Many evidences attest that the latest destructive earthquake was located on the Serghaya fault and could be younger than the earthquakes of Yammouneh fault (Gómez *et al.*, 2001; Tapponnier *et al.*, 2001; Daeron *et al.*, 2005). The Serghaya fault is, therefore, the most plausible source of earthquake hazard in Syria and Lebanon (Daeron *et al.*, 2005).

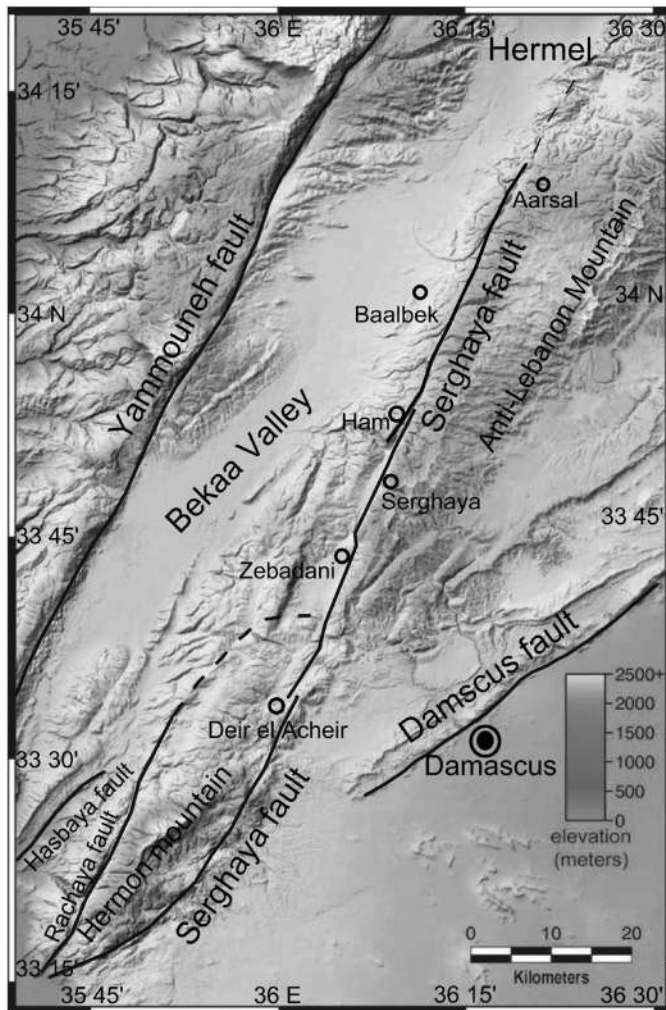


**Figure 2.** Local setting of Serghaya fault on shaded relief image (modified from Gómez *et al.*, 2003).

### Seismic activity

The instrumental seismicity in the central and northern DSFS, as observed from 1900 to the present day, depicts little earthquake activity in contrast with the historical records (e.g., Ambraseys and Jackson, 1998). The low level of seismicity and the scarce focal mechanisms could yield and probably support the idea of an apparent behavior of seismic quiescence for this part of the DSFS (Gómez *et al.*, 2003). Asfahani and Abdul-Wahed (2013) have found that the earthquake activity of Serghaya fault passes actually through a relative quiescence, in comparison with other active parts of DSFS such as Yammounah or Gulf of Aqaba (Figure 1). However, this result is not consistent with both the historical seismic activity (Sbeinati *et al.*, 2005), and the field observations that confirm the activity and the seismogenic potential of Serghaya fault (Meghraoui *et al.*, 2003). Several destructive earthquakes, occurring during the historical times, have been archived

in the historical sources (Sbeinati *et al.*, 2005). The results obtained from paleoseismic studies propose that Serghaya fault is active with slip rates of about 1.4 mm/year (Gómez *et al.*, 2001). The last historical earthquake implicated about 2–2.5 m of sinistral displacement and corresponds to historical earthquake of 1759. The average dislocation of about 2 m suggests that such event corresponds to an earthquake of  $M > \sim 7$  with a mean return period of about 1700 yrs (Gómez *et al.*, 2001, 2003; Meghraoui *et al.*, 2003). Instrumental seismicity of the eastern Mediterranean region shows that the southern part of DSFS is seismically active. The Gulf of Aqaba (29.0 N, 34.9 E in Figure 1), has been the most active area since the early 1980s, where thousands of small earthquakes have been recorded during several months. The activity reaches a point of highest development on November 22<sup>nd</sup>, 1995, when an earthquake of  $M_w 7.1$  (Baer *et al.*, 1999; Klinger *et al.*, 1999), was the biggest seismic event occurring along the DSFS during the 20<sup>th</sup> century. An

aftershock sequence, of about 60 earthquakes, continued for more than one year with many events surpassing magnitude 5.0.

### Syrian seismic network evolution

In 1985 the General Establishment of Geology and Mineral Resources (GEGMR), responding to an initiative proposed by the Program for Assessment and Mitigation of Earthquake Risk in the Arab Region (PAMERAR), started the design and implementation phases for the construction of the Syrian National Seismological Network (SNSN). The network's design objective was to monitor all discernible earthquake activity along the DSFS and its related branches in Syria and nearby Lebanon such as Serghaya fault. The nine seismic stations of the southern sub-network became operational in late 1994 and early 1995 and allowed to record the micro earthquake activity that occurred on November 22<sup>nd</sup>. 1995, along the Serghaya fault. The eleven stations of the northern sub-network followed the next year to complete the twenty stations of the western SNSN. The SNSN has been officially operated since January 14, 1995 (Dakkak *et al.* 2005). The seven eastern stations were added in April 2002, where two of them were three-component seismic stations. In 2003, the SNSN consists of twenty seven short period (1 Hz) stations of ~50 km seismograph spacing.

### Data and resources

All data used in this paper came from three seismic bulletins published by: the Syrian National Seismological Network (SNSN bulletins, 1995-2009), the Atomic Energy Commission of Syria (AECS bulletins, 1995-2009) and the Geophysical Research Arrays

of Lebanon (GRAL bulletins, 1995-2009). The data, gathered from these three seismic bulletins, have been used for construction of a combined catalogue (Asfahani and Abdul-Wahed, 2013). This published catalogue is the objective for more detailed analysis than was possible earlier to investigate the seismicity patterns for this fault. This analysis enables us to better understand the nature of Serghaya fault. Based on this catalog, a total of 350 events, occurring during the period of 15 years from 1995 to 2009, have been identified along Serghaya fault. The statistical analysis of the Serghaya catalogue indicates that the average occurring frequency of the recorded events is approximately four events by month. Such earthquake activity rate is considered as relatively very low. Some months, however, show a relative increasing in the recorded events number, which reaches 11 events per month, while other months do not indicate any recorded events as shown in Figure 3. Some temporal clustering can be generally observed in many time intervals such as November 1995 and 2008. On Figure 3, the increase of seismic activity can be observed since 2003. This observation could be related to the effect of a better operation of the national seismic network, where the southern sub-network started independently to detect and record the seismic events on the Serghaya fault zone. In this way, the acquisition system became more sensible and thereby additional micro-seismic events can be recorded. So, this increase could not reflect any significant changes regarding the fault behavior. Magnitudes in the three mentioned bulletins are calculated from the coda wave duration via the formula (GRAL bulletins 1995-2009):

$$M_c = 0.08 + 1.63 * \log(T) + 0.009 * D, \quad (1)$$

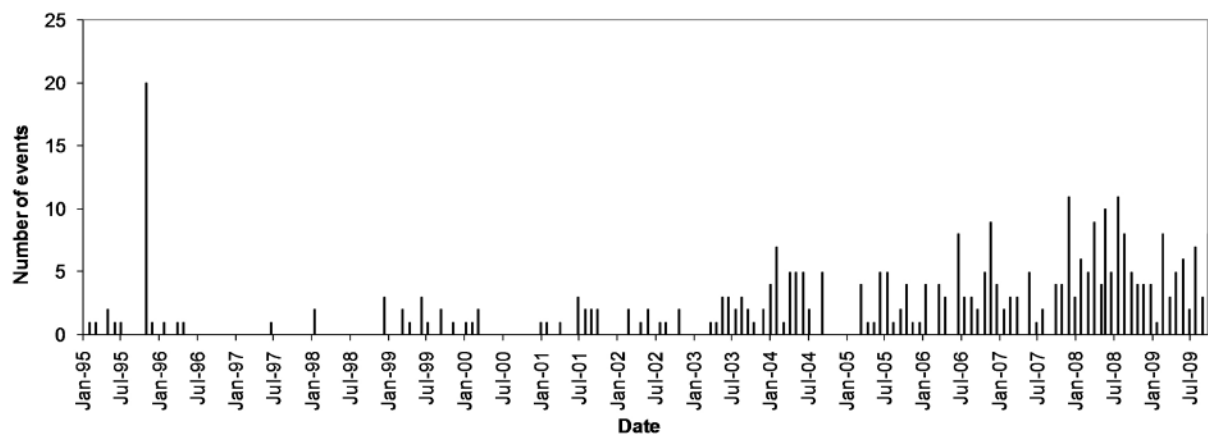


Figure 3. Monthly occurring frequency of the recorded events around Serghaya fault.

Where  $D$  is the epicentral distance (in km) and  $T$  is the coda duration (in seconds).

Most of the events, included in the established catalogue, qualified as weak and their average magnitude is about 2.8. Figure 4 shows the frequency of the recorded events according to their magnitude. Magnitude of most events varies between 2.6 and 3. It is obvious that the earthquake activity of the Serghaya fault during the studied 15 years has produced low magnitude events, in comparison with other parts of DSFS, such as Yammounah or Gulf of Aqaba. For example, 115 of the recorded events in 1995 in the Gulf of Aqaba have a magnitude greater than 4.0 (Jordan Seismological Observatory, 1995).

### Spatial clustering

Being of low magnitude, the recorded events were only observed by local stations located near Serghaya fault. In addition, the low magnitude of those events could affect the accuracy of the determination of wave-arrival times, hence the computed locations of the epicenters are not precise. A geographical distribution of these epicenters around Serghaya fault is presented in Figure 5. It is shown that those events extend from the divergence point of the Serghaya fault from the DSFS up to north-east Lebanon with a scattered pattern at both sides of Serghaya fault. Such a scattered distribution is justified by the low accuracy of the epicenter determination. Those events could probably occur on secondary faults, located near Serghaya fault. Although the scattered distribution of the epicenters, many spatial clusters can be observed. For

example: the cluster of tens of events at Deir el Acheir, the cluster of about 25 events at Ham, and the cluster of about 30 events north of Arsal (Figures 2 and 5). Some clusters could be related to the fault steps-over; e.g., at Deir el Acheir and Ham. Others clusters could be related to the Northern extension of Serghaya fault.

### Deir el Acheir clustering

Deir el Acheir region is nearly a Northward elongated basin, where, Serghaya fault spreads into two parallel branches at a distance of about 500 m (Figure 2). The left-stepping of Serghaya fault, observed at this elongated basin, suggests a pull-apart mechanism for the basin formation (Gómez *et al.*, 2001; 2003; Nemer *et al.*, 2008). The contact zone between Jurassic bedrock and Quaternary deposits, observed along the eastern branch, attests recent fault movements (Nemer *et al.*, 2008). The epicenter map (Figure 5) shows a clustering of events at Deir el Acheir (Figure 2). Some events in this cluster correspond to the micro earthquake activity that occurred on November 22<sup>nd</sup>, 1995, along the Serghaya fault. This remarkable activity has been regarded as a rare earthquake phenomenon. According to Mohamad *et al.*, (2000), this earthquake activity was triggered immediately following the 1995 Aqaba earthquake along the Serghaya fault at a distance of about 500 km, where a total of 21 events occurred during the first three and half hours following the mainshock. The focal plane solution of the largest event, of magnitude  $M_c 3.7$ , confirms the primary sinistral motion on Serghaya fault, predicted by local geology and plate tectonic considerations

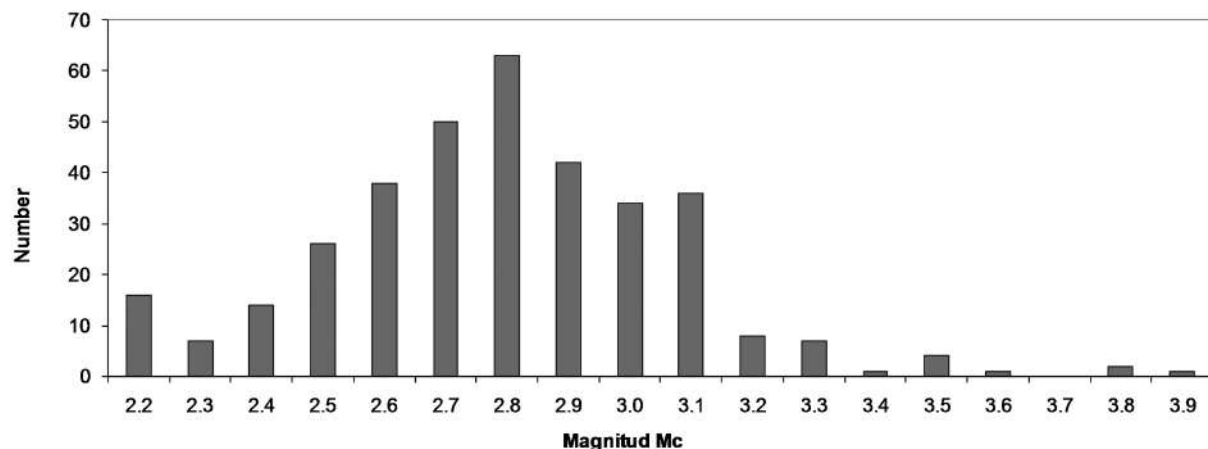


**Figure 4.** Distribution of recorded events according to their magnitude during the period of 1995-2009.

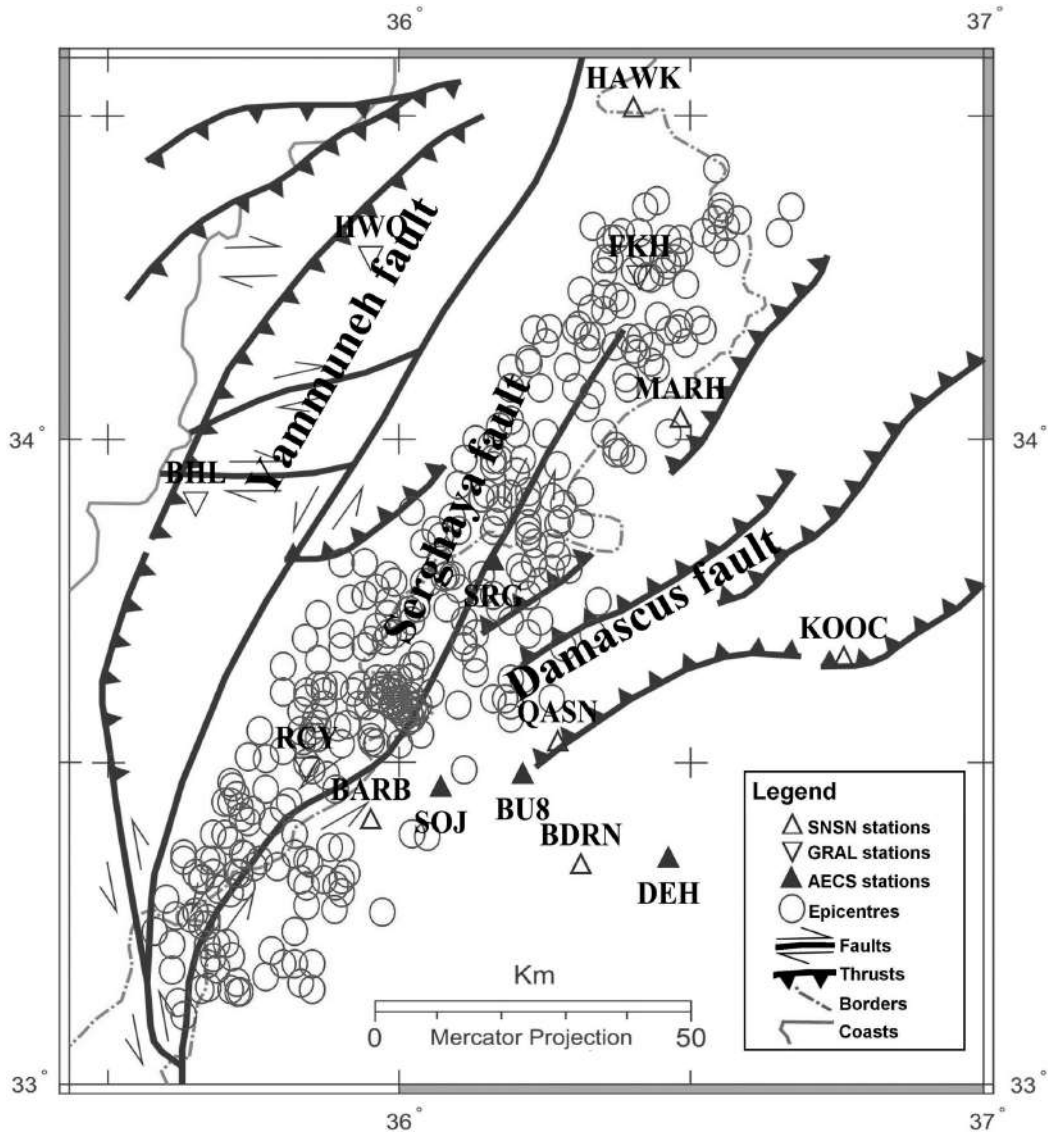


**Figure 5.** Geographical distribution of the earthquake epicentres around Serghaya fault during the period of 1995-2009.

(Gómez *et al.*, 2001; 2003; Meghraoui *et al.*, 2003; Abdul-Wahed and Al-Tahan, 2010; Abdul-Wahed *et al.*, 2011). The mechanisms for the small events of the Deir el Acheir cluster in 1995 were computed. Their uncertainty is large, but their variety provides valuable insights about the complexity of Serghaya fault and the structures along it (Figure 6). A good similarity can be observed between the fault plane solutions of events 1995/11/22-09:15:03.4 and 1995/11/22-09:15:33.9 in Figure 6. This similarity allows linking them with the sinistral Serghaya fault. In order to improve the quality of calculated mechanisms, the Composite Fault Plane Solution (CFPS) technique has been applied on those clustered small events. The advantages of the CFPS

technique are obvious: a better representative of the focal sphere is obtained by assembling further station/receiver pairs than when using only a single event (e.g., Evans *et al.*, 1985; Sato *et al.*, 2004). The CFPS has been applied on 9 micro-earthquakes from the 1995 cluster. The calculated composite focal mechanism (Figure 7) has shown exclusively strike slip faulting, where one fault plane solution is completely consistent with Serghaya fault. It demonstrates a good agreement with the fault sinistral motion.

#### Ham clustering

Ham region is also a Northward elongated basin, where, Serghaya fault spreads into

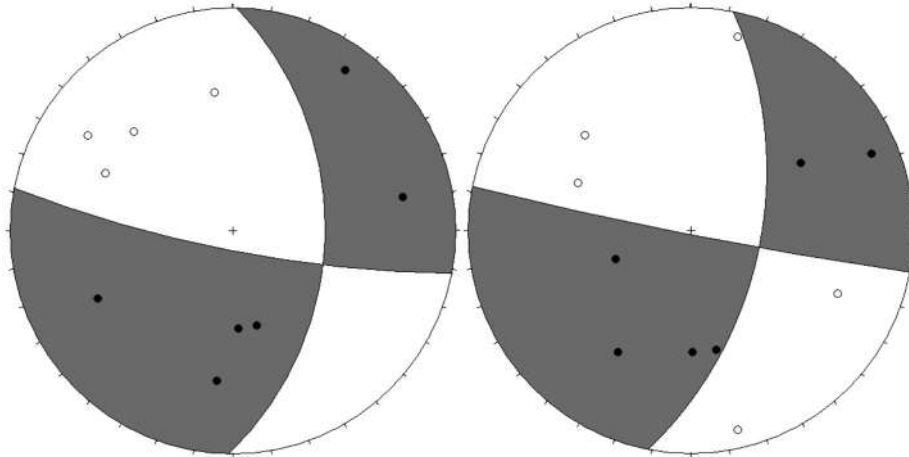


**Figure 6.** The fault plane solutions of the events 1995/11/22-09:15:03.4 (left) and 1995/11/22-09:15:33.9 (right) are presented with lower-hemisphere equal-area projection: white quadrants for dilatation and black for compression.

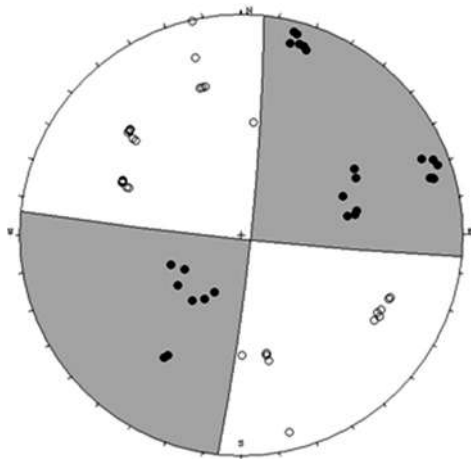


**Figure 7.** Composite focal mechanism of the biggest multiplet detected in Serghaya swarm. A good agreement was found between the fault plane solutions with NE Serghaya sinistral fault motion.

two parallel branches (Figure 2). Further northeastward, around Ham, the epicentral distribution (Figure 5) shows a cluster of about 25 events. In this region, the Serghaya fault bends to the north and steps approximately 500 m westward (Figure 2). Therefore, Ham basin could be considered as a pull-apart basin resulting from such stepping bend (Gómez *et al.*, 2001). The stepping segment is correlated with faulted rocks in soil matrix suggesting a recent fault movement (Nemer *et al.*, 2008). The cluster of about 25 events at Ham could be related to the recent faulting and the stepping bend of Serghaya fault at this region.

### Northern extension of Serghaya fault

The seismic activity in North Lebanon, shown on the epicenters map (Figure 5), is concentrated in the Hermel region (GRAL, 1995-2009). This activity could be related to the Northern extension of Serghaya fault (Figure 5). It displays a remarkable clustering of low-magnitude earthquakes. A cluster of about 30 events was observed around the village of Aarsal. It is aligned in NE until the village of Al-qa'a (Figure 2). The spatial distribution of this cluster could be associated to the northern part of Serghaya fault, which supports the finding of Walley (1998). Other cluster of ten events is observed near the Syrian-Lebanese borders and makes plausible the suggestion of linkage the Serghaya fault to the Jhar and Bishri faults (Figure 1) (Walley, 1998). It is probable to deduct that the Serghaya fault extends to the Hermel region, where this seismogenic zone could coincide with the proposed location of that linkage.

### Discussion and conclusion

The seismicity related to the Serghaya fault, during the period between 1995 and 2009, displays a remarkable clustering of low-magnitude earthquakes. The spatial and temporal clustering have been observed regardless the evolution of the seismic networks. The observed spatial clusters could be probably related to the fault steps-over; e.g., at Deir el Acheir and Ham. Some clusters, located in the Hermel region, indicate the activity of the Northern extension of Serghaya fault. It is possible to deduct that the Serghaya

fault extends to the Hermel region, where this seismogenic zone could coincide with the proposed location of linkage the Serghaya fault to the Jhar and Bishri faults, suggested by (Walley, 1998). Such evidence completes the findings of previous studies, which have demonstrated that the latest destructive earthquake was located on the Serghaya fault and could be younger than the earthquakes of Yammouneh fault. Therefore, Serghaya fault is, probably, the most plausible seismic source in Syria and Lebanon. The palaeoseismic investigations along the southern DSFS have, during the past decade, documented indications for long-term seismic behavior such as temporal clustering (e.g., El-Isa and Mustafa, 1986; Marco *et al.*, 1996; Zilberman *et al.*, 2000). The temporal clustering can be, therefore, an important characteristic of seismic activity along the DSFS. This clustering could have deep effects on the earthquake prediction. As discussed by Marco *et al.* (1996), temporal clustering of earthquakes may reflect a bias in 'earthquake cycle' for the northern part of DSFS. Several possible processes can cause temporal and space clustering such as the alternating periods of activity (Marco and Agnon, 2005). According to Ambraseys (1978), seismic activity has alternated between the North Anatolian and the East Anatolian major fault systems as a way of plate translation on longer time scales. The alternation phenomena might occur between the faults branches of DSFS in Lebanese restraining bend: Yammouneh, Roum, Hasbaya, Rachaya, and Serghaya faults. While a fault is active, the others store the elastic energy. The actual relative quiescence on Serghaya fault can be, therefore, regarded as alternating period of seismic activity with other faults within the Lebanese restraining bend.

### Acknowledgements

The authors are greatly indebted to Prof. Ibrahim Othman, Director General of the Atomic Energy Commission of Syria, for support this work.

### References

- Abdul-Wahed M.K., Asfahani J., Al-Tahan I., 2011, A combined methodology of multiplet and composite focal mechanism techniques for the identification of the seismological active zones in Syria. *Act. Geophys.*, 59, 967-992, DOI:10.2478/s11600-011-0024-2.
- Abdul-Wahed M.K., Al-Tahan I., 2010, Preliminary outlining of the seismological active zones in Syria. *Ann. Geophys.*, 53, 1-9.
- AECS bulletins, 1995-2009, Provisional Seismological Bulletin in Syria, internal reports, the Atomic Energy Commission of Syria (AECS), Damascus, Syria.
- Ambraseys N.N., Jackson J.A., 1998, Faulting associated with historical and recent earthquakes in the Eastern Mediterranean region. *Geophys. J. Int.*, 133, 390-406.
- Ambraseys N.N., 1978, Middle East: a reappraisal of the seismicity. *The Quarterly J. Engin. Geol.*, 11, 19-32.
- Asfahani J., Abdul-wahed M.K., 2013, Evaluation of Earthquake Activity Along the Serghaya Fault, Syria, from Instrumental Seismic Data, *Act. Geophys.*, 61, 1, 37-59, DOI: 10.2478/s11600-012-0059-z
- Baer G., Sandwell D., Williams S., Bock Y., Shamir G., 1999, Coseismic deformation associated with the November 1995, Mw=7.1 Nuweiba earthquake, Gulf of Elat (Aqaba), detected by synthetic aperture radar interferometry. *J. Geophys. Res.*, 104 B11, 25221-25232.
- Ben-Avraham Z., Schubert G., 2006, Deep "drop down" basin in the southern Dead Sea. *Earth Planet. Sci. Lett.* 251, 254-63.
- Brew G., Barazangi M., Al-Maleh A.K., Sawaf T., 2001, Tectonic and geologic evolution of Syria. *GeoArabia*, 6, 573-616.
- Bridgland D.R., Philip G., Westaway R., White M., 2003, A long Quaternary terrace sequence in the valley of the River Orontes, near Homs, Syria. *Current Science*, 84, 1080-1089.
- Butler R.W.H., Spencer S., Griffiths H.M., 1997, Trans current fault activity on the Dead Sea Transform in Lebanon and its implications for plate tectonics and seismic hazard. *Geolog. Soc. [London] J.* 154, 757-760.
- Daeron M., Klinger Y., Tapponnier P., Elias A., Jacques E., Sursock A., 2005, Sources of the large A.D. 1202 and 1759 Near East earthquakes. *Geology* 33, 7, 529-532; doi: 10.1130/G21352.1.
- Dakkak R., Daoud M., Mreish M., Hade G., 2005, The Syrian National Seismological Network (SNSN): Monitoring a major continental transform fault. *Seismolog. Res. Lett.*, 76, 437-445.
- Dubertret L. 1955, Carte géologique du Liban au 1:200000 avec notice explicative. République Libanaise, Ministère des travaux publics, 74 pp.

- El-Isa Z.H., Mustafa H., 1986, Earthquake deformations in the Lisan deposits and seismotectonic implications. *Geophys. J. R. Astron. Soc.*, 86, 413–424.
- Evans R., Asudeh I., Crampin S., 1985, Tectonics of the Maramara Sea region of Turkey: new evidence from micro-earthquake fault plane solutions. *Geophys. J. R. Astro. Soc.* 83, 47–60.
- GRAL bulletins, 1995-2009, Provisional Seismological Bulletin Geophysical Research Arrays of Lebanon from the National Seismic Network, The National Centre for Geophysical Research, Bhanne, National Council for Scientific Research, Lebanon.
- Gómez F., Karam G., Khawlie M., McClusky S., Vernant P., Reilinger R., Jaafar R., Tabet C., Khair K., Barazangi M., 2007, Global Positioning System measurements of strain accumulation and slip transfer through the restraining bend along the Dead Sea fault system in Lebanon. *Geophys. J. Int.*, 168, 1021–1028.
- Gómez F., Khawlie M., Tabet C., Darkal A. N., Khair K., Barazangi M., 2006, Late Cenozoic uplift along the northern Dead Sea transform in Lebanon and Syria. *Earth and Planet. Sci. Lett.*, 241, 913– 931
- Gómez F., Meghraoui M., Darkal A. N., Hijazi F., Mouty M., Suleiman Y., Sbeinati R., Darawcheh R., Al-Ghazzi R. and Barazangi M., 2003, "Holocene faulting & earthquake recurrence along the Serghaya branch of the Dead Sea fault system in Syria & Lebanon". *Geophys. J. Int.*, 153, 658-674,
- Gómez F., Meghraoui M., Darkal A.N., Sbeinati R., Darawcheh R., Tabet C., Khawlie M., Charabe M., Khair K., Barazangi M., 2001, Coseismic displacements along the Serghaya fault: an active branch of the Dead Sea fault system in Syria & Lebanon. *J. Geolog. Soc.*, 158, 405-40.
- Heimann A., Ron H., 1993, Geometric changes of plate boundaries along part of the northern Dead Sea Transform; geochronologic and paleomagnetic evidence. *Tectonics*, 12, 477–491.
- Jordan Seismological Observatory, 1995, Earthquakes in Jordan and adjacent areas, Nat. Res. Auth., *Jordan Seis. Obs., Bul.*, 27.
- Jordan Seismological Observatory, 1997, Earthquakes in Jordan and adjacent areas, Nat. Res. Auth., *Jordan Seis. Obs., Bul.*, No. 29.
- Klinger Y., Rivera L., Haessler H., Maurin J.-C., 1999, Active faulting in the Gulf of Aqaba: New knowledge from the Mw 7.3 earthquake of 22 November 1995. *Bull. Seism. Soc. Am.*, 89, 1025–1036.
- Kozlov V., Artemov A., Kalis A., 1963, Geological Map of the Trablus (I-36-XVIII) and Homs (I-37-XIII) Quadrangles, 1:200,000 Scale, and Accompanying Explanatory Guide. Vsesoj. Exportno-Import Objed. Technoexport, Moscow, and Ministry of Industry, Syrian Arab Republic, Damascus.
- Marco S., Stein M., Agnon A., Ron H., 1996, Long-term earthquake clustering: A 50,000-year paleoseismic record in the Dead Sea Graben. *J. Geophys. Res.*, 101, 6179–6192.
- Marco S., Agnon A., 2005, High-resolution stratigraphy reveals repeated earthquake faulting in the Masada Fault Zone, Dead Sea Transform. *Tectonophysics*, 408, 1-4, 101–112.
- McClusky S., Reilinger R., Mahmoud S., Ben Sari D. Tealeb A., 2003, GPS Constraints on Africa (Nubia) and Arabia plate motions. *Geophys. J. Int.*, 155, 1, 126–138, DOI: 10.1046/j.1365-246X.2003.02023.x
- Meghraoui M., Gómez F., Sbeinati R., van derWoerd J., Mouty M., Darkal A.N., Radwan Y., Layyous I., Al-Najjar H., Darawcheh R., Hijazi F., Al-Ghazzi R., Barazangi M., 2003, Evidence for 830 years of seismic quiescence from palaeoseismology, archeoseismology and historical seismicity along the Dead Sea fault in Syria. *Earth Planet. Sci. Lett.*, 210, 35–52.
- Mohamad R., Darkal A.N., Seber D., Sandvol E., Gómez F., Barazangi M., 2000, Remote earthquake triggering along the Dead Sea fault in Syria following the 1995 Gulf of Aqaba Earthquake (Ms = 7.3). *Seismolog. Res. Lett.*, 71, 47-52.
- Nemer T., Meghraoui M., Khair K., 2008, The Rachaya-Serghaya fault system (Lebanon): Evidence of coseismic ruptures, and the AD 1759 earthquake sequence. *J. Geophys. Res.*, 113, B05312, doi:10.1029/2007JB005090.
- Ponikarov V.P., Kazmin V.G., Mikhailov I.A., Razvaliyev A.V., Krashenninnikov V.A., Kozlov V.V., Souliidi-Kondratyev E.D., Faradzhev V.A., 1966, The Geological Map of Syria,

- 1:1,000,000: Scale, and Accompanying Explanatory Guide. Vsesoj. Exportno-Import Objed. Technoexport, Moscow, and Ministry of Industry, Syrian Arab Republic, Damascus.
- Salamon A., Hofstetter A., Garfunkel Z., Ron H., 2003, Seismotectonics of the Sinai subplate-The eastern Mediterranean region, *Geophys. J. Int.*, 155, 149–173.
- Sato Toshinori, Junzo K., Tuncay T., Masakazu I., Aya K., Tadaaki H., Onur T., 2004, A study of microearthquake seismicity and focal mechanisms within the Sea of Marmara (NW Turkey) using ocean bottom seismometers (OBSs). *Tectonophysics*, 391 303–314.
- Sbeinati M.R., Darawcheh R., Mouty M., 2005, The historical earthquakes of Syria: an analysis of large and moderate earthquakes from 1365 B.C. to 1900 A.D.. *Ann. Geophys.*, 48, 3, 347-435.
- SNSN Bulletins, 1995-2009, Bulletin of the Syrian National Seismological Network (SNSN), National Earthquake Center, Ministry of Petroleum and mineral resources, Syrian Arab Republic.
- Tapponnier P., Daeron M., King G., Jacques E., Sursock A., and Elias A., 2001, Active faulting and seismic hazard in Lebanon. *J. Conf. Abst.*, 6 (EUG XI).
- Walley C.D., 1998, Some outstanding issues in the geology of Lebanon and their importance in the tectonic evolution of the Levantine region. *Tectonophysics*, 298, 37–62.
- Walley C.D., 1988, A braided strike-slip model for the northern continuation of the Dead Sea Fault and its implications for Levantine tectonics. *Tectonophysics*, 145, 63–72.
- Westaway R., 1995, Deformation around stepovers in strike-slip fault zones. *J. Struct. Geol.*, 17, 831–846.
- Zilberman E., Amit R., Heimann A., Porat N., 2000. Changes in Holocene Paleoseismic activity in the Hula pull-apart basin, Dead Sea Rift, northern Israel. *Tectonophysics* 321, 2, 237–252.

## Paleoseismological uncertainty estimation in the Acambay region, Central Mexico

Quetzalcoatl Rodríguez-Pérez\*, F. Ramón Zúñiga and Pierre Lacan

Received: September 06, 2016; accepted: February 14, 2017 ; published on line: July 01, 2017

### Resumen

Los estudios paleosismológicos proporcionan información valiosa de los procesos de ruptura de los terremotos como son: las dimensiones de las fallas geológicas, los desplazamientos promedio y máximos, así como los tiempos de recurrencia y las magnitudes de eventos ocurridos en el pasado geológico. Esta información se basa en observaciones en los registros geológicos. La interpretación de dichas observaciones geológicas tienen una fuente de incertidumbres inherente al gran número de hipótesis que explican las características geológicas observadas. La información obtenida a partir de estudios paleosísmicos es importante en el análisis del riesgo sísmico y es crucial sobre todo para las regiones de baja actividad sísmica en donde el tiempo de recurrencia de los terremotos mayores alcanzan varios miles de años. Sin embargo, el uso de esta información en el análisis de riesgos requiere un tratamiento sistemático de las incertidumbres. En este estudio, se estimaron las incertidumbres de cuatro estudios paleosismológicos realizados en tres fallas geológicas diferentes en la región del graben de Acambay en el Centro de México. El método usado se basa en el formalismo de los árboles lógicos que cuantifica las incertidumbres acumuladas asociadas con las diferentes etapas de los estudios paleosismológicos aunado a una evaluación de la entropía en cada paso y al final del proceso. La incertidumbre final y su importancia relativa en el análisis de riesgo sísmico se expresa como el factor de calidad paleosísmico, el cual es de 0.14, 0.40-0.50 y 0.41 para las fallas de Acambay-Tixmadeje, Pastores y San Mateo, respectivamente. Estos valores se pueden incorporar en los análisis de riesgo sísmico para la región.

Palabras clave: Eje Neovolcánico, Acambay, Paleosismología, incertidumbres, riesgo sísmico, árbol lógico.

Q. Rodríguez-Pérez\*  
Consejo Nacional de Ciencia y Tecnología  
Dirección Adjunta de Desarrollo Científico  
Dirección de Cátedras  
Av. Insurgentes Sur 1582  
Col. Crédito Constructor 03940,  
Ciudad de México

\*Corresponding author: quetza@geociencias.unam.mx

### Abstract

Paleoseismological studies provide valuable information of the earthquake rupture processes such as fault dimensions, average and maximum displacements, as well as recurrence times and magnitudes of events which took place in the geologic past. This information is based on observations of the geological record. Interpretation of geological observations has a source of uncertainties inherent to the large number of hypothesis that explain the observed geological features. Information obtained from paleoseismic studies is important in seismic hazard analyses, and particularly crucial for regions of low seismic activity where the recurrence period of major earthquakes reaches several thousand years. However, using this information in hazard analysis requires the systematic treatment of uncertainties. We estimated uncertainties of four paleoseismological studies conducted at three different faults of the Acambay graben region in Central Mexico. The method used is based on a logic-tree formalism that quantifies the cumulative uncertainties associated with the different stages of the paleoseismic studies together with a quantification of the entropy at each step and at the end of the process. The final uncertainty and its relative importance in seismic hazard analysis is expressed as the paleoseismic quality factor, which indicate 0.14, 0.40-0.50, and 0.41 for the Acambay-Tixmadeje, Pastores and San Mateo faults, respectively. These values can be incorporated in seismic hazard analyses for the region.

Key words: Trans-Mexican Volcanic Belt, Acambay, Paleoseismology, uncertainties, seismic risk, logic-tree.

Q. Rodríguez-Pérez  
F. R. Zúñiga  
P. Lacan  
Centro de Geociencias  
Universidad Nacional Autónoma de México  
Blvd. Juriquilla No. 3001, 76230  
Juriquilla, Querétaro, México

## Introduction

Paleoseismological studies in Mexico are a recent development (e.g. Langridge *et al.*, 2000; Norini *et al.*, 2010; Garduño-Monroy *et al.*, 2009; Langridge *et al.*, 2013; Ortuño *et al.*, 2015; Sunye-Puchol *et al.*, 2015). They were mainly developed due to lack of instrumental data in regions of low strain rate, such as the Trans-Mexican Volcanic Belt (TMVB), notwithstanding the historical occurrence of large events such as the November 19 1912, Acambay earthquake ( $M_s$  6.7/ $m_b$  6.9; Urbina and Camacho, 1913; Abe, 1981), a moderate crustal normal-faulting event that caused widespread destruction and loss of lives at several towns near its epicenter (Urbina and Camacho, 1913; Singh *et al.*, 1984, 2011; Singh and Suárez, 1987). Other relevant shallow crustal events ( $M > 5$ ) at the TMVB are: the 1567/68 Ameca earthquake ( $M_w \sim 7.2$ ; Suter, 2015; Suárez *et al.*, 1996); the 1887 Pinal ( $m_b$  5.3; Suter, 1996); the 1920 Jalapa ( $M_s$  6.2/ $m_b$  6.5; Abe, 1981); the 1950

Ixmiquilpan ( $m_b$  5.0; Singh *et al.*, 1984); the 1976 Cardonal ( $m_b$  5.3; Mexican Seismological Service); and the 1979 Maravatío ( $m_b$  5.5; Astiz, 1980) earthquakes (Figure 1). These intraplate events pose a significant seismic hazard to people and infrastructure in Central Mexico, the most populated region in the country. The importance of the information extracted from paleoseismological studies in seismic hazard analysis highlights the need for systematic treatment of uncertainties. Interpretation of geological observations has a source of uncertainties inherent to large number of hypothesis that may explain the observed geological features. For example, the uncertainties which are related to the spatial observation window (at the scale of the trench) and the preservation of the geological record. In particular, breaking evolved along the fault however, in paleoseismological studies, it can only be observed as deformations preserved in the sedimentary record. Moreover, in Central Mexico, the differential compaction of surface sediments can produce structures that can be

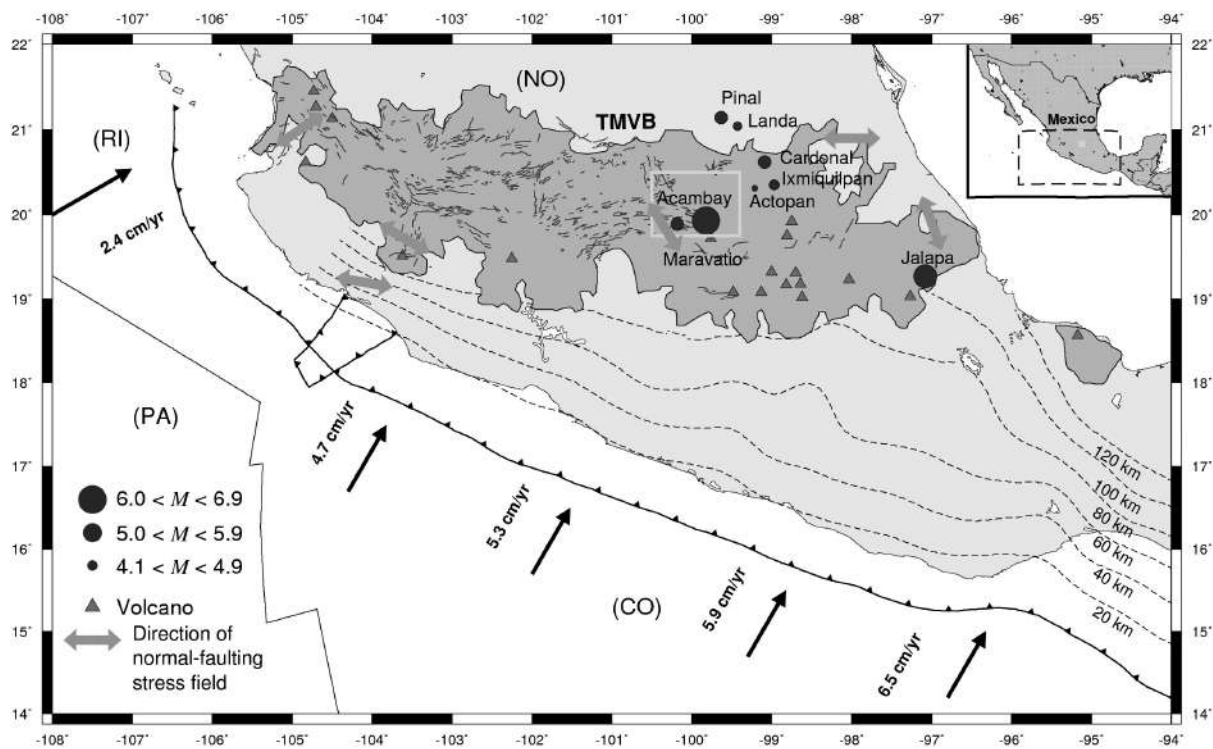


**Figure 1.** Main tectonic features in Central Mexico. NA is the North American plate, CO is the Cocos plate, PA is the Pacific plate, RI is the Rivera micro plate, and TMVB is the Trans-Mexican Volcanic Belt. Red triangles are volcanoes and the black-bold line delimits the boundary of the TMVB. Dashed lines show contour lines of the subducted slab at 20, 40, 60, 80 and 120 km depth (Hayes *et al.*, 2012). Gray circles are shallow crustal earthquakes in the TMVB with  $M > 4.1$  (Orozco and Berra, 1887; Urbina and Camacho, 1913; Astiz, 1980; Suter, 2015; and the Mexican Seismological Service). The size of the circle is proportional to the magnitude. The green rectangle shows the Acambay region. The arrows show the convergence rate relative to North America (DeMets *et al.*, 1994). Blue lines are geological faults in the TMVB reported in Ferrari *et al.* (2012). Orange arrows indicate direction of horizontal stress in provinces with a normal fault-type stress field based on Suter (1991).

interpreted, wrongly, as tectonic movements if the study areas are wrongly chosen. Finally, fractures without associated displacement can be wrongly interpreted as being associated with a seismic event on paleoseismological studies. However, without any other structural features described in the trench it can not be discarded that fractures could also be associated to other factors such as a distant earthquake, a period of drought, etc. This makes estimating the uncertainties related to paleoseismological data for their use in seismic hazard analysis a difficult task (Atakan *et al.*, 2000). To overcome these pitfalls, a detailed description of the source of paleoseismological data is needed (Atakan *et al.*, 2000). None of the paleoseismic studies in Mexico had tried to quantify a total uncertainty in their results. Using paleoseismic data in seismic hazard analysis without any uncertainty quantification may lead to a misinterpretation of the true seismic hazard. In this study, we applied the method proposed by Atakan *et al.* (2000) to estimate uncertainties in paleoseismic studies carried out in the Acambay graben region in Central Mexico. The method is based on logic-tree formalism and it has been applied in paleoseismological and archaeoseismological studies with success (Atakan *et al.*, 2000; Grützner *et al.*, 2010, respectively). Furthermore, we employ a measure of the information entropy (Shannon, 1948) at each step in the estimation to provide an additional source of validation of the results.

### Tectonic setting

The TMVB is an active calc-alkaline volcanic arc that traverses Mexico from the Pacific Ocean to the Gulf of Mexico (1200-km-long, 100-km-wide; Figure 1). The TMVB is associated with the subduction of the Cocos and Rivera plates beneath the North America plate (Suárez and Singh, 1986; Ego and Ansan, 2002; Figure 1). The crustal seismicity of this region is not related to the subduction along the Middle America Trench (MAT) but is due to numerous east-west striking normal faults that are characterized by pronounced scarps and displace Quaternary volcanic rocks (Suter *et al.*, 1992; 1995). The Acambay region is located at the central part of the TMVB; it consists of a series of depressions bounded by normal faults, such as the Acambay graben (Figure 2). The Acambay graben is up to 80 km long and 15-38 km wide and has a maximum topographic relief of 500 m (Suter *et al.*, 1992; 1995). The graben is delimited by the Epitacio-Huerta and Acambay-Tixmadejé faults to the north and by the, Venta de Bravo and Pastores faults, to the south (Figure 2). The Epitacio-Huerta fault is 30-km-long normal fault with E-W direction and dip to the south

but its activity has not been demonstrated. The Acambay-Tixmadejé fault is an approximately 42-km-long, south-dipping normal fault (Suter *et al.*, 1992) (Figure 2). The Acambay-Tixmadejé fault forms the master fault of the Acambay graben and was the principal seismogenic source of the 1912 Acambay earthquake (Urbina and Camacho, 1913). The Venta the Bravo is a 45-km-long active normal fault with E-W direction and dip to the north. The Pastores fault is a north-dipping active normal fault about 32-km-long (Suter *et al.*, 1992; Langridge *et al.*, 2013; Figure 2). The San Mateo fault is a 13 to 25-km-long active normal fault with E-W direction and dip to the south at the center of the graben (Sunye-Puchol *et al.*, 2015).

### Data and methods

#### Data

Paleoseismological studies on faults in Mexico concentrate mainly near the epicentral area of the Acambay 1912 earthquake (central segment of the TMVB; Figures 1 and 2), since that was one of the most damaging events occurred in the continental environment of Mexico notwithstanding other faults which have not ruptured in historical times. We used the method proposed by Atakan *et al.* (2000) to estimate uncertainties in paleoseismic studies in the Acambay graben region. We focus our analysis on the studies conducted by Langridge *et al.* (2000) on the Acambay-Tixmadejé fault; Langridge *et al.* (2013) and Ortuño *et al.* (2015) on the Pastores fault; and Sunye-Puchol *et al.* (2015) on the San Mateo fault (Figure 2). All the mentioned studies used trench evidence for identifying paleoearthquakes with a magnitude and time of occurrence, making them suitable for the methodology proposed by Atakan *et al.* (2000). The relevant data employed in the uncertainty estimation will be discussed in a subsequent section.

#### Uncertainty estimation

Atakan *et al.* (2000) introduced a method to estimate uncertainties in paleoseismic studies using a logic-tree formalism. The method is based on a quantitative description of uncertainties related to paleoseismological data and its interpretation. In this method, the cumulative uncertainties associated with different stages of the study are computed as the combination of the preferred alternative branches of the logic-tree. The total uncertainty and its relative importance in seismic hazard analysis is expressed by a quality factor, known as the paleoseismic quality factor (PQF). This PQF can be directly used in seismic hazard

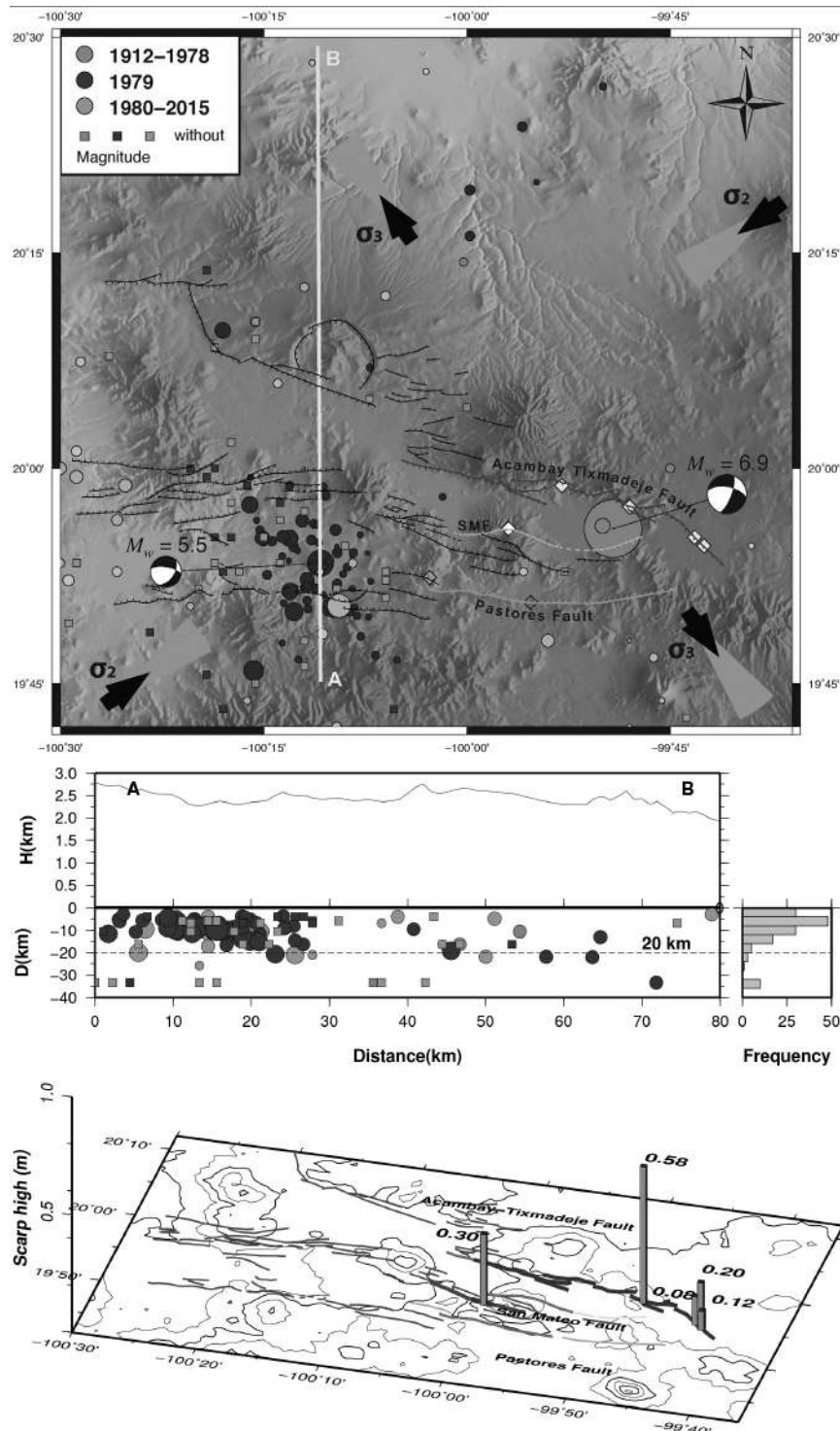


**Figure 2.** a) Main tectonic features in the Acambay region: the Acambay-Tixmadejé fault, the Pastores fault (PF), and the San Mateo fault (SMF). Diamonds are paleoseismological trench sites of Langridge *et al.* (2000) (yellow), Langridge *et al.* (2013) (magenta), Ortuño *et al.* (2015) (green), and Sunye-Puchol *et al.* (2015) (white). Focal mechanisms based on results of Astiz (1980) (Maravatio earthquake,  $M_w$  5.5) and fault orientation reported by Suter *et al.* (1995) and Langridge *et al.* (2000) (Acambay earthquake,  $M_w$  6.9). Thick black arrows indicate the direction of principal stresses with their uncertainty cone based on Ego and Ansan (2002). b) Most of the events in the region occur at depths less than 20 km (Cross-section AB). c) Major surface fault rupture for the 1912 event (blue bold line). Red bold lines show the interpreted extended fault rupture based on descriptions of Urbina and Camacho (1913) in adjacent areas. Vertical bars depict scarp heights reported by Urbina and Camacho (1913) and Langridge *et al.* (2000).

analysis and compared with other studies (Atakan *et al.*, 2000). The different study stages are represented as different nodes of the logic-tree. Each node has at least two alternative branches with their respective uncertainties. One branch represents the preferred solution and the other the sum of the remaining alternatives. The uncertainties are expressed in terms of probabilities assigned to each branch of the logic-tree. Eventually, a joint probability of the preferred alternatives will provide a qualitative measure of uncertainty of the paleoseismological analysis. According to Atakan *et al.* (2000), the relevant steps in the paleoseismic analysis are: 1) tectonic setting and strain-rate; 2) site selection criteria; 3) extrapolation of the conclusions drawn from the detailed site analysis to the entire fault; 4) identification of individual paleoearthquakes; 5) dating of paleoearthquakes; 6) paleoearthquake size estimates. In what follows, we summarize the main aspects of each step.

Atakan *et al.* (2000) classified the tectonic settings into three different categories. Each of them with an associated quality weight factor (QWF): plate boundaries (high strain-rate, QWF = 0.8 – 1.0); active plate interiors (intermediate strain-rate, QWF = 0.6 – 0.8); and stable continental regions (low strain-rate, QWF = 0.4 – 0.6). The site selection criteria take into account the methods used to select a site for detailed analysis. The site selection is mainly based on geomorphological information but according to the authors it should be supported by complementary studies. If the geomorphological evidence is supported by at least two or more geodetic and/or geophysical analyses, a QWF of 0.8 – 1.0 is assigned. If the geomorphological evidence is supported by an additional geodetic or geophysical study, a QWF of 0.6 – 0.8 is assigned. If only geomorphological is used, a QWF of 0.4 – 0.6 is assigned. If the selection is based on other indirect evidence, a weight of < 0.4 is assigned.

A criterion to assess the amount of extrapolation of site data to the entire fault is proposed. This criterion is based on the ratio of the total trench area studied to that of the entire fault area (TFR). TFR is defined as (Atakan *et al.*, 2000):

$$TRF = \frac{A_{st}}{A_f} = \frac{\sum_{i=1}^n (T_{li} \times T_{di})}{F_l \times F_d} \quad (1)$$

where  $A_{st}$  is the total area of the studied trenches,  $A_f$  is the total fault area,  $n$  is the number of

trenches used,  $T_{li}$  and  $T_{di}$  are the trench length and depth for the  $i$ -th trench, respectively,  $F_l$  is the fault length and  $F_d$  is the fault depth. Depending on the TFR value, a QWF is assigned. If TFR is in the interval of 0.5 – 1.0 (very good classification), QFW is equal to 0.8 – 1.0. If TFR ranges from 0.1 to 0.5 (good classification), QFW is equal to 0.6 – 0.8. If TFR varies from 0.01 to 0.1 (moderate classification), QFW is equal to 0.4 – 0.6. If TFR ranges from  $1 \times 10^{-6}$  to 0.01 (poor classification), QFW is equal to 0.2 – 0.4. If TFR is <  $1 \times 10^{-6}$  (very poor classification), QFW has a value of < 0.2. We estimated uncertainties in the TFR by using error propagation rules. Uncertainties in the TFR are mainly due to errors in  $F_l$  and  $F_d$ . We do not consider errors in the trench dimensions, because they are controlled parameters. We obtained the following expression to estimate the error factor in the TFR (dTFR):

$$dTFR = \frac{1}{F_l \times F_d} \sqrt{\frac{dF_l^2}{F_l^2} + \frac{dF_d^2}{F_d^2}} \quad (2)$$

where  $dF_l$  and  $dF_d$  are the uncertainties in the fault length and depth, respectively.

Paleoearthquake identification in the trenches is based on diagnostic criteria. These criteria are used to preclude the possibility of similar structures created by non-tectonic processes. The criteria consider the paleoseismic features defined by McCalpin and Nelson (1996) which focus on three aspects: genesis, location and timing, respectively. Based on the abundance of non-seismic features, a QWF is assigned: few (QWF = 0.8 – 1.0), some (QWF = 0.6 – 0.8), common (QWF = 0.4 – 0.6) and very common (QWF < 0.4) features, respectively. The uncertainties related to the dating of paleoearthquakes depend on the precision and accuracy of the techniques used. Estimating the size of the events is based on either primary or secondary evidence (Atakan *et al.*, 2000). Primary evidence includes the following criteria: seismic moment (QWF = 1.0); rupture area (QWF = 0.9); length x displacement, and average displacement (QWF = 0.8); surface-rupture length (QWF = 0.7); maximum displacement (QWF = 0.6). On the contrary, secondary evidence includes the following criteria: the total area affected by liquefaction (QWF = 0.5) and landslides (QWF = 0.4).

The QWFs are expressed in terms of percent probabilities indicating the relative reliability of the chosen (preferred) alternative. This allows

to account for uncertainties systematically. The concept of entropy has been used in information theory to characterize uncertainties in decision trees (Shannon, 1948). The entropy of a probability distribution ( $H$ ) is defined as (Shannon, 1948):

$$H(p) = -\sum_{i=1}^n p_i \log_2(p_i) \quad (3)$$

where  $p_i$  are the probabilities.  $H$  ranges from 0 to 1 where high  $H$  is associated with high uncertainty and viceversa. We also quantified the conditional entropy in order to estimate uncertainties in tree nodes conditioned on a particular probability value in previous branches (stages in paleoseismology analysis). The conditional entropy is defined as:

$$H(A/B) = -\sum_{i=1}^n \sum_{j=1}^m p(a,b) \log_2 p(a/b) \quad (4)$$

where  $a$  and  $b$  are two random variables.

The cumulative uncertainties provide an end solution (probability) in terms of the paleoseismic quality factor (PQF). PQF is defined as:

$$PQF = P_{es} \cdot C_{ri} \quad (5)$$

where  $P_{es}$  is the probability of the preferred end-solution, in the logic-tree analysis,  $C_{ri}$  is a correction term for the relative level of importance of the investigation in the seismic hazard analysis.  $C_{ri}$  depends on the aim of the paleoseismic study (see Table 1).

### Input parameters for paleoseismological uncertainty analysis

We briefly present the main results of previous studies that were used as input parameters for the uncertainty estimation analysis. Table 2 summarizes the relevant results for the Acambay-Tixmadejé (ATF), San Mateo (SMF) and Pastores (PF) faults.

Case study 1 (Acambay-Tixmadejé fault): The Acambay-Tixmadejé fault is situated in a continental plate interior, where the strain-rate is classified under the intermediate strain-rate category (about 0.17 mm/yr) (Langridge *et al.*, 2000). The site selection was based on geomorphological information and on the location of the surface fault rupture (Urbina and Camacho, 1913). Fault length and depth are 42 and 15 km, respectively. Table 2 shows the number of trenches and their dimensions. The diagnostic features observed in the trenches were of primary origin on the fault and co-seismic. The evidence used to identify the events was based on disturbed stratigraphic horizons and colluvial wedges indicating vertical offset. Langridge *et al.* (2000) used  $^{14}\text{C}$  to determine the date of the organic material from the sedimentary deposits in the trenches. At least four events of about the same magnitude ( $M \sim 7.0$ ) were recognized by a combination of upward terminating faults, fissure fills, erosionally truncated fissures, colluvial wedges fills, and downward separation of stratigraphic units. These events occurred in the last 34.3 ky cal BP, 11.5 ky cal BP, 7.9 ky cal BP, and 4.7 – 5.2 ky cal BP, respectively. Langridge *et al.* (2000) reported magnitudes in the range of  $6.8 < M_w < 7.0$  based on maximum and average displacements and surface rupture length.

**Table 1.** Correction terms  $C_{ri}$  (After Atakan *et al.*, 2000).

Correction term $C_{ri}$	Level of importance	Aim of the study
2	level 1	The results are used for estimating time recurrence and magnitudes in local seismic hazard analysis.
4	level 2	The results are used for estimating time recurrence and magnitudes in regional seismic hazard analysis.
6	level 3	The results reported in an event catalogue and used in the computation of seismic parameters.
8	level 4	To assess the earthquake potential of a fault. The results will not be used directly in the seismic hazard analysis.
10	level 5	To prove that the fault is active.

Case study 2 (Pastores fault): The Pastores fault is also located in a continental plate interior, where the strain-rate is classified under the intermediate strain-rate category ( $< 0.04$  mm/yr in the central fault segment, Suter *et al.*, 1995; and  $0.23 - 0.37$  mm/yr at the western fault tip, Ortuño *et al.*, 2015) (Figure 2). The site selection was based on geomorphological evidence supported by a ground penetrating radar (GPR) prospecting (Langridge *et al.*, 2013; Ortuño *et al.*, 2015). Fault length and depth are 32 and 15 km, respectively. Table 2 shows the number of trenches and their dimensions. The diagnostic features observed in the trenches were of primary origin on the fault and co-seismic. The evidence used to identify the events was based on disturbed stratigraphic horizons and colluvial wedges indicating vertical offset (Langridge *et al.*, 2013; Ortuño *et al.*, 2015). Both used  $^{14}\text{C}$  to determine the date of the organic material from the sedimentary deposits in the trenches. In the central fault segment, three paleoearthquakes were identified (Langridge *et al.*, 2013). The events occurred at

$12.2 - 23.9$  ky cal BP,  $23.9 - 34.6$  ky cal BP, and  $31.5 - 41.0$  ky cal BP, respectively. The average recurrence time is about  $10 - 15$  ky cal BP (Langridge *et al.*, 2013). At the western fault tip, five paleoearthquakes were identified within the past 4 ky (Ortuño *et al.*, 2015). A recurrence interval of  $1.1 - 2.6$  ky cal was inferred (Ortuño *et al.*, 2015). Langridge *et al.* (2013) reported magnitudes of  $6.4 < M_w < 6.8$  for the paleoearthquakes based on maximum displacement and surface rupture. Ortuño *et al.* (2015) reported magnitudes of 5.8 based on the scaling relationships of Wells and Coppersmith (1994) for average displacement of normal fault events at the western end. The magnitudes were also estimated with the scaling relations of Wesnousky (2008), obtaining magnitudes of about  $M_w \sim 6.7$ .

Case study 3 (San Mateo fault): The San Mateo fault is located in a continental plate interior as the other cases, and the strain-rate is classified under the intermediate strain-rate category ( $0.060 - 0.11$  mm/yr, Sunye-Puchol *et al.*, 2015). The site selection was

**Table 2.** Input parameters

N	Parameter	ATF	PF	SMF
1	Strain rate (mm/yr)	0.17	$< 0.04$ central segment $0.23-0.37$ western tip	0.06-0.11
2	Site selection	-geomorphic -surface fault rupture	-geomorphic -GPR survey	-geomorphic
3	Fault length (km)	42	32	25
4	Fault depth (km)	15	15	15
5	Number of trenches	4	4	2
6	Trench dimensions (length $\times$ depth )(m)	$14 \times 2$ $120 \times 1.7$ $30 \times 3.75$ $30 \times 4.0$	$28 \times 3$ $24 \times 4$ $15 \times 3$ $47 \times 3$	$15 \times 3$ $24 \times 4$
7	Diagnostic features	on-fault coseismic	on-fault coseismic	on-fault coseismic
8	Dating method	numerical $^{14}\text{C}$	numerical $^{14}\text{C}$	numerical $^{14}\text{C}$
9	Earthquake size	$6.8 < M_w < 7.0$	$6.4 < M_w < 6.8$	$6.4 < M_w < 6.7$
10	Magnitude criteria	maximum and average displacement -rupture surface length	-maximum displacement -rupture surface length	-maximum displacement -rupture surface length

ATF is the Acambay-Tixmadejé fault; PF is the Pastores fault; SMF is the San Mateo fault.

**Table 3.** Results

Parameters	QWF interval	Assigned QWF	Observations	Fault
Intermediate strain rate	0.6 – 0.8	0.8	Fault scarp visible along 40 km	ATF
	0.6 – 0.8	0.7	Fault scarp for 5 km/ buried structures	PF
	0.6 – 0.8	0.8	Fault scarp visible over 10 km	SMF
Site selection criteria	0.4 – 0.6	0.8	Geomorphic-fault rupture	ATF
	0.4 – 0.8	0.8	Geomorphic/geophysical	PF
	0.4 – 0.6	0.6	Geomorphic only	SMF
TFR	< 0.2	0.2	Very poor classification	ATF
	< 0.2	0.2	Very poor classification	PF
	< 0.2	0.2	Very poor classification	SMF
Non-seismic features	0.8 – 1.0	0.9	Few	ATF
	0.8 – 1.0	1.0	Few	PF
	0.8 – 1.0	1.0	Few	SMF
Dating method	0.8 – 1.0	0.8	Isotopic/numerical	ATF
	0.8 – 1.0	0.8	Isotopic/numerical	PF
	0.8 – 1.0	0.8	Isotopic/numerical	SMF
Magnitude estimate	0.6 – 0.8	0.7	Mean/maximum/rupture length	ATF
	0.6 – 0.7	0.7	Maximum/rupture length	PF
	0.6 – 0.7	0.7	Maximum/rupture length	SMF

ATF is the Acambay-Tixmadejé fault; PF is the Pastores fault; SMF is the San Mateo fault.

based only on geomorphological evidence (Sunye-Puchol *et al.*, 2015). Fault length and depth are 25 and 15 km, respectively. Table 2 shows the number of trenches and their dimensions. The diagnostic features observed in the trenches were of primary origin on the fault and co-seismic. The evidence used to identify the events was based on disturbed stratigraphic horizons and colluvial wedges indicating vertical offset (Sunye-Puchol *et al.*, 2015). Sunye-Puchol *et al.* (2015) used  $^{14}\text{C}$  to determine the date of the organic material from sedimentary deposits in the trenches. The dating results indicated that in total, three paleoearthquakes were identified (Sunye-Puchol *et al.*, 2015). These events occurred in the last 31 – 29.2 ky cal BP, 19.1 – 6.5 ky cal BP and 6.0 – 4.2 ky cal BP, respectively (Sunye-Puchol *et al.*, 2015). A recurrence interval of  $11.57 \pm 5.32$  ky cal BP was inferred (Sunye-Puchol *et al.*, 2015). Sunye-Puchol *et al.* (2015) reported magnitudes in the range of  $6.4 < M_w < 6.7$  based on maximum displacement and surface rupture length of 13 km.

## Results and Discussion

The results are presented for individual faults and then we discuss the advantages and possible drawbacks in the paleoseismology uncertainty method. The assigned QWFs in all the logic tree stages are listed in Table 3. Uncertainties in TFR are estimated with the following assumptions:  $F_l = 42 \pm 2$  km and  $F_d = 15 \pm 5$  km;  $F_l = 32 \pm 4$  km and  $F_d = 15 \pm 5$  km;  $F_l = 13 \pm 7$  km and  $F_d = 15 \pm 5$  km for the Acambay-Tixmadejé, Pastores and San Mateo faults, respectively. Estimations of  $F_d$  are based on reported seismicity in the Acambay region (Figure 2b). The calculated TFR with uncertainties are:  $(7.37 \pm 2.48) \times 10^{-7}$ ,  $(7.62 \pm 2.71) \times 10^{-7}$  and  $(3.76 \pm 2.19) \times 10^{-7}$  for the Acambay-Tixmadejé, Pastores and San Mateo faults, respectively. All the results belong to the very poor class according to the classification of Atakan *et al.* (2000). These errors represent 34, 36 and 58% of the TFR value for the ATF, PF and SMF, respectively.

Applying the logic-tree formalism, the probability of the preferred end solution in the analysis is found to be  $P_{es} = 0.0681$  (Figure 3) for the Acambay-Tixmadejé fault. The study conducted by Langridge *et al.* (2000) focused on characterizing typical events in terms of magnitude and time recurrence in the Acambay-Tixmadejé fault, thus a  $C_{ri}$  of 2 is assigned (Table 1 and Figure 3). Accordingly, we obtain a PQF of 0.14. For the case of the Pastores fault, we obtained a  $P_{es}$  of 0.0502 (Figure 3). Langridge *et al.* (2013) stated that the aim of their study is to assess the earthquake potential of the Pastores fault, thus a  $C_{ri}$  of 8 is assigned (Table 1 and Figure 3). This gives a  $PQF_1$  of 0.40. The study conducted by Ortuño *et al.* (2015) focused on the activity of the Pastores fault, thus a  $C_{ri}$  of 10 is also assigned (Table 1 and Figure 3). Accordingly, the  $PQF_2$  is 0.50. In the case of the San Mateo fault, the probability of the preferred end solution in the analysis is  $P_{es} = 0.0511$  (Figure 3). Sunye-Puchol *et al.* (2015) stated that the aim of their study is to assess the earthquake

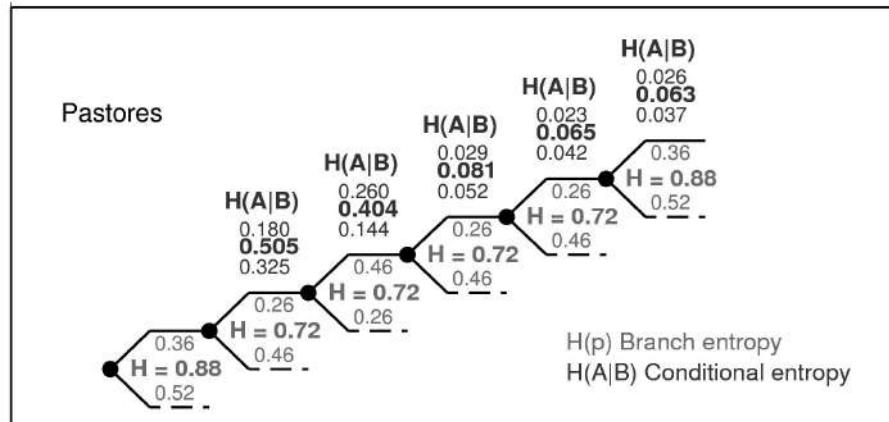
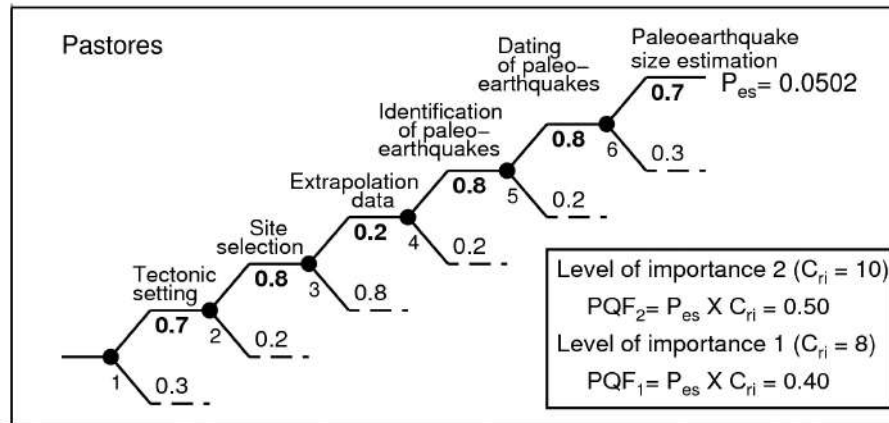
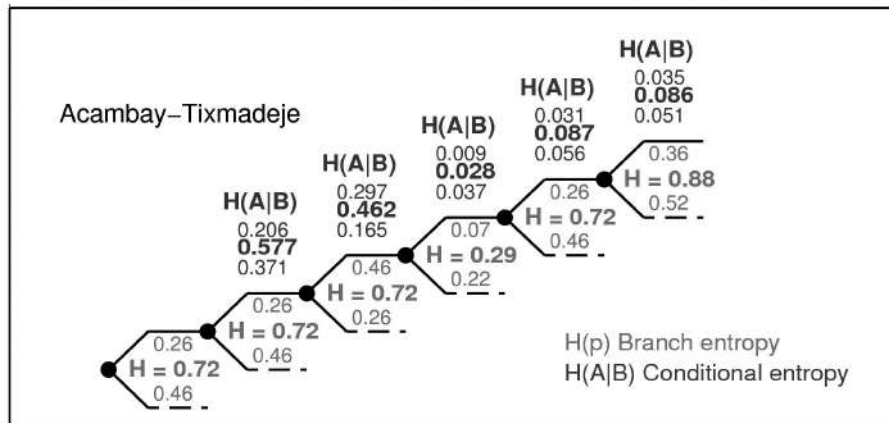
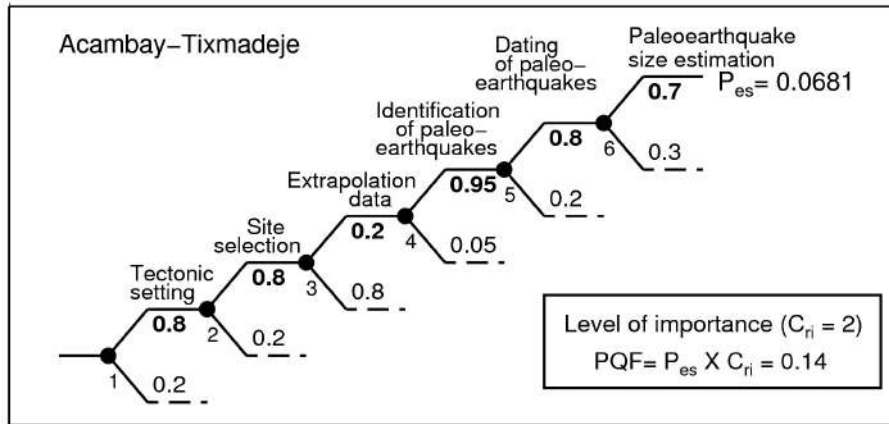
potential of the San Mateo fault, thus a  $C_{ri}$  of 8 is assigned (Table 1 and Figure 3). For this case, we get a PQF of 0.41.

Comparing the entropy, the lowest entropy values are related to the identification of the paleoevents stage (Figure 3a and 3c and Table 4) for the preferred branch and the mean entropy at the ATF and SMF. For these faults the conditional entropy showed a similar behavior throughout the stages (Figure 3a and 3c and Table 4). The correct identification of paleoearthquakes seems to be a key step in estimating uncertainties as is also seen in the Pastores fault case. A QWF of 0.8 in this stage produces significant fluctuations in the entropy of the tree (Table 4). The conditional entropy in the last tree node represents the uncertainty at the end of the paleoseismological study. This final entropy is lower than the conditional entropy in the first two study stages (for example in the site selection and extrapolation data steps) (Figure 3). By incorporating more stages with relative good QWFs, the conditional entropy decreases

**Table 4.** Entropy analysis

Fault	Stage	Branch 1	Branch 2	$H_1$	$H_2$	$H$	$H_1(A B)$	$H_2(A B)$	$H(A B)$
ATF	1	0.80	0.20	0.26	0.46	0.72			
	2	0.80	0.20	0.26	0.46	0.72	0.206	0.371	0.577 H(2 1)
	3	0.20	0.80	0.46	0.26	0.72	0.297	0.165	0.462 H(3 1,2)
	4	0.95	0.05	0.07	0.22	0.29	0.009	0.028	0.037 H(4 1,2,3)
	5	0.80	0.20	0.26	0.46	0.72	0.031	0.056	0.087 H(5 1,2,3,4)
	6	0.70	0.30	0.36	0.52	0.88	0.035	0.051	0.086 H(6 1,2,3,4,5)
PF	1	0.70	0.30	0.36	0.52	0.88			
	2	0.80	0.20	0.26	0.46	0.72	0.180	0.325	0.505 H(2 1)
	3	0.20	0.80	0.46	0.26	0.72	0.260	0.144	0.404 H(3 1,2)
	4	0.80	0.20	0.26	0.46	0.72	0.029	0.052	0.081 H(4 1,2,3)
	5	0.80	0.20	0.26	0.46	0.72	0.023	0.042	0.065 H(5 1,2,3,4)
	6	0.70	0.30	0.36	0.52	0.88	0.026	0.037	0.063 H(6 1,2,3,4,5)
SMF	1	0.80	0.20	0.26	0.46	0.72			
	2	0.60	0.40	0.44	0.53	0.97	0.354	0.423	0.777 H(2 1)
	3	0.20	0.80	0.46	0.26	0.72	0.223	0.124	0.347 H(3 1,2)
	4	0.95	0.05	0.07	0.22	0.29	0.007	0.021	0.028 H(4 1,2,3)
	5	0.80	0.20	0.26	0.46	0.72	0.023	0.042	0.065 H(5 1,2,3,4)
	6	0.70	0.30	0.36	0.52	0.88	0.026	0.038	0.064 H(6 1,2,3,4,5)

ATF is the Acambay-Tixmadejé fault; PF is the Pastores fault; SMF is the San Mateo fault.  $H_1$  and  $H_2$  are the entropy in branches 1 and 2, respectively.  $H$  is the mean entropy.  $H_1(A|B)$  and  $H_2(A|B)$  are the conditional entropies in branches 1 and 2, respectively.  $H(A|B)$  is the mean conditional entropy.



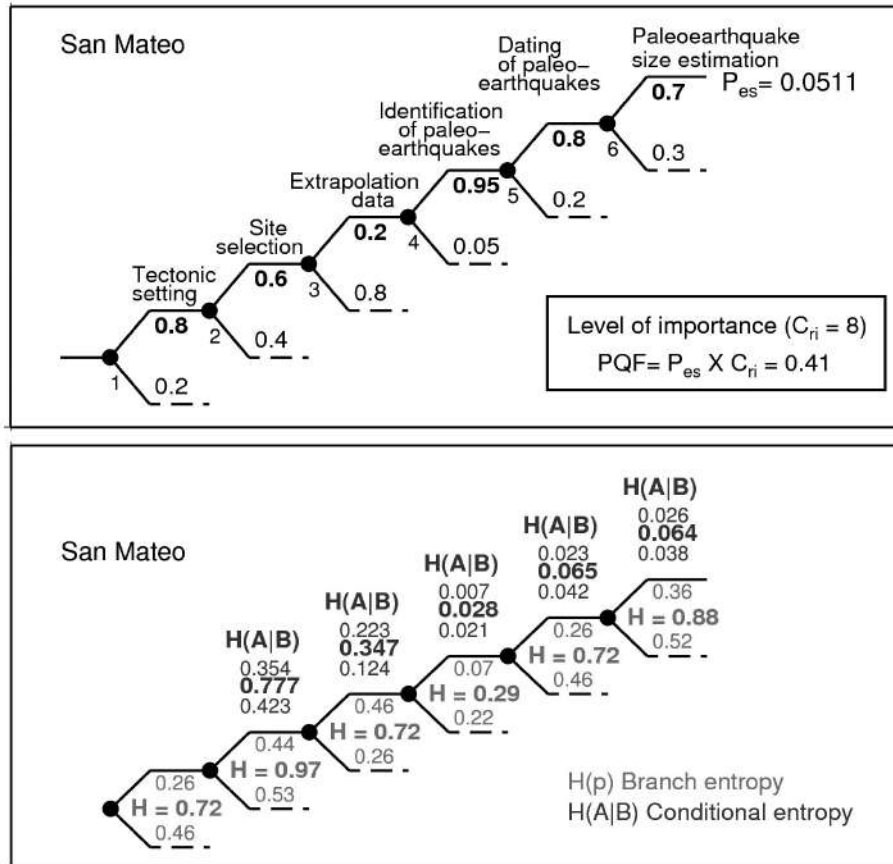


**Figure 3.** Paleoseismology logic-trees for the Acambay-Tixmadejé, Pastores and San Mateo faults. The logic-trees consist of 12 branches and 6 nodes at which certain probabilities must be defined. The result is the probability of the preferred end solution ( $P_{es}$ ). In this study,  $P_{es}$  is 0.0681, 0.0502 and 0.0511 for the Acambay-Tixmadejé, Pastores and San Mateo faults, respectively. The paleoseismic quality factor (PQF) is  $P_{es} \times C_{ri}$  ( $C_{ri}$  is a correction term depending on the level of importance of the study). PQF is 0.14, 0.40-0.50, and 0.41 for the Acambay-Tixmadejé, Pastores and San Mateo faults, respectively. Estimations of entropy for each branch is shown in the lower panels of a), b) and c) in red colors. Mean entropies are shown bold red color (middle value). Conditional entropy for each branch (upper and lower values) and the average (middle value) are indicated in blue color. Upper values represent the preferred branch.

as shown in Table 4 and Figure 3. This highlights the importance of adding more stages in the paleoseismological studies resulting in more complex logic trees.

Paleoseismology has to deal with many uncertainties caused in particular by limitations in site selection and earthquake identification. Subjective evaluations are inherent in paleoseismic studies, thus the quantification of uncertainty is necessary to address this problem. The logic trees are first attempts to quantify uncertainties that are often hard to express in numbers, and this approach reaches its limits at certain points. Some nodes of the logic trees are based on a number of different criteria, which allow calculations of a

wide range of probability values. For example the estimation of QWF for intermediate strain-rate tectonic environments ( $0.6 < QWF < 0.8$ ). Additionally, the paleoseismological logic-tree is mainly designed to investigate faults and related coseismic surface ruptures and hardly incorporates the large variety of secondary earthquake ground effects (e.g. ground failure, liquefaction, landslides). Atakan *et al.* (2000) mentioned that some of the uncertainties that are not considered in their analysis are: 1) those related with the completeness of the paleoseismic records; and 2) aspects concerning the time evolution of different processes involved rupture process. For example, the difficulties in matching the long-term deformation rates with the

co-seismic slip and whether the maximum observed slip at fault is a result of a single or several paleoearthquakes. These aspects can be implemented in the logic-tree analysis but they are difficult to quantify. For future refined studies, these and other aspects would have to be taken into consideration, at least comparatively, to account for the peculiarity of the different studies areas. In the particular case of the Acambay graben, some important factors that are not taken into account by the logic-tree methodology proposed by Atakan *et al.* (2000), are: 1) the data relative to the 1912 earthquake rupture along the Acambay-Tixmadejé fault; 2) the width of the fault zone that may influence the distribution of deformation on unstudied secondary faults; 3) the completeness of the sedimentary record in the trench that directly controls the completeness of the record of paleoseismological events identified.

We now analyze possible sources for the low level of classification of the paleoseismological studies conducted in the Acambay region obtained through the logic tree scheme. One disadvantage of these studies is that few were supported by complementary geodetic and/or geophysical methods. The identification of suitable places for trenching was mostly based on geomorphological evidence. Only one study used a complementary method to the paleoseismic analysis (see Ortuño *et al.*, 2015). The advantage of the studies, on the other hand, was that they used numerical dating techniques and they provided a complete description of the diagnostic criteria employed at each trench. A key point in seismic hazard analysis, is the magnitude estimation of the paleoevents. Most of the estimated magnitudes were based on the scaling relationships of Wells and Coppersmith (1994). These relations have been shown to be a poor approximation to magnitudes in certain regions (Stirling *et al.*, 2013), such as continental ones. The studies do not specify the valid magnitude range of these relations. For example, Ortuño *et al.* (2015) reported magnitudes of about 5.8 considering average displacement on the Pastores fault using relations developed for events in the magnitude range of  $6.0 < M < 7.3$ . Another source of low uncertainty of the analyzed studies concerns the extrapolation of site data to the entire fault, since most of them were carried out at single point in the fault, so they fall under the very poor qualitative classification following the rules of Atakan *et al.* (2000) (Table 1). They, nevertheless, provide data of utmost importance since no other source of information was available previous to these studies, which could be used towards a comprehensive evaluation of risk in the region.

Because of the lack of similar studies and the absence of sufficient estimations of PQFs values for different regions, a robust comparison of our results in a logic-tree framework was not possible. We can just state that by incorporating geophysical/geodetic studies, and by analyzing more trenches, a better PQF can be obtained resulting in more reliable results for the Acambay region. For example, under these conditions Atakan *et al.* (2000) obtained better estimates of PQF (PQF = 0.76). More studies are needed to compare different tectonic settings and to prove whether the logic tree approach is suitable method to quantify uncertainties in paleoseismological studies. This comparison could be possible because the logic-tree approach takes into account the tectonic setting and site environment in the probability estimations. A direct comparison of several studies in a certain region may enhance the reliability of the results (Sintubin and Stewart, 2008; Grützner *et al.*, 2010). Grützner *et al.* (2010) suggested the incorporation of secondary earthquake ground effects and their relation to ground geotechnical properties and seismic amplification in the logic tree approaches. This will allow to conduct more realistic assessments of non-faulted sites devastated by ground shaking which is the case for most of the severely damaged locations during individual earthquakes (Grützner *et al.*, 2010). In the case of the Acambay region, a detailed study of site effects is needed to improve our uncertainty estimates and seismic hazard assessment. Nevertheless, the logic-tree formalism proposed by Atakan *et al.* (2000) is prone to improvement by considering other aspects currently not taken into account, or investigating the effect of different weights on the tree branches.

## Conclusions

We estimated uncertainties of paleoseismic studies conducted in the Acambay-Tixmadejé, Pastores, Venta de Bravo and San Mateo faults. We focus on the following steps of the paleoseismic analysis: 1) tectonic setting and strain-rate; 2) site selection; 3) extrapolation of site data to the entire fault; 4) identification of paleoearthquakes; 5) dating of paleoearthquakes and 6) event size estimates. The main results are: 1) In the Acambay region, the probability of the preferred end solution is 0.0681, 0.0502 and 0.0511 for the Acambay-Tixmadejé, Pastores and San Mateo faults, respectively; 2) The paleoseismic quality factor is 0.14, 0.40-0.50, and 0.41 for the Acambay-Tixmadejé, Pastores and San Mateo faults, respectively. These values indicate that the paleoseismic results fall in the very poor to

poor category according to the description of Atakan *et al.* (2000). This implies that better estimates could be attained if complementary studies were carried out at each fault, as well as additional trenching studies. The results, however, do not undermine the importance of all the paleoseismic data collected so far since they are the first steps ever taken in the direction of knowing the seismic potential of faults in Central Mexico, and provide key elements for a correct evaluation of risk in the region. The entropy results showed that the study stage with less uncertainty is associated with the identification of paleoearthquakes. This stage seems to be a key step in estimating uncertainties because QWFs less than 0.8 produce significant fluctuations in the entropy of the logic tree. On the other hand, the entropy conditioned on previous steps is higher at the first two stages (site selection and extrapolation data steps) then it reduces due to the incorporation of more stages (branches) with high QWFs as shown by the results. In the Acambay region, more careful have to be taken in the site selection and extrapolation data stages in order to reduce the entropy and thus the uncertainties in the paleoseismological studies.

### Acknowledgments

Quetzalcoatl Rodríguez-Pérez was supported by the Mexican National Council for Science and Technology (CONACYT) (Catedras program-project 1126). This work was carried out with the support of UNAM PAPIIT projects No. IA101615 and IN108115. We used the UNIPAS software (Toiran and Atakan, 1999) for uncertainty analysis.

### References

- Abe K., 1981, Magnitude of large shallow earthquakes from 1904 to 1980. *Phys. Earth Planet. Inter.*, 27, 72-92.
- Astiz L.M., 1980, Sismicidad en Acambay, Estado de México. El temblor del 22 de febrero de 1979. B.Sc. Thesis, Universidad nacional Autónoma de México, Mexico City, 130 pp.
- Atakan K., Midzi V., Moreno Toiran B., Vanneste K., Camelbeeck T., Meghraoui M., 2000, Seismic hazard in regions of present day low seismic activity: uncertainties in the paleoseismic investigations along the Bree Fault Scarp (Roer Graben, Belgium). *Soil Dyn. Earthq. Eng.*, 20, 415-427.
- Ego F., Ansan V., 2002, Why the Central Trans-Mexican Volcanic Belt (102° -99° W) in transtensive deformation?, *Tectonophys.*, 359, 189-208.
- Ferrari L., Orozco-Esquivel T., Manea V., Manea M., 2012, The dynamic history of the Trans-Mexican Volcanic Belt and the Mexico subduction zone. *Tectonophys.*, 522, 122-149.
- Garduño-Monroy V.H., Pérez-Lopez R., Israde-Alcantara I., Rodríguez-Pascua M.A., Szykaruk E., Hernández-Madrigal V.M., García-Zepeda M.L., Corona-Chávez P., Ostroumov M., Medina-Vega V.H., García-Estrada G., Carranza O., Lopez-Granados E., Mora-Chaparro J.C., 2009, Paleoseismology of the southwestern Morelia-Acambay fault system, central Mexico. *Geofis. Int.*, 48, 319-335.
- Grützner C., Reicherter K., Silva P.G., 2010, Comparing semiquantitative logic trees for archaeoseismology and paleoseismology: The Baelo Claudia (southern Spain) case study, *in* Sintubin, M., Stewart I.S., Niemi T.M., Altunel E., eds., Ancient Earthquakes: *Geolog. Soc. Am. Special Pap.*, 471, 129-143.
- Langridge R.M., Weldon II R.J., Moya J.C., Suárez G., 2000, Paleoseismology of the 1912 Acambay earthquake and the Acambay-Tixmadejé fault, Trans-Mexican Volcanic Belt. *J. Geophys. Res.*, 105, 3019-3037.
- Langridge R.M., Persaud M., Zúñiga F.R., Aguirre-Díaz G.J., Villamor P., Lacan P., 2013, Preliminary paleoseismic results from the Pastores fault and its role in the seismic hazard of the Acambay graben, Trans-Mexican Volcanic Belt, Mexico. *Rev. Mex. Cienc. Geol.*, 30, 463-481.
- McCalpin J.P., Nelson A.R., 1996, Introduction to paleoseismology. In: McCalpin JP, editor. *Paleoseismology*. Academic Press Inc, San Diego, USA, 1-32pp.
- Norini G., Capra L., Borselli L., Zúñiga R., Sarocchi D., 2010, Large scale landslides triggered by Quaternary tectonics in the Acambay graben, Mexico. *Earth Surf. Proc. Land*, doi: 10.1002/esp.1987.
- Ortuño M., Zúñiga F.R., Aguirre-Díaz G.J., Carreón-Freyre D., Cerca M., Roverato M., 2015, Holocene paleo-earthquakes recorded at the transfer zone of two major faults: the Pastores and Venta de Bravo faults (Trans-Mexican Volcanic Belt). *Geosphere*, 11, 160-184.

- Shannon C., 1948, A mathematical theory of communication. *Bell Sys. Tech. J.*, 27, 379-423.
- Singh S.K., Rodríguez M., Espíndola J.M., 1984, A catalog of shallow earthquakes of Mexico from 1900 to 1981. *Bull. Seismol. Soc. Am.*, 74, 267-279.
- Singh S.K., Suárez G., 1987, Overview of the seismicity of Mexico with emphasis on the September 1985 Michoacan earthquake, in Cassaro M.A., Martínez-Romero E., eds., Proc. Int. Conf. Am. Civil Eng. Soc., The Mexico Earthquakes-1985: Factors Involved and Lessons Learned, *Am. Civil Eng. Soc.*, 7-18.
- Singh S.K., Iglesias A., Ordaz M., Pérez-Campos X., Quintanar L., 2011, Estimation of ground motion in Mexico City from a repeat of the  $M \sim 7.0$  Acambay earthquake of 1912. *Bull. Seismol. Soc. Am.*, 101, 2015-2028.
- Sintubin M., Stewart I.S., 2008, A logical methodology for archeoseismology: A proof of concept at the archeological site of Sagalassos, southwest Turkey. *Bull. Seismol. Soc. Am.*, 98, 2209-2230.
- Stirling M., Goded T, Berryman K, Litchfield N (2013) Selection of earthquake scaling relationships for seismic-hazard analysis. *Bull. Seismol. Soc. Am.*, 103, 2993-3011.
- Suárez G., García-Acosta V., Gaulon R., 1994, Active crustal deformation in the Jalisco block, Mexico: evidence for a great historical earthquake in the 16<sup>th</sup> century. *Tectonophys.*, 234, 1-2, 117-127.
- Suárez G., Singh S.K., 1986, Tectonic interpretation of the Trans-Mexican Volcanic Belt- Discussion. *Tectonophys.*, 127, 155-160.
- Sunye-Puchol I., Lacan P., Ortuño M., Villamor P., Audin L., Zúñiga F.R., Langridge R.M., Aguirre-Díaz G.J., Lawton T.F., 2015, The San Mateo Fault, new paleoseismological evidence of an active faulting in the Acambay graben, Mexico (In Spanish). *Rev. Mex. Cienc. Geol.*, 32, 361-375.
- Suter M., 1991. State of stress and active deformation in Mexico and western Central America, in *Neotectonics of North America*, D. B. Slemmons, et al. (Editors), Geological Society, Boulder Colorado, Decade Map., 1401-1421.
- Suter M., Quintero O., Johnson C.A., 1992, Active faults and state of stress in the central part of the Trans-Mexican Volcanic Belt, Mexico, I. The Venta de Bravo fault. *J. Geophys. Res.*, 97, 11983-11993.
- Suter M., Quintero-Legorreta O., López-Martínez M., Aguirre-Díaz G., Ferrar E., 1995, The Acambay graben: active intra-arc extension in the Trans-Mexican Volcanic Belt, Mexico. *Tectonics*, 14, 1245-1262.
- Suter M., Carrillo-Martínez M., Quintero-Legorreta O., 1996, Macro seismic study of shallow earthquakes in the Central and Eastern parts of the Trans-Mexican Volcanic Belt, Mexico. *Bull. Seismol. Soc. Am.*, 86, 1952-1963.
- Suter M., 2015, The A.D. 1567  $M_w$  7.2 Ameca, Jalisco, earthquake (Western Trans-Mexican Volcanic Belt): surface rupture parameters, seismological effects, and macro seismic intensities from historical sources. *Bull. Seismol. Soc. Am.*, 105, 646-656.
- Toirán-Moreno B., Atakan K., 1999, Uncertainties in paleoseismology UNIPAS. A computer software for systematic treatment of uncertainties in paleoseismology. UNIPAS V2.0 Program. University of Bergen.
- Urbina F., Camacho H., 1913, La zona megasísmica Acambay Tixmadejé, Estado de Mexico, conmovida el 19 de noviembre de 1912. *Bol. Inst. Geol. Mexico*, 32, 125pp.
- Wells D.L., Coppersmith K.J., 1994, New empirical relationships among magnitude rupture length, rupture width, rupture area, and surface displacement. *Bull. Seismol. Soc. Am.*, 75, 939-964.
- Wesnousky S.G., 2008, Displacement and geometrical characteristics of earthquake surface ruptures: issues and implications for seismic-hazard analysis and the process of earthquake rupture. *Bull. Seismol. Soc. Am.*, 98, 1609-1633.

## Observations of remotely triggered seismicity in Salton Sea and Coso geothermal regions, Southern California, USA, after big ( $M_w > 7.8$ ) teleseismic earthquakes

Raúl R. Castro\*, Robert Clayton, Egill Hauksson and Joann Stock

Received: September 27, 2016; accepted: January 08, 2017; published on line: July 01, 2017

### Resumen

Se analizó un catálogo de sismos relocalizados en las regiones cercanas a los campos geotérmicos de Coso y Salton Sea, en el sur de California, USA, para investigar posibles cambios en la tasa de sismicidad durante y después de telesismos grandes ( $M_w > 7.8$ ). Se estudió la sismicidad de estas dos regiones usando ventanas de 30 días previos y posteriores a la ocurrencia de cinco grandes sismos: el de Denali, Alaska del 2002 ( $M_w 7.9$ ); el de Sumatra-Andaman del 2004 ( $M_w 9.2$ ); el de Chile del 2010 ( $M_w 8.8$ ); el de Tohoku-Oki, Japón del 2011 ( $M_w 9.1$ ); y el del norte de Sumatra del 2012 ( $M_w 8.6$ ).

El sismo de Denali ( $M_w 7.9$ ) coincide con un incremento de la sismicidad en la región del Salton Sea cuando este evento remoto ocurrió, indicando que el disparo instantáneo de la sismicidad está posiblemente relacionado con el paso de las ondas superficiales en esta región. En la región del campo geotérmico Coso la tasa de sismicidad permaneció aproximadamente constante durante el periodo de 30 días de observación. La sismicidad después del sismo de Sumatra-Andaman del 2004 ( $M_w 9.2$ )

incrementó en las dos regiones 9 días después de este mega-evento. La sismicidad después del sismo de Chile del 2010 ( $M_w 8.8$ ) incrementó en ambas regiones aproximadamente 14 días después de la ocurrencia de este telesismo. La sismicidad en las regiones de Salton Sea y de Coso incrementaron 17 y 14 días, respectivamente, después del terremoto de Japón del 2011 ( $M_w 9.1$ ), lo que sugiere que el disparo retrasado de la sismicidad fue inducido después del paso de las ondas superficiales en ambas regiones. De manera similar el sismo del norte de Sumatra del 2012 ( $M_w 8.6$ ) disparó sismicidad 6 y 16 días después en las regiones de Salton Sea y Coso, respectivamente. Estas observaciones se pueden interpretar como evidencia de disparo dinámico retrasado inducido por sismos grandes y remotos. Encontramos que la magnitud máxima de los enjambres sísmicos disparados incrementa con el tamaño ( $M_0/\Delta$ ) de los mega-sismos y que cuando el tamaño de estos se incrementa, el tiempo de retraso también aumenta.

Palabras clave: disparo remoto, sismicidad del sur de California, USA, campo geotérmico Coso, campo geotérmico Salton Sea.

---

R. R. Castro\*  
CICESE  
Departamento de Sismología  
Ensenada, Baja California  
México,  
\*Corresponding author: raul@cicese.mx

R. Clayton  
E. Hauksson  
J. Stock  
CALTECH  
Seismological Laboratory  
Pasadena, California, USA

## Abstract

A relocated catalog was used to search for changes in seismicity rate in the Salton Sea and the Coso geothermal regions, southern California, USA, during and after large ( $M_w > 7.8$ ) teleseismic earthquakes. Seismicity in these two regions was analyzed within 30-day windows before and after the occurrence of five major earthquakes: the 2002 Denali fault, Alaska ( $M_w 7.9$ ); the 2004 Sumatra-Andaman ( $M_w 9.2$ ); the 2010 Central Chile ( $M_w 8.8$ ); the 2011 Tohoku-Oki, Japan ( $M_w 9.1$ ); and the 2012 Offshore Northern Sumatra ( $M_w 8.6$ ) earthquakes.

The Denali ( $M_w 7.9$ ) earthquake coincided with an increase in seismicity in the Salton Sea region the day when this remote event occurred, indicating that instantaneous triggered seismicity was likely related with the passage of its surface waves. However, in the Coso region the seismicity rate remained approximately constant during the 30-day observation period. The seismicity after the 2004 Sumatra-Andaman ( $M_w 9.2$ ) earthquake

increased in both regions 9 days after the mega-earthquake. The seismicity after the 2010 Chile ( $M_w 8.8$ ) earthquake increased in both regions approximately 14 days after the remote event. The seismicity in Salton Sea and Coso regions increased 17 and 14 days, respectively, after the 2011 Japan ( $M_w 9.1$ ) earthquake, suggesting that delayed triggered seismicity was induced after the passage of the surface waves in both regions. Similarly, 6 and 16 days after the 2012 northern Sumatra ( $M_w 8.6$ ) earthquake the seismicity also increased in Salton Sea and Coso regions, respectively. These observations can be interpreted as evidence of instantaneous and delayed dynamic triggering induced by large remote earthquakes. The maximum magnitude of the delayed triggered swarm increased with the strength ( $M_0/\Delta$ ) of the mega-earthquake and, the stronger the remote earthquake, the longer the delay time.

**Key words:** remote triggering, seismicity southern California, USA, Coso geothermal field, Salton Sea geothermal field.

## Introduction

Since the 1992,  $M_w 7.3$  Landers earthquake, several studies have documented that large distant earthquakes can dynamically trigger seismicity (Hill *et al.*, 1993; Anderson *et al.* 1994; Gomberg and Bodin, 1994; Hill and Prejean, 2007; Peng and Gomberg, 2010), particularly in volcanic and geothermal regions. Velasco *et al.* (2008) and Jiang *et al.* (2010) showed that the dynamic stress generated by both Rayleigh and Love waves can increase significantly the crustal stress in active regions, which can trigger micro-earthquakes. Based on the analysis of dynamic stress associated with the fundamental mode of Rayleigh and Love waves (Hill, 2008), the triggering potential of the surface waves was defined by Gonzalez-Huizar and Velasco (2011) as the change of the Coulomb failure function caused by the passage of the seismic wave. The triggering potential depends also on the faulting mechanism that is being triggered. The physical processes of dynamic triggering have been related with geothermal activity, including magma intrusions, movement of magmatic fluids and bubble excitation (Hill *et al.*, 1993; Linde and Sacks, 1998). Long-period waves that generate fluid flow can lead to high-pressure oscillations (Brodsky and Prejean, 2005) and likely temporal variations of seismicity.

Withdrawal and injection of fluids can also change pore pressure and modify normal stress driving local faults to failure (Hubbert and Rubey, 1959). Seismicity induced in geothermal fields has been analyzed in Coso (Feng and Lees, 1998) and Salton Sea (Brodsky and Lajoie, 2013) regions, USA. More recently Trugman *et al.* (2016) studied long-term changes in seismicity at these two regions and found that the seismicity rate in both of them correlates with fluid withdrawal and injection only before 1990, during the beginning of the geothermal field operations.

In the present study, temporal variations of local seismicity are analyzed in two geothermal related regions, the Coso Range and the Salton Sea, before and after the occurrence of five major earthquakes: the 2002 Denali fault, Alaska ( $M_w 7.9$ ); the 2004 Banda Ache, Sumatra-Andaman ( $M_w 9.2$ ); the 2010 Central Chile ( $M_w 8.8$ ); the 2011 Tohoku-Oki, Japan ( $M_w 9.1$ ); and the 2012 northern Sumatra ( $M_w 8.6$ ) earthquakes. In particular, the time delay between the origin time of large remote earthquakes and the triggered seismicity variation with the strength ( $M_0/\Delta$ ) of the teleseismic events and these with the maximum magnitude of the triggered earthquake swarm are analyzed.

## Tectonic framework

### *The Coso Geothermal Region*

The Coso geothermal field is located in a releasing bend in a right-lateral fault system west of Death Valley, north of the Mojave Desert and east of southern Owens valley (Monastero *et al.*, 2005). The location of the Coso range, the main topographic features of the region and the seismicity analyzed are displayed in the map of Figure 1. The Coso Geothermal Field (CGF) is located in the central zone of the Range and is one of the most seismically active regions in central California, USA (Bhattacharyya and Lees, 2002). The Coso Range has a high level of seismicity, resulting from dextral transtension along the eastern margin of the Sierra Nevada microplate and other processes related to the

CGF. Moderate size earthquakes have occurred in this region in the past, for instance, from 1981 to 2005 several events with  $M \leq 5.8$  were reported by Hauksson *et al.* (1995) near Ridgecrest. Remotely triggered seismicity has been reported previously at Coso after the 1992 Landers earthquake (Hill *et al.*, 1993), and by other large teleseismic earthquakes like the 2002 Denali fault earthquake (Prejean *et al.*, 2004). Aiken and Peng (2014) analyzed local earthquakes triggered by distant earthquakes with magnitudes greater than 5.5 that occurred in the Coso Geothermal Field between 2000 and 2012. They found that the triggering frequency of local earthquakes in Coso varied 3.8% in the 12 year period analyzed, and that the stress triggering threshold is approximately 1 KPa in this region.

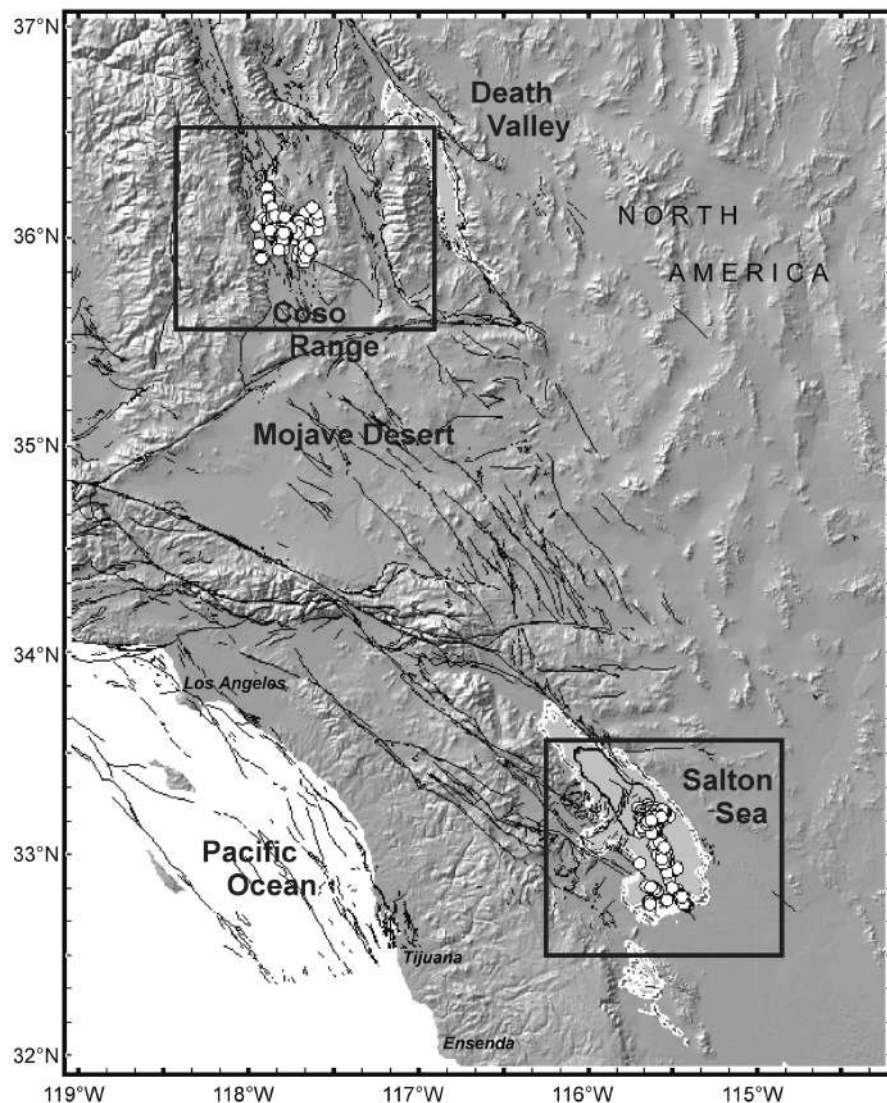


**Figure 1.** Location of regions studied (Coso and Salton Sea) and seismicity taken from the Hauksson-Yang-Shearer Alternative catalog of Southern California. The topography and bathymetry are from GeoMap App (Ryan *et al.*, 2009). The boxes delimit the two regions of interest shown in Figures 2 and 3.

### Salton Sea

Oblique extension in this region of southern California originated the Salton Trough, a topographic depression (endorheic basin) that links the San Andreas Fault system to the Gulf of California rift system (Elders *et al.*, 1972; Stock and Hodges, 1989). The basin includes the Coachella, Imperial, and Mexicali Valleys, and contains the sub-sea-level Salton Sea in the central depression. Main transform faults of the depression included the Imperial fault, the Cerro Prieto Fault, and the southern San Andreas Fault. The Salton Sea Geothermal Field is located in the extensional step-over between the San Andreas and Imperial faults (Muffler and White, 1969). Earthquake swarms are generated frequently in the spreading centers south of Salton Sea but the largest earthquakes occur on the main transform faults (Doser and Kanamori, 1986; Hauksson, 2011). The underlying crust consists of sediments and new oceanic crust (Fuis *et al.*, 1984; Barak *et al.*, 2015), with higher heat flow than in the neighboring ranges (Lachenbruch *et al.*, 1985). The sediments of the Imperial Valley have a thickness of 5-6 km grading into metamorphic rocks (Fuis *et al.*, 1984; Barak *et al.*, 2015). The Salton Sea Basin and the Laguna Salada Basin, the regions with the lowest elevation in the Salton Trough, have the lowest upper mantle velocities, suggesting a connection between rift-related subsidence and deep magmatic activity (Barak *et al.*, 2015). Previous studies in this region (Hough and Kanamori, 2002; Doran *et al.*, 2011) have observed remote triggering of seismicity.

### Data and method

Previous studies of triggered seismicity in southern California (e.g. Prejean *et al.*, 2004) have used the standard Southern California Seismic Network (SCSN) earthquake catalog. We used the 2011-Hauksson-Yang-Shearer alternative catalog for Southern California (Hauksson *et al.*, 2012; Lin *et al.*, 2007) to analyze temporal changes of seismicity after the occurrence of the five mega earthquakes mentioned above. This catalog contains hypocentral coordinates relocated from the SCSN data base from 1981 and recently updated to 2014. Quarry blasts have been removed from this alternative catalog. The relocation procedure accounts for local variations in the velocity structure by applying various techniques in post-processing of the data. The absolute picks combined with the differential travel times are applied to improve the relative locations within clusters of similar events. Trugman *et al.* (2016) estimated the minimum magnitude

of completion of this catalog and found that for the years 1981-2013 the catalog is complete above magnitude 2.0 for Salton Sea and above 1.5 for Coso.

From the alternative catalog events that occurred between October 2002 and May 2012 in the Coso region (35.87N-36.25N and 117.5W-118.0W) and in the Salton Sea region (32.75N-33.25N and 115.25W-115.70W) (Figure 1) were selected to analyze temporal seismicity variations for 30-day periods before and after the five big teleseismic events.

For the Coso region only shallow events (focal depth less or equal to 3 km) were selected for the analyses because these events are more likely related to the geothermal activity in this region. Approximately 60% of the events reported by the SCSN catalog have focal depths less than 3 km in the Coso Range and 30% have depths between 3 and 6 km. The rest of the events (~10%) have focal depths between 6 and 12 km. Hauksson and Unruh (2007) found localized low *P*- and *S*-wave velocity zones beneath the central Coso Range at 0-3 km depth that image the geothermal reservoir.

The local earthquakes that occurred in the Coso region in the 30 day periods before each of the remote earthquakes are displayed with light dots in Figure 2 and with dark dots the local events that occurred in the subsequent 30 days. The seismicity after the remote earthquakes (dark dots) seems to follow the same distribution pattern as the pre-event seismicity, suggesting that the seismicity triggered zones were already active. Similarly, Figure 3 shows the location of the earthquakes in the Salton Sea region for the 30-day periods before and after the remote earthquakes. The seismicity that presumably triggered after the passage of surface waves (dark dots) tends to concentrate near the Salton Sea geothermal field, located in the north of the studied area. In particular, before the 2012 Offshore Northern Sumatra  $M_w$ 8.6 earthquake, the seismicity near the Salton Sea (light dots in Figure 3e) was distributed along the Imperial fault and in the Brawley seismic zone on a conjugate-fault trending NE-SW. Then, after the remote event most of the local earthquakes concentrated along the NE-SW direction, in the Salton Buttes area (site of Holocene volcanism; Schmitt *et al.*, 2013) presumably in a small spreading center. This suggests that the tectonic stress had been concentrating in that zone before the mega-earthquake and that the dynamic stress increased the existing stress enough to trigger the seismicity where more stress had accumulated.

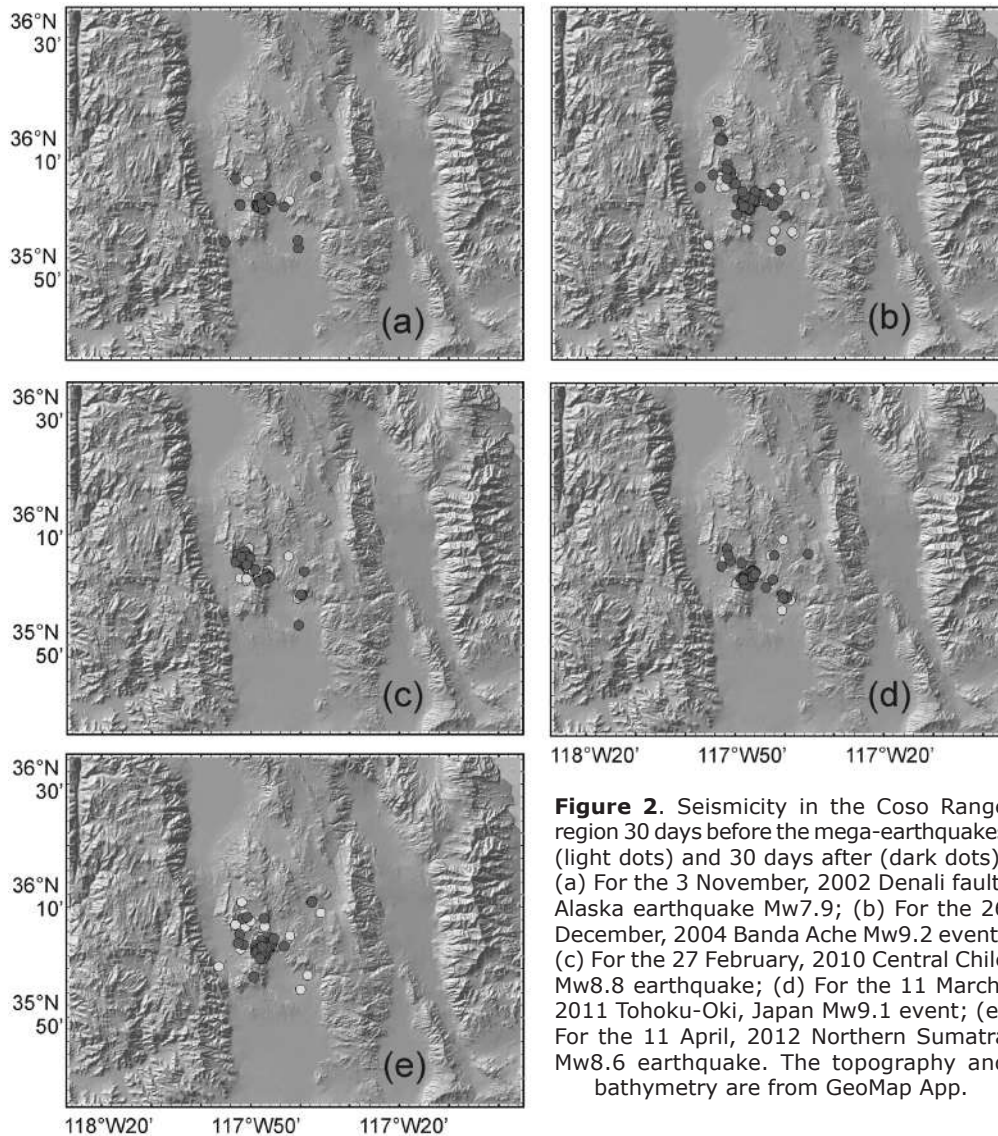


**Figure 2.** Seismicity in the Coso Range region 30 days before the mega-earthquakes (light dots) and 30 days after (dark dots). (a) For the 3 November, 2002 Denali fault, Alaska earthquake Mw7.9; (b) For the 26 December, 2004 Banda Ache Mw9.2 event; (c) For the 27 February, 2010 Central Chile Mw8.8 earthquake; (d) For the 11 March, 2011 Tohoku-Oki, Japan Mw9.1 event; (e) For the 11 April, 2012 Northern Sumatra Mw8.6 earthquake. The topography and bathymetry are from GeoMap App.

To quantify the statistical significance of seismicity rate changes, we compute  $\beta$ -statistics. This statistical parameter has been used before (e.g. Aron and Hardebeck, 2009) to compare the difference between the number of events occurring in a given time period and the expected number of events in that time period for a constant seismicity rate, normalized by the standard deviation (Matthews and Reasenberg, 1988).

The  $\beta$ -statistic is defined as:

$$\beta = \frac{N_i - NT_i / T}{N \frac{T_i}{T} \sqrt{1 - \frac{T_i}{T}}} \quad (1)$$

where  $T_i$  is the duration of the time period of interest and  $T$  is the duration of the whole

catalog.  $N_i$  and  $N$  are the number of events in the time period of interest and the total number of events, respectively. For  $|\beta| \geq 1.64$ , the difference in seismicity rate between the two time periods is significant at 90% confidence; for  $|\beta| \geq 1.96$ , it is at 95% confidence, and for  $|\beta| \geq 2.57$ , it is significant at 99% confidence.

**Data sets: triggered seismicity**

The number of local events per day that occurred within a 30-day period before and after the remote mega-earthquakes selected is displayed in Figures 4 and 5 for the Coso Range and the Salton Sea regions, respectively. These figures illustrate the temporal variability of the seismicity rate. Time zero corresponds to the day when the remote earthquake occurred.

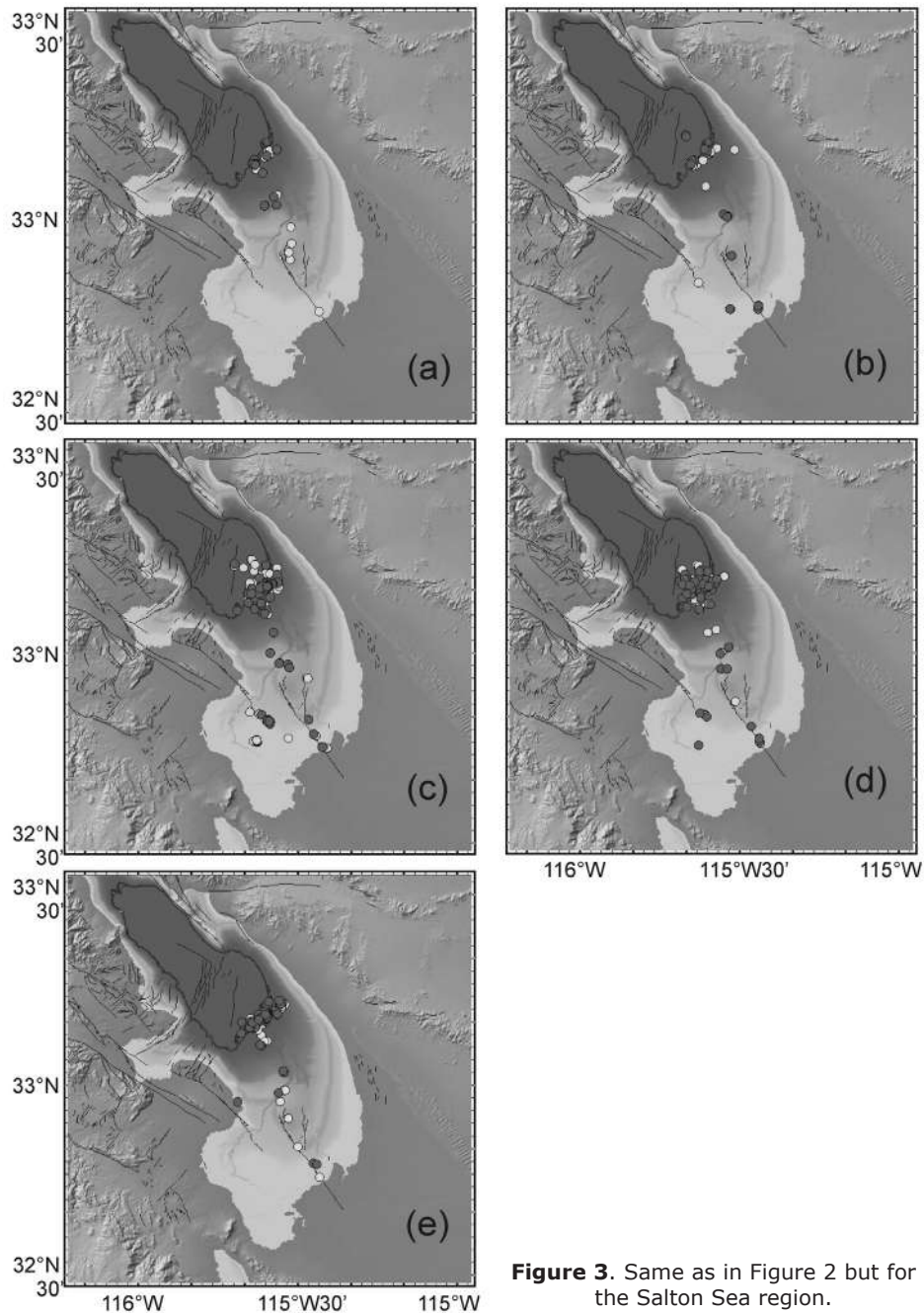


**Figure 3.** Same as in Figure 2 but for the Salton Sea region.

#### *The Denali fault Mw7.9 earthquake*

Remotely triggered seismicity following this earthquake has been extensively studied (Eberhart-Phillips *et al.*, 2003; Gomberg *et al.*, 2004; Pankow *et al.*, 2004; Prejean *et al.*, 2004; Hough, 2007; Jiang *et al.*, 2010; Peng *et al.*, 2011). The CGF is approximately 3700 km south east of the Denali fault epicenter and in general the Coso region does not show a significant increase in number of events until 26 days after the Denali earthquake (Figure

4, top). Aiken and Peng (2014) found events that triggered by the Denali earthquake by analyzing waveforms from a local station. They also found that most micro-earthquakes triggered were not detected by earthquake catalogs like ANSS because the low magnitude of these events ( $M < 2$ ). We detected only two events in the alternative catalog for Southern California (Figure 4) on 3 November 2002, the origin date of the Denali earthquake. The peak dynamic stress estimated by Prejean *et al.* (2004) from Love waves is  $\sim 0.01$  MPa

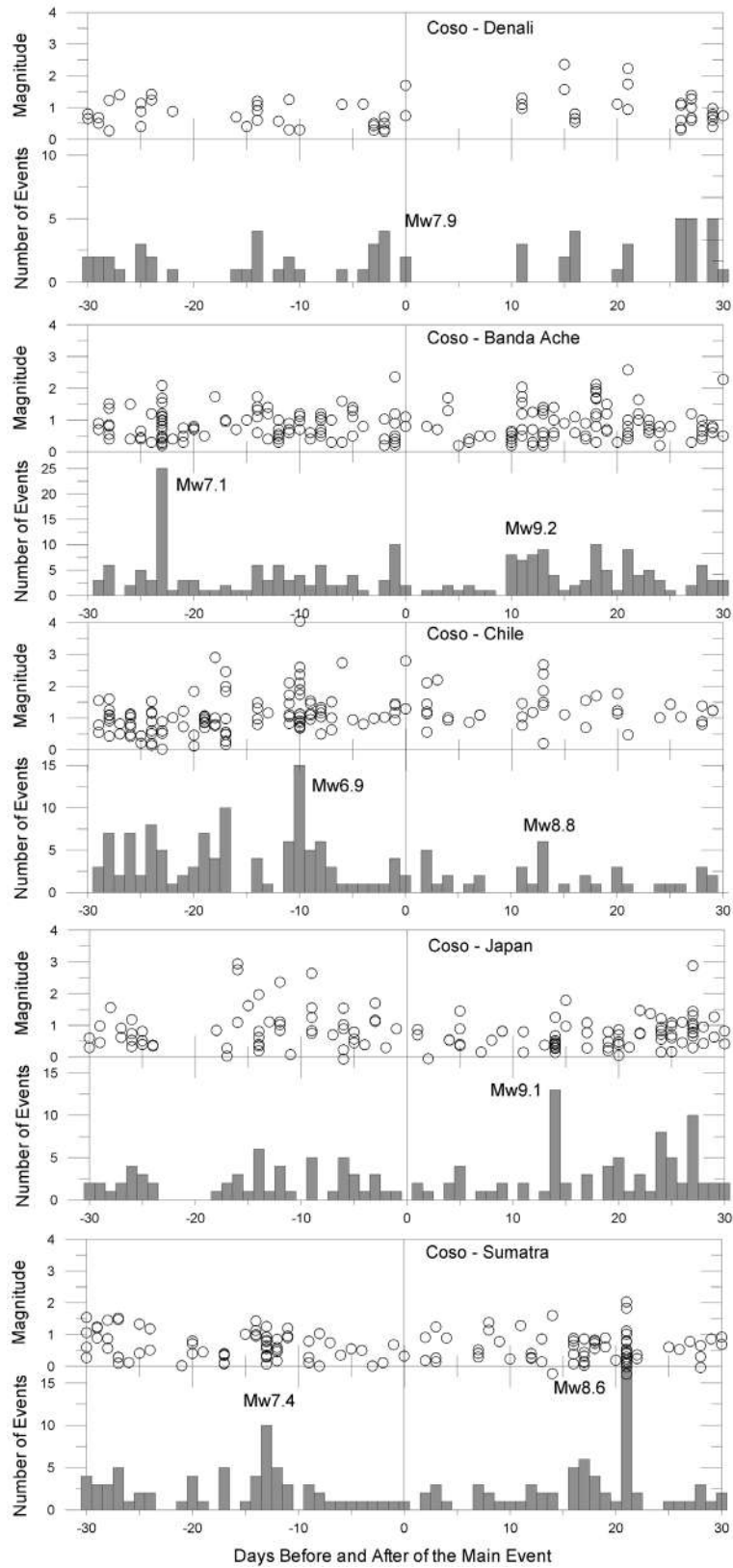


**Figure 4.** Number of events within a 30-day period before and after the remote big earthquakes in the Coso region and magnitudes of the triggered event. The numbers close to the peaks indicate the magnitude of the teleseism associated to the seismicity increase.

and  $\sim 0.03$  MPa from Rayleigh wave arrivals, and the magnitude of the largest triggered earthquake was  $M=2.3$ . They also observed that the seismicity rate in Coso did not change significantly, based on the beta statistic on the SCSN catalog.

In the Salton Sea region (Figure 5, top) the seismicity increased significantly the same day of the 2002 Denali earthquake, indicating instantaneous triggering during the passage of the surface waves. The largest event triggered has a magnitude  $M=3.25$  and smaller events occurred 14 days after with magnitudes between 1.4 and 2.2.

#### *The Banda Ache, Sumatra-Andaman Mw9.2 earthquake*

Dynamic triggering following this mega-earthquake has been studied by West *et al.* (2005) and Velasco *et al.* (2008). The local earthquakes at Mount Wrangell, Alaska occurred at depths of 2 km or less with magnitudes up to 1.9. Rayleigh waves produced vertical trough-to-peak ground motion displacements of 1.5 cm and generated stresses that reached 25 kilopascals.

The seismicity increased in the Coso and Salton Sea regions 9 days after the mega-earthquake. It is notable in Figures 4 (second row) the seismicity peak 24 days before the Mw9.2 event. We searched in the International Seismological Centre (ISC) catalog for large teleseismic events that could correlate with that seismicity peak and found a M7.1 earthquake that occurred in Papua at a depth of 10 km, on November 11, 2004, 21 days before the seismicity peak in the Coso region. In the Salton Sea region the seismicity also increased before the Mw9.2 Banda Ache, Sumatra earthquake (21 days before) and 24 days after the M7.1 Papua earthquake.

#### *The Central Chile Mw8.8 earthquake*

This event triggered seismicity in both regions 13-14 days after this mega-earthquake (Figures 4 and 5, third row). There were also increases in seismicity 10 and 5 days before the Chile earthquake in Coso and Salton Sea, respectively. That seismicity peak at the Salton Sea could have been induced by a M6.9 teleseismic earthquake located in the China-Russia-North Korea border at a depth of 25 km, on February 18, 2010. The seismicity peak in the Coso area may be related to the regional seismic activity. Remote triggered seismicity in the Coso Range following the 2010 Central

Chile  $M_w$ 8.8 earthquake has been studied in detail by Peng *et al.* (2010). They observed that the largest earthquake triggered ( $M_L$ 3.5) occurred during the passage of the Love-wave peak amplitude. The Chile  $M_w$ 8.8 earthquake also triggered seismicity in the El Mayor-Cucapah fault, Baja California region, Mexico, where the seismicity increased 10-20 days after this earthquake (Castro *et al.*, 2015).

#### *The 2011 Tohoku-Oki, Japan Mw9.1 earthquake*

The  $M_w$ 9.1 Japan earthquake generated large surface waves that impacted local seismicity thousands of kilometers away from the source region. Gonzalez-Huizar *et al.* (2012) identified several regions in the United States, Russia, China, Ecuador and Mexico where seismicity was triggered during and after the passage of the surface waves.

The 2011 Tohoku-Oki mega-earthquake presumably induced delayed seismicity 14 and 17 days after the origin time in the Coso and Salton Sea regions, respectively (Figures 4 and 5, fourth row). In the Salton Sea area there are also seismicity peaks the same day of the Japan mega-event and 5 days before, suggesting that instantaneous triggering also occurred in this region. The seismicity peak observed 5 days before may be related to the M6.5 South Sandwich Islands earthquake that occurred on March 6, 2011, the same day of the seismicity peak in the Salton Sea region.

#### *The 2012 Offshore Northern Sumatra Mw8.6 earthquake*

The Indian Ocean  $M_w$ 8.6 earthquake is the largest strike-slip event ever recorded (Pollitz *et al.*, 2012) and caused strong shaking in Indonesia, Japan and in the Gulf of California, Mexico. Several  $M>5.5$  events were delayed triggered worldwide, unlike those in previous remote-triggering cases. Aiken and Peng (2014) found that this earthquake did not trigger instantaneously microearthquakes at Coso during the arrival of surface waves.

Within the 30-day period after the 2012 Sumatra earthquake the seismicity increased on days 16 and 6 in the Coso and Salton Sea regions, respectively (Figure 4 and 5, fifth row). There is a prominent peak 12 and 19 days before this remote event in the Coso and Salton Sea, respectively, that could be related to the M7.4 Oaxaca, Mexico, earthquake of March 20, 2012.

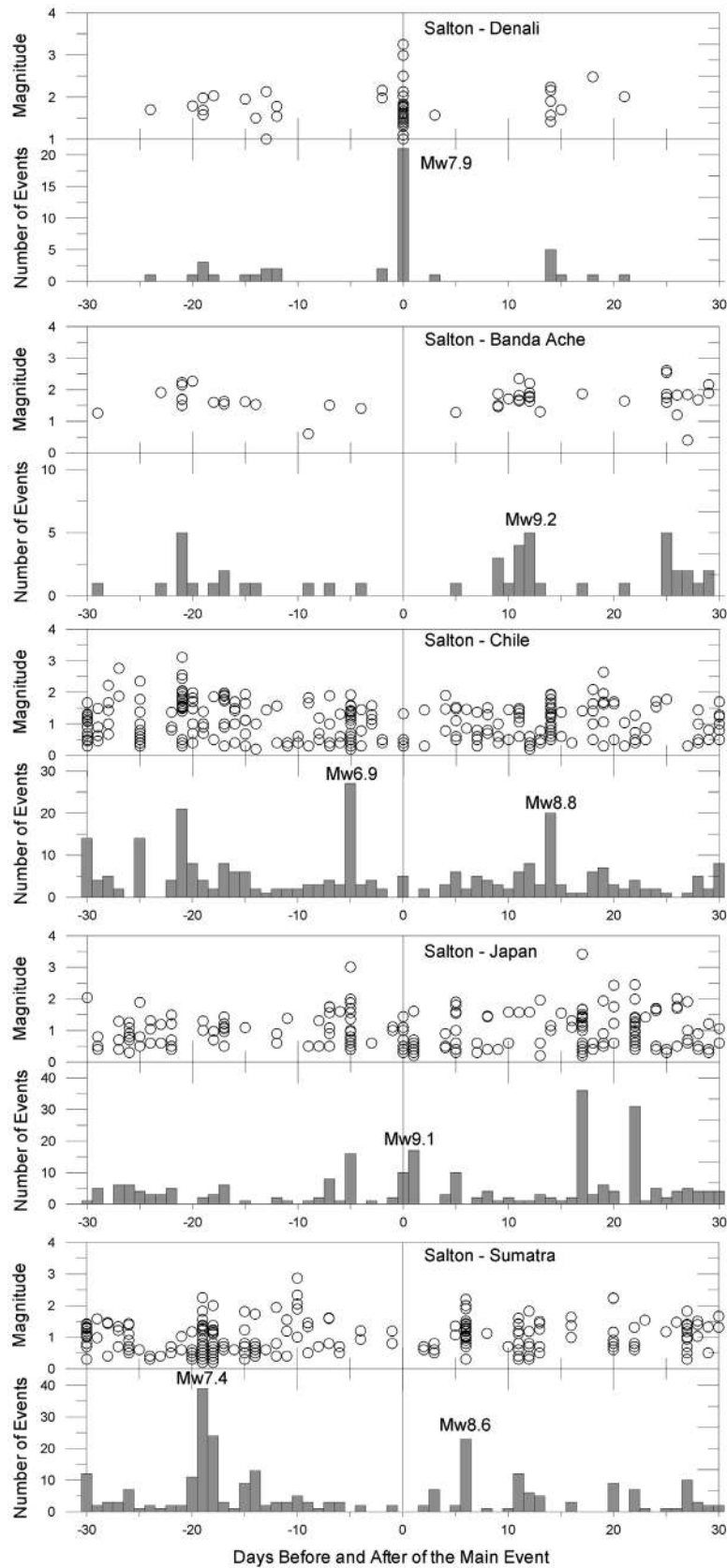


**Figure 5.** Same as in figure 4 but for the Salton Sea region.

## Results

We analyzed longer seismicity time intervals to have a better perspective on the possible influence of other large remote earthquakes on the variability of seismicity rates observed in the Salton Sea region. In Figure 6 we show the number of events per day for a 6-month period before and after the 2002 Denali  $M_w$ 7.9 and the 2004 Banda Ache  $M_w$ 9.2 earthquakes. We focus on these two events because the first one shows a clear instantaneous triggering signal in the Salton Sea region and the second is the largest of the five mega-earthquakes analyzed. The vertical lines in Figure 6 indicate the day when a big ( $M > 7.0$ ) and remote earthquake occurred worldwide. During 2002 there were 12 big teleseismic events and 17 during 2004, and the seismicity in the Salton Sea region varied from 426 events in 2002 to 407 local events in 2004. In 2002 there was a seismicity peak on day 295 that cannot be associated to any  $M > 7$  remote event but there was a  $M$ 6.6 earthquake at 19 km depth in Unimak Island region, Alaska, on February 19, 2003 that could be related to that seismicity peak. Similarly, the seismicity peak on day 219 for the 2004 Banda Ache 6-month window (Figure 6, bottom) can be related to the  $M$ 6.8 central Mid-Atlantic Ridge earthquake that occurred on January 12, 2005.

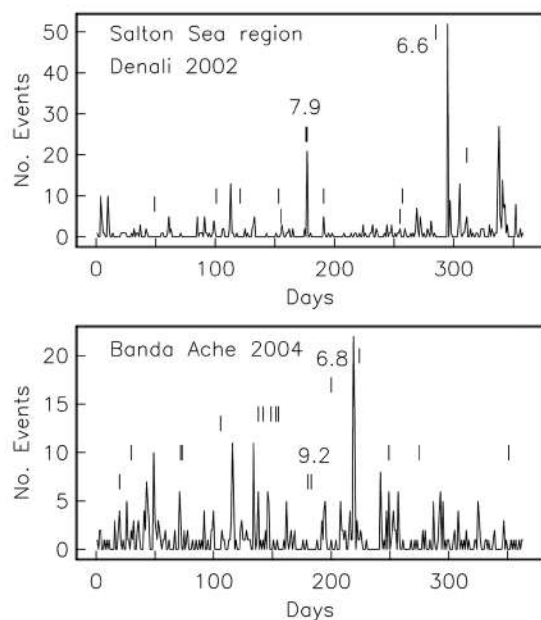


**Figure 6.** Number of events versus time in days for a 6-month period before and after the 2002 Denali fault ( $M$ 7.9) earthquake (top frame) and for the 2004 Banda Ache, Sumatra ( $M_w$ 9.2) earthquake (bottom frame). The vertical lines indicate the time of occurrence of big teleseismic ( $M > 7.0$ ) earthquakes.

The change in seismicity rate was quantified after the five mega-earthquakes by calculating the cumulative number of events in 60-day periods (Figure 7). The origin of the horizontal axis is the day of occurrence of the corresponding mega-event. The event rate variations seem to be randomly distributed before and after time zero. This observation suggests that different processes may be responsible for a swarm in geothermal fields. The  $\beta$ -statistics for the 30-day period was calculated after the five remote earthquakes for the Coso and Salton Sea regions, and for the total reference seismicity period of six months and 34 years (Table 1). The alternative Southern California catalog (Hauksson *et al.*, 2012; Lin *et al.*, 2007) was used for this calculation. The absolute values of  $\beta$  determined with equation (1) for the six month period are displayed in the lower right corner of each frame of Figure 7. In the Salton Sea region there is a clear change of seismicity rate on day zero, when the 2002 Denali fault earthquake occurred; 11 days after the 2004 Banda Ache event; 14 days after the 2010 Chile earthquake; 17 days after the 2011 Japan mega-quake; and 6 days after the 2012 Northern Sumatra earthquake.

As shown in Figures 4 and 5 most earthquakes had magnitudes below 2.0. Trugman *et al.* (2016) found that the minimum magnitude of completeness of the catalog increases during active earthquake sequences and swarms. Nevertheless,  $\beta$  was calculated using only events with magnitude above the conservative estimates of  $M_c$  obtained by Trugman *et al.* (2016), namely  $M_c = 1.5$  for Coso and  $M_c = 2.0$  for Salton Sea. Table 1 lists the present estimates of  $\beta$  for both regions for a 30-day period after the 5 teleseisms analyzed for the total reference periods of 60 days (30 days before and 30 days after the mega-earthquakes) and for a reference period of 34 years (the total period of the catalog). For the 60-day reference, in Salton Sea the change of seismicity rate is significant only after the Denali ( $M_w$ 7.9) and the Chile ( $M_w$ 8.8) earthquakes. For the Coso region the change is also significant after those events and after the Japan ( $M_w$ 9.1) earthquake. For a total reference period of 34 years, the change of seismicity rate is significant after all the events in the Salton Sea region (Table 1). For the Coso region the change was not significant only for the Sumatra ( $M_w$ 8.6).

The injection record of the geothermal fields (Figures 8 and 9) was plotted to verify that there were not significant changes of the injection parameters at the time when the seismicity rate-change takes place. No clear correlation

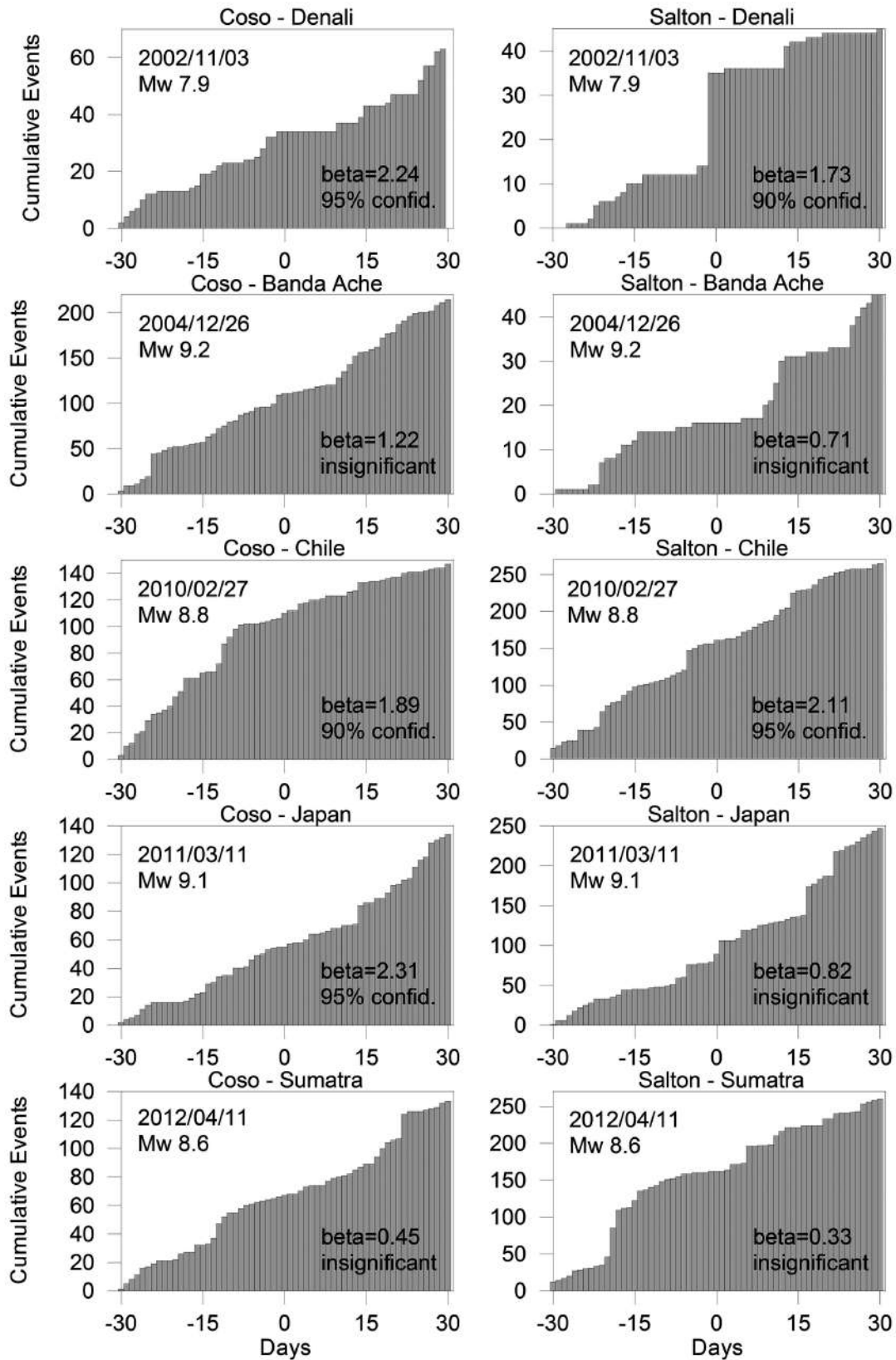


**Figure 7.** Cumulative number of events versus time for a 30-day period before and after the remote mega-earthquakes. Left column for the Coso region, right column for the Salton Sea region.

**Table 1.** Beta statistics for a 30-day period after the remote earthquake with respect to 60 days and 34 years of seismicity above  $M_c$  (the minimum magnitude of completeness for Coso and Salton Sea is 1.5 and 2.0, respectively).

EVENT	BETA (60 Days)	Confidence (%)	BETA (34 Yr)	Confidence (%)	REGION
Denali Mw7.9	1.73	90	6.1	99	Salton Sea
Banda Ache Mw9.2	0.71	Insignificant	3.6	99	
Chile Mw8.8	2.11	95	7.2	99	
Japan Mw9.1	0.82	Insignificant	11.9	99	
Sumatra Mw8.6	0.33	Insignificant	5.5	99	
Denali Mw7.9	2.24	95	3.7	99	Coso
Banda Ache Mw9.2	1.22	Insignificant	6.1	99	
Chile Mw8.8	1.89	90	2.7	99	
Japan Mw9.1	2.31	95	2.9	99	
Sumatra Mw8.6	0.45	Insignificant	1.2	Insignificant	

was observed between the seismicity rate-change and the net production (production minus injection) at neither geothermal field. Trugman *et al.* (2016) found that the seismicity rate in both fields correlates with fluid injection and withdrawal only before 1990, as shown in Figures 8 and 9.

### Discussion

Different models have been proposed to explain delayed dynamic triggering of seismicity (Brodsky and Prejean, 2005; Parsons, 2005; Hill and Prejean, 2007; Shelly *et al.*, 2011). The prolonged fault creep model (Shelly *et al.*, 2011) proposes that large remote earthquakes can induce a creep event that may trigger earthquakes secondarily, with some time delay as creep evolves. If the passage of seismic waves generated by the mega-earthquakes analyzed changed the tectonic stress near the regions studied, when the size of the mega-event increases and/or the epicentral distance decreases, the dynamic stress is expected to increase. It may be also expected that the strength of the remote earthquake will be proportional to the size of the local events triggered. In Figure 10 (upper left) the maximum magnitude ( $M_{max}$ ) of the delayed triggered earthquake swarm versus the seismic moment of the mega-earthquake divided by the epicentral distance ( $M_0/\Delta$ ) in dynes, is plotted. The solid line is the linear least-square fit of the observation points (asterisks and circles are observed data for Salton Sea and Coso, respectively) and indicates that the magnitude of the delayed triggered event increased with the size of the mega-earthquake. The resulting regression equation is:

$$\text{Log}\left(\frac{M_0}{\Delta}\right) = (19.35 \pm 0.40) + (0.44 \pm 0.17) M_{max} \quad (2)$$

Figure 10 (upper right) also shows a positive correlation between the size of the mega-event and the delay time in days ( $D_t$ ) and between  $D_t$  and the maximum magnitude of the triggered swarm (Figure 10 bottom). Based on the prolonged fault creep model (Shelly *et al.*, 2011), it is expected that the duration of the creeping event may increase when the size of the remote earthquake increases. Thus, it would be expected that the delay time of the triggered events will increase. On the other hand, longer delay times permit greater accumulation of stress on the local faults and consequently larger magnitudes will be expected. The best least-square fit of these observations are represented by the following relations:

$$\text{Log}\left(\frac{M_0}{\Delta}\right) = (19.79 \pm 0.28) + (0.44 \pm 0.02) D_t \quad (3)$$

$$M_{max} = (1.58 \pm 0.54) + (0.056 \pm 0.04) D_t \quad (4)$$

Making  $M_0/\Delta$  the independent variable, the resulting regressions give:

$$M_{max} = (-22.53 \pm 9.41) + (1.21 \pm 0.46) \text{Log}\left(\frac{M_0}{\Delta}\right) \quad (5)$$

$$D_t = (-211.8 \pm 94.6) + (11.06 \pm 4.64) \text{Log}\left(\frac{M_0}{\Delta}\right) \quad (6)$$

Equations (5) and (6) predict that for an earthquake like Japan 2011 having  $\frac{M_0}{\Delta} = 0.6435 \times 10^{21}$  dynes, the maximum magnitude expected for a local event triggered in Salton Sea or Cosco regions will be  $M_{max} = 2.6$  and will occur seven days after the remote earthquake.

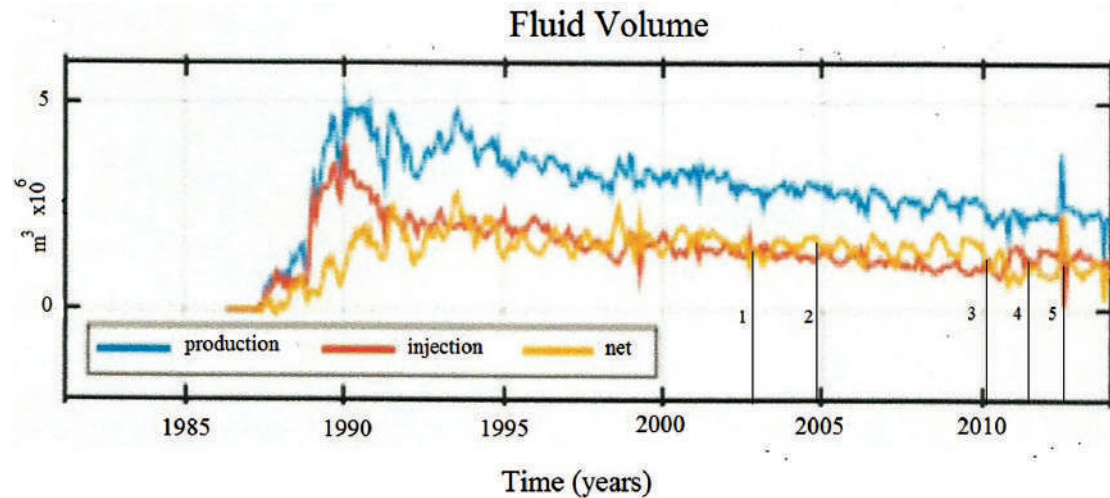


**Figure 8.** Monthly rate fluid injection (red), production (blue), and net production (yellow) (modified from Trugman *et al.*, 2016) at Coso geothermal field (data available at <http://www.conservation.ca.gov/dog/geothermal>). The vertical lines (black) indicate the date when the remote earthquakes occurred: (1) the November, 2002 Denali fault, Alaska ( $Mw7.9$ ); (2) the December, 2004 Banda Ache ( $Mw9.2$ ); (3) the February, 2010 Central Chile ( $Mw8.8$ ); (4) the March, 2011 Tohoku-Oki, Japan ( $Mw9.1$ ); (5) the April, 2012 Northern Sumatra ( $Mw8.6$ ) earthquake.

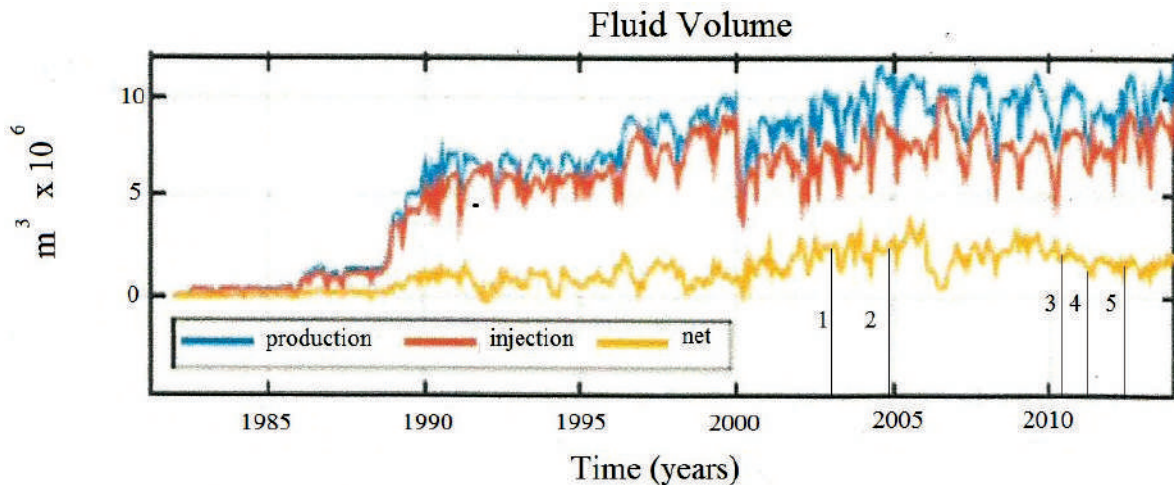


**Figure 9.** Same as in Figure 8 but for Salton Sea geothermal field.

Other regions may be able to generate bigger magnitude events. For instance, Gonzalez-Huizar *et al.* (2012) observed delayed triggering of larger magnitudes, including an  $M=5.2$ , in the southern Gulf of California following the 2011 Tohoku-Oki earthquake. Equations (5) and (6) should be used with caution because the data set used to obtain them is small and spread. However, these equations permit to quantify the trends of the observations here presented.

An alternative model to explain the delayed triggered seismicity and the spatial distribution pattern of earthquakes observed in Figures 2 and 3 is to consider that the surface waves generated by the large distant events induce the migration of pressurized pore fluids (e.g. Malagnini *et al.*, 2012). The migration of fluids can cause an increase in pore pressure and the decrease in shear strength on the fault planes, inducing earthquakes. This diffusion-like process can be modeled as a 1-D steady state source of pressure that starts when the

Rayleigh wave reach the region of interest. The solution to this 1-D diffusion process is given by Turcotte and Schubert (1982):

$$P(x,t) = (P_0 - P_1) \operatorname{erfc} \left( \frac{x}{2\sqrt{Dt}} \right) + P_1 \quad (7)$$

With the following boundary and initial conditions:

$$P(x = 0, t > 0) = P_0 = \gamma_f \rho_r g z \quad (8)$$

$$P(x > 0, t = 0) = P_1 = \rho_w g z \quad (9)$$

Where *erfc* is the complementary error function, *D* is the diffusion coefficient,  $\gamma_f = 0.8$  is the pore fluid coefficient,  $\rho_r = 2.99 \text{ gr/cm}^3$ ,  $z = 3 \text{ km}$  is the depth and  $\rho_w$  is the density of the water. Turcotte and Schubert (1982) show that the position of the pressure boundary can be estimated with the relation:

$$x_p = 2.32\sqrt{Dt} \quad (10)$$

This model was tested with the seismicity triggered by the 2011 Japan ( $M_w 9.1$ ) earthquake (fourth row of Figures 4 and 5). This earthquake was selected because it is one of the biggest and it triggered delayed and instantaneous seismicity in both Coso and Salton Sea geothermal fields. The fluid flow was assumed to start with the arrival of the Rayleigh waves generated by the Japan earthquake to the geothermal fields and that the seismicity migrates in the same direction of the pressure boundary following equation (10). The first event triggered with the Rayleigh wave arrival was used as a reference origin and relative distances were calculated. Figure 11 shows time of occurrence in days versus relative distance in km. The solid lines are the expected position of the pressure boundary for different values of the diffusion coefficient *D*. This figure illustrates that the seismicity in

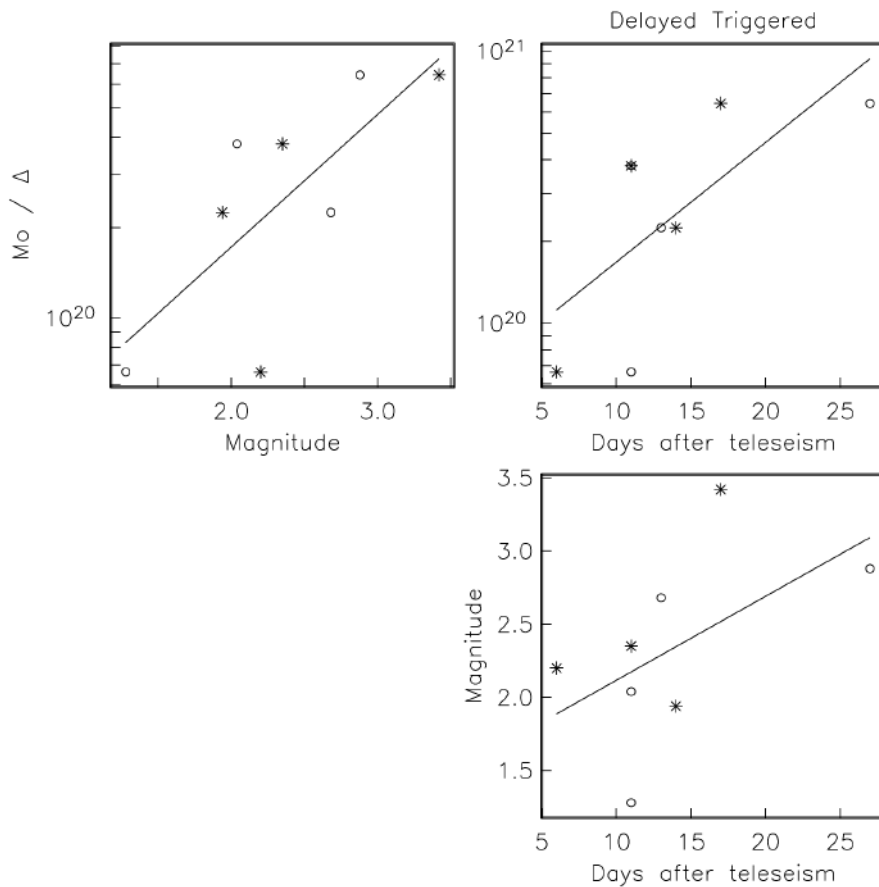


**Figure 10.** Correlation between size of remote earthquakes (seismic moment/epicentral distance) and maximum magnitude of the triggered event (upper left frame) in the Salton Sea (asterisks) and in the Coso Range (circles) regions. The upper right shows the time delay in days after the mega-earthquake. The bottom frame shows the relation between time after the mega-earthquake and the maximum magnitude of the local event triggered.

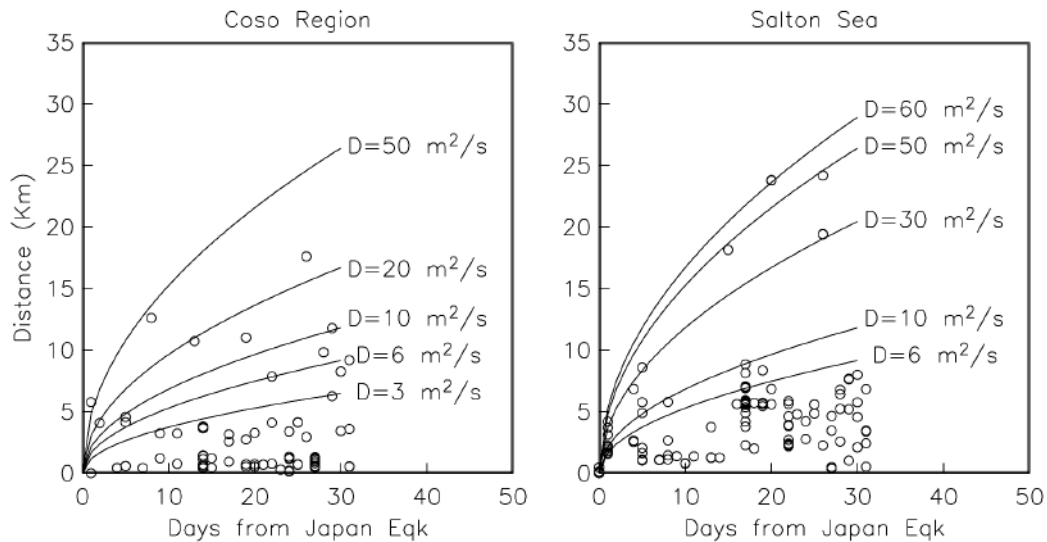


**Figure 11.** Events that occurred 30 days after the 2011 Japan ( $M_w$ 9.1) earthquake in the Coso region (left) and in the Salton Sea region (right). The distance is relative to the first event of the swarm that occurred after the Japan earthquake. The solid lines are the expected position of the pressure boundary for different values of the diffusion coefficient  $D$  (equation 10).

the 30-day window after the Japan earthquake seems to follow a diffuse pattern, as predicted by the 1-D model (equations 7 and 10). The Rayleigh waves propagate toward the SE and seismicity is expected to migrate in the same direction. In the Salton Sea region, for instance, events with larger relative distance (Figure 9 right) are located south of the geothermal field (Figure 3d).

## Conclusions

The 2011-Hauksson-Yang-Shearer alternative catalog of Southern California was used to analyze possible changes in seismicity rate in the Coso and Salton Sea, southern California, during and after five large ( $M_w > 7.8$ ) and remote earthquakes. The 2002 Denali fault ( $M_w$ 7.9) earthquake and the 2011 Tohoku-Oki ( $M_w$ 9.1) earthquake generated an increase of seismicity in the Salton Sea region the day when these remote events occurred, indicating that instantaneous triggered seismicity was likely induced by the passage of the surface waves. No instantaneous triggering was detected in the Coso region with the alternative seismicity catalog of southern California but a clear delayed triggered seismicity was observed after the  $M_w$ 7.9 Denali, the  $M_w$ 8.8 Chile and the  $M_w$ 9.1 Japan. Delayed triggered seismicity in the Salton Sea for those earthquakes was also observed.

In conclusion the observations of delayed triggering presented here are consistent with the prolonged fault creep model proposed by Shelly *et al.* (2011). The stronger the dynamic stress the bigger the creeping event induced and the longer the delay of the triggered event. Equation (4) indicates that the longer the delay time the bigger the maximum magnitude of the expected triggered earthquake. The resulting regressions (equations 5 and 6) could be useful to evaluate if remote mega-earthquakes can trigger significant size earthquakes locally, and when the triggered seismicity could occur. However, this process also depends on the earthquake cycle of the active region and those regressions should be used with caution until more data is available to verify the observed trends. The spatial-temporal distribution of the seismicity in Coso and Salton Sea geothermal fields following the 2011 Japan earthquake is also consistent with a diffusion model where migration of fluids can cause increase in pore pressure and the decrease in shear strength that induces earthquakes. This alternative model to explain the delayed triggered seismicity and the spatial distribution pattern of earthquakes observed is complex because it relies on the wave propagation characteristics of the Rayleigh waves.

## Acknowledgements

This paper was prepared while the first author (RRC) was on sabbatical year in Caltech. We thank CONACYT and Prof. Gurnis for the support provided. Antonio Mendoza helped us to prepare some maps. We used parametric data from the Caltech/USGS Southern California Seismic Network (SCSN); DOI: 10.7914/SN/CI; stored at the Southern California Earthquake Center. doi:10.7909/C3WD3xH1. We thank the two anonymous reviewers and the Editor Dr. Xyoli Pérez-Campos for their comments and suggestions.

## References

- Aiken C., Peng Z., 2014, Dynamic triggering of microearthquakes in three geothermal/volcanic regions of California. *J. Geophys. Res. Solid Earth*, 119, 6992-7009.
- Anderson J.G., Brune J.N., Lowie J.N., Zeng Y., Savage M., Yu G., Chen Q., dePolo D., 1994, Seismicity in the western Great Basin apparently triggered by the Landers, California, earthquake, 28 June 1992. *Bull. Seism. Soc. Am.*, 84, 863-891.
- Aron A., Hardebeck J.L., 2009, Seismicity rate changes along the central California coast due to stress changes from the 2003 M6.5 San Simeon and 2004 M6.0 Parkfield earthquakes. *Bull. Seism. Soc. Am.*, 99, 2280-2292.
- Barak S., Klemperer S.L., Lawrence J.F., 2015, San Andreas fault dip, Peninsular Ranges mafic lower crust and partial melt in the Salton Trough, Southern California, from ambient-noise tomography, *Geoch., Geophys., Geosystems, AGU Publications*, doi:10.1002/2015GC005970.
- Bhattacharyya J., Lees J.M., 2002, Seismicity and seismic stress in the Coso Range, Coso geothermal field, and Indian Wells Valley region, southeast-central California, *Mem. Geol. Soc. Am.*, 195, 243-257.
- Brodsky E.E., Prejean S.G., 2005, New constraints on mechanisms of remotely triggered seismicity at Long Valley Caldera. *J. Geophys. Res.*, 110, B04302, doi:10.1029/2004JB003211.
- Brodsky E.E., Lajoie L.J., 2013, Anthropogenic seismicity rates and operational parameters at the Salton Sea Geothermal Field, *Science*, 341, 543-546, doi:10.1126/science.1233554.
- Castro R.R., González-Huizar H., Zúñiga F.R., Wong V.M., Velasco A.A., 2015, Delayed dynamic triggered seismicity in northern Baja California, Mexico caused by large and remote earthquakes, *Bull. Seism. Soc. Am.*, 105, 1825-1835.
- Doran A.K., Peng Z., Meng X., Wu C., Kilb D., 2011, Dynamic triggering of earthquakes in the Salton Trough of southern California, *Seismol. Res. Lett.*, 82, 2.
- Doser D.I., Kanamori H., 1986, Depth of seismicity in the Imperial Valley region (1977-1983) and its relationship to heat flow, crustal structure and the October 15, 1979, earthquake, *J. Geophys. Res.*, 91, 675-688.
- Eberhart-Phillips D., Haeussler P.J., Freymueller J.T., Frankel A.D., Rubin C.M., Craw P., Ratchkovski N.A., Anderson G., Carver G.A., Crone A.J., Dawson T.E., Fletcher H., Hansen R., Harp E.L., Harris R.A., Hill D.P., Hreinsdóttir S., Jibson R.W., Jones L.M., Kayen R., Keefer D.K., Larsen C.F., Moran S.C., Personius S.F., Plafker G., Sherrod B., Sieh K., Sitar N., Wallace W.K., 2003, The 2002 Denali fault earthquake, Alaska: A large magnitude, slip-partitioned event, *Science*, 300, 1113-1118, doi:10.1126/science.1082703.
- Elders W.A., Rex R.W., Robinson P.T., Biehler S., Meidav T., 1972, Crustal spreading in southern California: The Imperial Valley and the Gulf of California formed by the rifting apart of a continental plate, *Science*, 178, 15-24.
- Feng Q., Lees J.M., 1998, Microseismicity, stress and fracture in the Coso Geothermal Field, California, *Tectonophysics*, 289, 221-238, doi:10.1016/S0040-1951(97)00317-X.
- Fuis G.S., Mooney W.D., Healy J.H., McMechan G.A., Lutter W.J., 1984, A seismic refraction survey of the Imperial Valley region, California, *J. Geophys. Res.*, 89, 1165-1189.
- Gomberg J., Bodin P., 1994, Triggering of the Ms=5.4 Little Skull Mountain, Nevada, earthquake with dynamic strains, *Bull. Seism. Soc. Am.*, 84, 844-853.
- Gomberg J., Bodin P., Larson K., Dragert H., 2004, Earthquake nucleation by transient deformations caused by the M=7.9 Denali, Alaska, earthquake, *Nature*, 427, 621-624, doi:10.1038/nature02335.

- Gonzalez-Huizar, Velasco, 2011, Dynamic triggering: Stress modeling and a case study, *J. Geophys. Res.*, 116, B02304, doi:10.1029/2009JB007000.
- Gonzalez-Huizar, H., A.A. Velasco, Z. Peng, and R. Castro (2012). Remote triggered seismicity caused by the 2011, M9.0 Tohoku-Oki, Japan earthquake, *Geophys. Res. Lett.*, 39, L10302, doi:10.1029/2012GL051015,2012.
- Hauksson, E., K. Hutton, H. Kanamori, L. Jones, J. Mori, S. Hough, and G. Roquemore (1995). Preliminary report on the 1995 Ridgecrest earthquake sequence in eastern California, *Seismol. Res. Lett.*, 66, 54-60.
- Hauksson, E., and J. Unruh (2007). Regional tectonics of the Coso geothermal area along the intracontinental plate boundary in central eastern California: Three-dimensional Vp and Vp/Vs models, spatial-temporal seismicity patterns, and seismogenic deformation. *J. Geophys. Res.*, 112, B06309, doi:10.1029/2006JB004721.
- Hauksson, E. (2011). Crustal geophysics and seismicity in southern California, *Geophys. J. Int.*, 186, 82-98.
- Hauksson, E., W. Yang, and P.M. Shearer (2012). Wave form relocated earthquake catalog for Southern California (1981 to 2011). *Bull. Seism. Soc. Am.*, 102, 2239-2244.
- Hill, D.P., P.A. Reasenber, A. Michael, W.J., Arabaz, G. Beroza, D. Brumbough, J.N., Brune, R. Castro., S. Davis, D. de Polo, W.L. Ellsworth, J. Gomberg, S. Harmson, L. House, S.M. Jackson, M.J.S. Johnston, L. Jones, R. Keller, S. Malone, L. Munguía, S. Nava, J.C. Pechmann, A. Sanford, R.W. Simpson, R.B. Smith, M. Stark, M. Stickney, A. Vidal, S. Walter, V. Wong, J. Zollweg (1993). Seismicity remotely triggered by the Magnitude 7.3 Landers, California, Earthquake, *Science*, 260, 1617-1623.
- Hill, D. P., and S. G. Prejean (2007). Dynamic triggering, in *Treatise on Geophysics*, 257–292, ed. Schubert, G., Vol. 4: Earthquake Seismology, ed. Kanamori, H., Elsevier, Amsterdam.
- Hill, D.P. (2008). Dynamic stresses, coulomb failure, and remote triggering, *Bull. Seism. Soc. Am.*, 98, 66-92.
- Hough, S.E., and H. Kanamori (2002). Source properties of earthquakes near Salton Sea triggered by the 16 October 1999 M7.1 Hector Mine, California, earthquake, *Bull. Seismol. Soc. Am.*, 92, 1281-1289.
- Hough, S.E. (2007). Remotely triggered earthquakes following moderate main shocks, *Spec. Pap. Geol. Soc. Am.*, 425, 73-86.
- Hubbert, M.K., and W.W. Rubey (1959). Role of fluid pressure in mechanics of overthrust faulting, *Geol. Soc. Am. Bull.*, 70, 115-166.
- International Seismological Centre, On-line Bulletin, <http://www.isc.ac.uk>, Internatl. Seis. Cent. Thatcham, United Kingdom, 2016.
- Jiang, T., Z. Peng, W. Wang, and Q.-F. Chen (2010). Remotely triggered seismicity in continental China by the 2008 Mw7.9 Wenchuan earthquake, *Bull. Seismol. Soc. Am.*, 100, 2574-2589, doi:10.1785/0120090286.
- Lachenbruch, A.H.A., J.H. Sass, S.P. Galanis, and S. Galanis Jr. (1985). Heat flow in southernmost California and the origin of the Salton Trough, *J. Geophys. Res.*, 90, 6709-6736.
- Lin, G., P.M. Shearer, and E. Hauksson (2007). Applying a three-dimensional velocity model, wave form cross correlation, and cluster analysis to locate southern California seismicity from 1981 to 2005. *J. Geophys. Res.*, 112, B12309, doi:10.1029/2007JB004986.
- Linde, A.T., and I.S. Sacks (1998). Triggering of volcanic eruptions, *Nature*, 395, 888-890.
- Malagnini, L., F.P. Lucente, P. De Gori, A. Akinci, and I. Munafo (2012). Control of pore fluid pressure diffusion on fault failure mode: Insights from the 2009 L'Aquila seismic sequence. *J. Geophys. Res.*, 117, B05302, DOI:10.1029/2011JB008911.
- Matthews, M.V., and P.A. Reasenber (1988). Statistical methods for investigating quiescence and other temporal seismicity patterns. *Pure Appl. Geophys.*, 126, 357-372.
- Monastero, F.C., A.M., Katzenstein, J.S., Miller, J.R., Unruh, M.C., Adams, K., Richards-Dinger (2005). The Coso geothermal field: A nascent metamorphic core complex. *GSA Bulletin*, 117, 1534-1553, DOI:10.1130/B25600.1

- Muffler, L.J., and D.E. White (1969). Active metamorphism of upper Cenozoic sediments in the Salton Sea Geothermal Field and the Salton Trough, Southeastern California, *Geol. Soc. Am. Bull.*, 80, 157-182.
- Pankow K.L., Arabasz W.J., Pechmann J.C., Nava S.J., 2004, Triggered seismicity in Utah from the November 3, 2002, Denali fault earthquake, *Bull. Seismol. Soc. Am.*, 94, S332-S347.
- Parsons T., 2005, A hypothesis for delayed dynamic earthquake triggering, *Geophys. Res. Lett.*, 32, L04302, doi: 10.1029/2004GL021811
- Peng Z., Gomberg J., 2010, An integrated perspective of the continuum between earthquakes and slow-slip phenomena, *Nat. Geosci.*, 3, 599-607, doi:10.1038/ngeo940.
- Peng Z., Hill D.P., Shelly D.R., Aiken C., 2010, Remotely triggered microearthquakes and tremor in central California following the 2010 Mw 8.8 Chile earthquake. *Geophys. Res. Lett.*, 37, L24312, doi:10.1029/2010GL045462
- Peng Z., Wu C., Aiken C., 2011, Delayed triggering of microearthquakes by multiple surface waves circling the Earth. *Geophys. Res. Lett.*, 38, L04306, doi:10.1029/2010GL046373.
- Pollitz F.F., Stein R.S., Sevilgen V., Burgmann R., 2012, The 11 April 2012 east Indian Ocean earthquake triggered large aftershock worldwide, *Nature*, 490, doi:10.1038/nature11504
- Prejean S.G., Hill D.P., Brodsky E.E., Hough S.E., Johnson M.J.S., Malone S.D., Oppenheimer D.H., Pitt A.M., Richards-Dinger K.B., 2004, Remotely triggered seismicity on the United States west coast following the M 7.9 Denali fault earthquake, *Bull. Seismol. Soc. Am.*, 94, S348-S359.
- Ryan W.B.F., Carbotte S.M., Coplan J.O., O'Hara S., Melkonian A., Arko R., Weissel R.A., Ferrini V., Goodwillie A., Nitsche F., Bonczkowski J., Zemsky R., 2009, Global Multi-Resolution Topography synthesis, *Geochem. Geophys. Geosys.*, 10, Q03014, DOI:10.1029/2008GC002332.
- Schmitt A.K., Martin A., Stockli D.F., Farley K.A., Lovera O.M., 2013, (U-Th)/He zircon and archaeological ages for a late prehistoric eruption in the Salton Trough (California, USA), *Geology*, 41, 7-10.
- Shelly D.R., Peng Z., Hill D., Aiken C., 2011, Triggered creep as a possible mechanism for delayed dynamic triggering of tremor and earthquakes, *Nature Geosci.*, 4, 384-388.
- Stock J.M., Hodges K.V., 1989, Pre-Pliocene extension around the Gulf of California and the transfer of Baja California to the Pacific Plate, *Tectonics*, 8, 99-115.
- Trugman D., Shearer P.M., Borsa A.A., Fialko Y., 2016, A comparison of long-term changes in seismicity at the Geysers, Salton Sea, and Coso geothermal fields, *J. Geophys. Res. Solid Earth*, 121, 225-247, doi:10.1002/2015JB012510.
- Turcotte D.L., Schubert G., 1982, *Geodynamics: Applications of continuum Physics to geological problems*, 450 pp., John Wiley, New York.
- West M., Sanchez J.J., McNutt S.R., 2005, Periodically triggered seismicity at Mount Wrangell, Alaska, after the Sumatra earthquake, *Science*, 308, 1144-1146, doi:10.1126/science.1112462.
- Velasco A.A., Hernandez S., Parsons T., Parkow K., 2008, Global ubiquity of dynamic earthquake triggering, *Nat. Geosci.*, 1, 375-379, doi:10.1038/ngeo204.

## Paleomagnetism and Aeromagnetic Survey From Tancitaro Volcano (Central Mexico) - Paleo-Secular Variation at Low Latitudes During the Past 1 Ma

Rafael García-Ruiz, Avto Goguitchaichvili\*, Hector-López Loera, Miguel Cervantes-Solano, Jaime Urrutia-Fucugauchi, Juan Morales-Contreras, Rafael Maciel-Peña and José Rosas-Elguera

Received: October 17, 2016; accepted: April 28, 2017; published on line: July 01, 2017

### Resumen

El volcán Tancitaro (TV) forma parte del campo volcánico monogenético Michoacán-Guanajuato (MGVF) en el sector centro-oeste del Eje Volcánico Trans Mexicano (TMVB). Los resultados de un estudio paleo magnético de flujos de lava del volcán Tancitaro fechados radiométricamente, se utilizaron para investigar la variación paleo secular (PSV) y el campo promedio temporal (TAF) para latitudes bajas. El rango de fechado Ar-Ar fue de 70 a 960 años considerando los Chrones de polarización de Brunhes y Matuyama. Todas las muestras arrojaron una polaridad de magnetización normal bien definida. Dos flujos se correlacionaron con la polaridad del Evento Jaramillo, lo cual provee un marcador útil para la actividad volcánica en el MGVF. Para los análisis del PSV y TAF las paleo direcciones se combinaron con resultados anteriores de alta precisión. El estudio aeromagnético alrededor del volcán Tancitaro se caracterizó por una serie de anomalías tanto positivas como negativas. El Volcán Tancitaro presenta una gran anomalía positiva que sugiere la presencia de una gran fuente subterránea. El análisis espectral de este campo anómalo da una estimación promedio hacia la parte alta de los cuerpos que la originan entre 2-3 km.

Palabras clave: Variación paleo secular; Dipolo axial geomagnético; excursiones al Jaramillo; Volcán Tancitaro; Aeromagnetismo.

### Abstract

The Tancitaro volcano (TV) is part of the Michoacan-Guanajuato monogenetic volcanic field (MGVF) in the central-western sector of the Trans-Mexican Volcanic Belt (TMVB). Results of a paleomagnetic study of radiometrically dated lava flows from Tancitaro volcano were used to investigate the paleosecular variation (PSV) and time averaged field (TAF) at low latitudes. Ar-Ar dates range from ~70 to 960 kyr spanning the Brunhes and Matuyama polarity chrons. All samples yielded well defined normal polarity magnetization. Two flows are correlated to the Jaramillo polarity event, which provide a useful marker for the volcanic activity in the MGVF. For the PSV and TAF analysis, paleodirections were combined with previously reported high standard results. The aeromagnetic survey around the Tancitaro volcano was characterized by a trend of regional anomalies over the volcanic structures. The residual field showed several positive and negative anomalies. The Tancitaro volcano is marked by a broad positive anomaly suggesting the presence of a large underground source. Spectral analysis of this anomaly field gives an average estimate to the top of the source bodies between 2-3km.

Key words: Paleosecular variation, Geomagnetic Axial Dipole, Jaramillo excursions, Tancitaro volcano, Aeromagnetism.

R. García-Ruiz  
A. Goguitchaichvili\*  
J. Urrutia-Fucugauchi  
J. Morales-Contreras  
Instituto de Geofísica-Unidad Michoacán  
Universidad Nacional Autónoma de México  
Campus Morelia, Morelia Michoacán  
Antigua Carretera a Pátzcuaro 8701, 58059, México  
\*Corresponding author: [avto@geofisica.unam.mx](mailto:avto@geofisica.unam.mx)

H. López-Loera  
División de Geociencias Aplicadas  
IPICYT, San Luis Potosí, México.

M. Cervantes-Solano  
Escuela Nacional de Estudios Superiores  
Unidad Morelia, Antigua Carretera a Pátzcuaro 8701  
Morelia Michoacán 58190, México.

R. Maciel-Peña  
Instituto Tecnológico Superior de Tacámbaro División  
de Investigación y Estudios Superiores  
Av. Tecnológico 201  
Tacámbaro Michoacán 61650 México

J. Rosas-Elguera  
Laboratorio Interinstitucional de Magnetismo Natural  
Sede Guadalajara  
Universidad de Guadalajara, México

## Introduction

Study of radiometrically dated lava flows permits understanding the behavior of the Earth magnetic field (EMF) during the geological periods. The paleomagnetic records provide valuable information about the directions and intensity stored in each independent cooling unit. Sediments may provide quite continuous records of magnetic field variation, while lavas, due to the sporadic character of volcanic eruptions, yield rather discontinuous records of geomagnetic field fluctuations. On the other hand, the results obtained from lavas are generally more reliable because of nature and physical principles of the thermoremanent magnetization (TRM) acquisition (Prévot *et al.*, 1985). Many high resolution volcanic records have documented polarity transitions and intervals of constant polarity termed chrons and relatively short duration of  $10^3$ – $10^4$  year's events or excursions inside. The transitional episodes are generally defined in terms of a deviations in intervals less than  $10^3$  years of the Virtual Geomagnetic Pole (VGP) position from the Geomagnetic Axial Dipole (GAD).

The whole Trans Mexican Volcanic Belt (TMVB) represents an excellent target for high standard paleomagnetic studies since it offers more than 3000 Plio-Quaternary lava flows (mainly monogenetic volcanoes) being many of them radiometrically dated using either K-Ar or Ar-Ar systematics. The present investigation is aimed to contribute to the Time Averaged Field (TAF) study for the past *My* and improve knowledge on the paleosecular variation (PSV) at low latitudes ( $20^\circ$ ) extending the previous work of Maciel *et al.* (2009) from Tancitaro volcano and the surrounding Michoacán-Guanajuato Volcanic Field (VFMG).

Johnson *et al.* (2008) analysis of a new generation of paleomagnetic data provides new insights about the latitudinal dependence of VGP (Virtual Geomagnetic Pole) scatter showing that this relationship is much less comparing to previous studies (Tauxe and Kent, 2004). It appears that the latitude dependence of VGP angular dispersion depends critically on a dataset from the moderate latitudes about  $20^\circ$  north including numerous data from Hawaii and Central Mexico. In other hand, modeling of the aeromagnetic anomalies in the area permits to investigate the subsurface structure, and stratigraphy, in particular about distribution of magnetic sources related to magmatic bodies and volcanic structures.

## Geological setting and sampling details

Tancitaro volcano (TV) is an andesitic-dacitic stratovolcano located in the Michoacán-Guanajuato volcanic Field (MGVF). The MGVF has an extension of 40,000 km<sup>2</sup> and is part of the central portion of the TMVB. The MGVF has geographic boundaries  $18^\circ45'N$  and  $20^\circ15'N$  in latitude and  $100^\circ25'W$  and  $102^\circ45'W$  longitude; contains over 2000 small-sized monogenetic volcanoes including basaltic monogenetic cinder cones (Hasenaka and Carmichael, 1985), maars, tuff rings, lava domes and lava flows with hidden vents. Volcanic products are predominant calc-alkaline, but some alkaline and transitional rocks are present. Silica content varies from 47% to 70% for olivine basalt and basalt-andesite rocks (Hasenaka, 1994; Hasenaka *et al.*, 1994).

The TV is a highest stratovolcano in the MGVF with a height of 3840 mts (Ownby *et al.*, 2007), and has a large amount of dated flows. The activity start  $\geq 793 \pm 22$  kyr, and its last eruption was around  $237 \pm 4$  kyr, most of these events were dated by the radiometric method  $Ar^{40}/Ar^{39}$  (Ownby *et al.*, 2007; 2010). The present study sampled 8 lava flows to complement previous work made by Maciel *et al.* (2009). These lava flows (Figure 1) have been reported by Ownby *et al.* (2010) who present 39 new Ar-Ar dates that complement 26 flows with radiometric age also reported by Ownby *et al.*, (2007).

For the present study, the volcanic flows correspond to those with radiometric age, easy access, and sampled roadside of almost continuous structures of lava flows not being rotated or unaltered outcrops and not being near a geological fault which was corroborated with the geological map of the National Geological Service. The eight samples were obtained with a gasoline powered portable drill, oriented with a magnetic compass to obtain several samples along each flow  $N \geq 8$ .

The eight flows sampled cover an age range of  $\sim 70$  to 957 kyr, and complements previous work by Maciel *et al.*, 2009, that included 11 flows with an age range from 82 to 612 kyr, since the TV is an important source of unrecorded flows that could provide important paleomagnetic information with aged of a good accuracy.

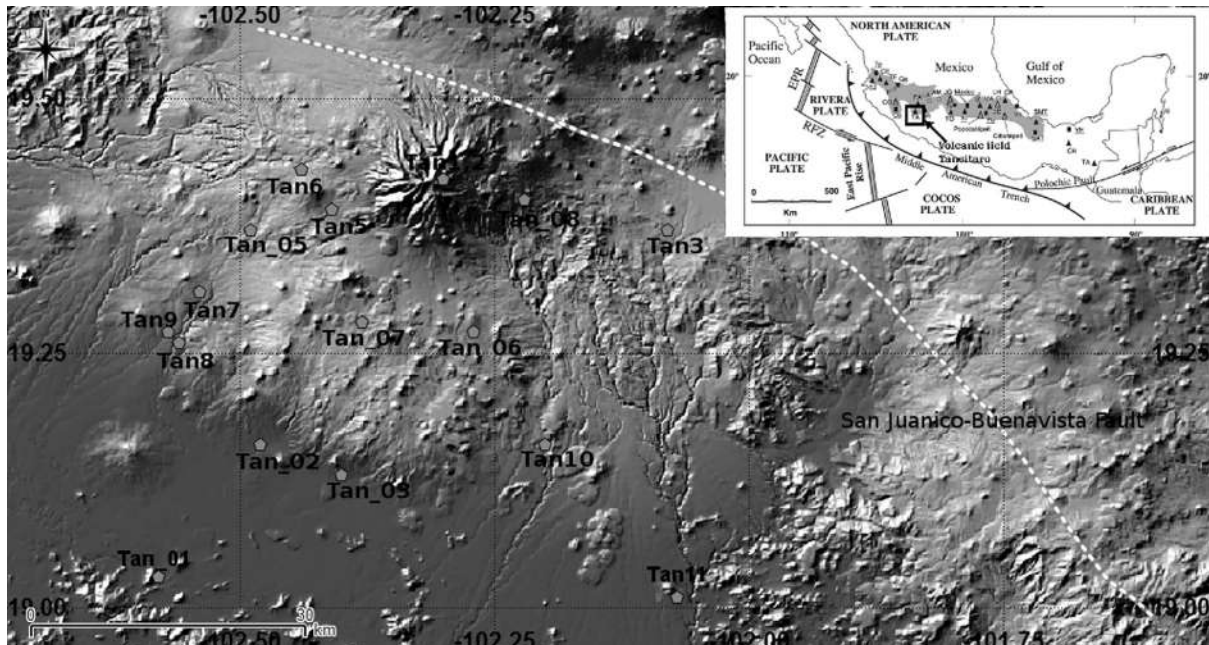


**Figure 1.** Location of the Tancitaro Volcano in the western sector of the TMVB showing the setting of sites reported in this study (Tan\_01-08) and the previously sampled flows by Maciel *et al.*, (2014) (Tan1-11).

## Magnetic Measurements and Data Analysis

### *Remanence measurements*

All specimens were demagnetized by peak alternating fields which proved to be highly efficient to isolate the characteristic, primary remanence. A Molspin AF-demagnetizer with available alternating fields from 5 to 95 *mT* was used while magnetization was measured with a JR6A (AGICO) spinner magnetometer with nominal sensitivity  $\sim 10^{-9} \text{Am}^2$ . The determination of the main magnetization components for each specimen was achieved with the method of principal component analysis (Kirschvink, 1980) and the directions were averaged by unit based on Fisher statistics (Fisher, 1953).

In most of the cases a stable, uni-vectorial characteristic remanent magnetization (ChRM) was observed (Figure 2 a) for Tan1 and Figure 2 d) for Tan7) occasionally accompanied by a negligible viscous overprint (Figure 2 b) for Tan 2 and Tan5) easily removed after the first step of demagnetization (Figure 2). Most of the specimens were completely demagnetized until 100 *mT*. The site mean directions are quite precisely determined since all  $\alpha_{95}$  are found less than  $10^\circ$ . For one out to eight studied lava flows (Tan4) not paleodirection are determined due the erratic and unstable behavior during the magnetic cleaning of specimens.

The other seven volcanic flows gave stable paleodirections, and were divided in two groups, the first group are all the directions that belong to the chron of Brunhes (5 of the 7 paleodirections) and the second group are the paleodirections that belong to the chrons of Matuyama. The directions that belong to the chron of Matuyama had the peculiarity to correspond to the same event of transition due the normal polarity and the radiometric age assigned to these flows by Ownby *et al.* (2010). The transitional event known as Jaramillo, was first recognized by Doell and Dalrymple (1966).

### *Rock magnetism*

The acquisition of thermomagnetic curves for representative samples are reported on Figure 3. Curie temperatures were estimated using the differential method of Tauxe (1998) for the analysis of the Magnetic vs Temperature curves. These analyses evidenced the low temperature phase in the heating process (red line Figure 3)  $T_c$  492°C for sample 94T002A corresponding to site Tan\_01 (Figure 3a) with two phases in the heating process (red line) that may indicates the presence of Titanomagnetite with medium Ti content. Using the method of Moskowitz (1981), it results that the highest Curie temperatures are 591°C for 94T016A corresponding to site Tan\_02 (Figure 3b), and 511°C for 94T028A corresponding to Tan\_03

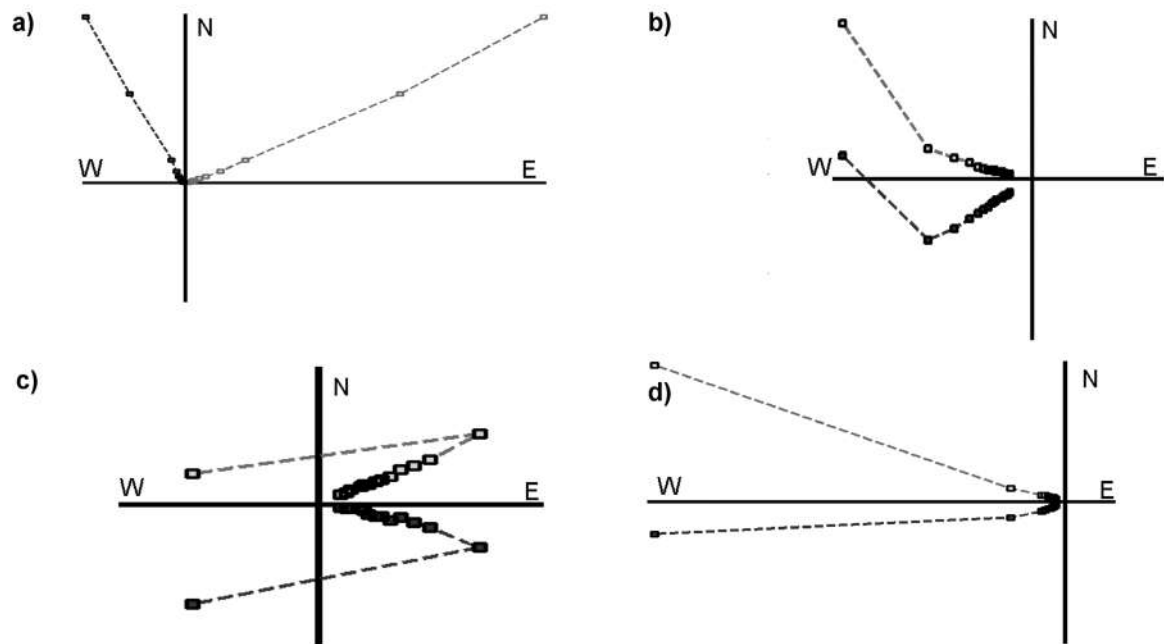


**Figure 2.** Representative examples of demagnetization experiments using peak alternative fields up to 95 mT, with the orthogonal vector plots, (Zijderveld diagrams) a) For the sample 94T004A and the site Tan1 b) Sample 94T015A and site Tan\_02, c) Sample 94T047A corresponding to Tan\_05 and d) Sample 94T060A for the site Tan\_07.

(Figure 3c). In some cases the heating and cooling curves are not perfectly reversible (Tan\_01). This may be due to the high to moderate mineralogical alteration at high temperatures occurred during the laboratory heating.

The hysteresis loops were analyzed using a RockMagAnalyzer1.0 software (Leonhard, 2006). Near to the origin, there is no evidence of wasp-waisted behavior (Tauxe, 1998), which reflect restricted coercivity ranges. When judging the ratios obtained from the hysteresis curves, samples fall in the pseudo-single domain PSD field (Figure 3). Isothermal remanence acquisition curves are sensitive to the magnetic mineralogy, concentration and grain size properties. Almost all samples are saturated at about 300 mT applied magnetic field, which indicate the presence of ferromagnetic phase with moderate coercivity as may be expected from magnetite and titanomagnetite grains (Tauxe, 1998). The lack of total symmetry on the hysteresis plots is generally attributed to the instrumental errors except for the study performed by Chandra *et al.* (2012) where the exchange bias seem to be the principal cause.

## Main Results and Discussion

All lava flows associated to the TV yielded a normal polarity magnetization. The paleodirections were divided in two groups, five of them (Tan\_01, Tan\_02, and Tan\_06-08) correspond to Brunhes Chron, and the other two (Tan\_03 and Tan\_05) belong to Matuyama Chron.

The mean paleodirection obtained from the seven flows is , , with an uncertainty  $\alpha_{95}=8.21^\circ$  and  $\kappa=13.89$ , which correspond to the pole position of  $Plat=83.06^\circ$ ,  $Plong=294.86^\circ$ ,  $A95=14.49^\circ$ . These paleodirections are combined with those obtained by Maciel *et al.* (2009) that reported 11 normal polarity directions within normal Brunhes Chron (Table 1, Figures 4 and 5). For the global mean calculation purpose we selected sites with  $N > 4$  samples per site and  $\alpha_{95} \leq 10^\circ$ . Moreover, transitional polarity data are rejected as common in studies of paleosecular variation (PSV) and time average field (TAF) for an age less than 5 Myr (Johnson *et al.*, 2008, Ruiz-Martínez *et al.*, 2010) to obtain a mean calculation.

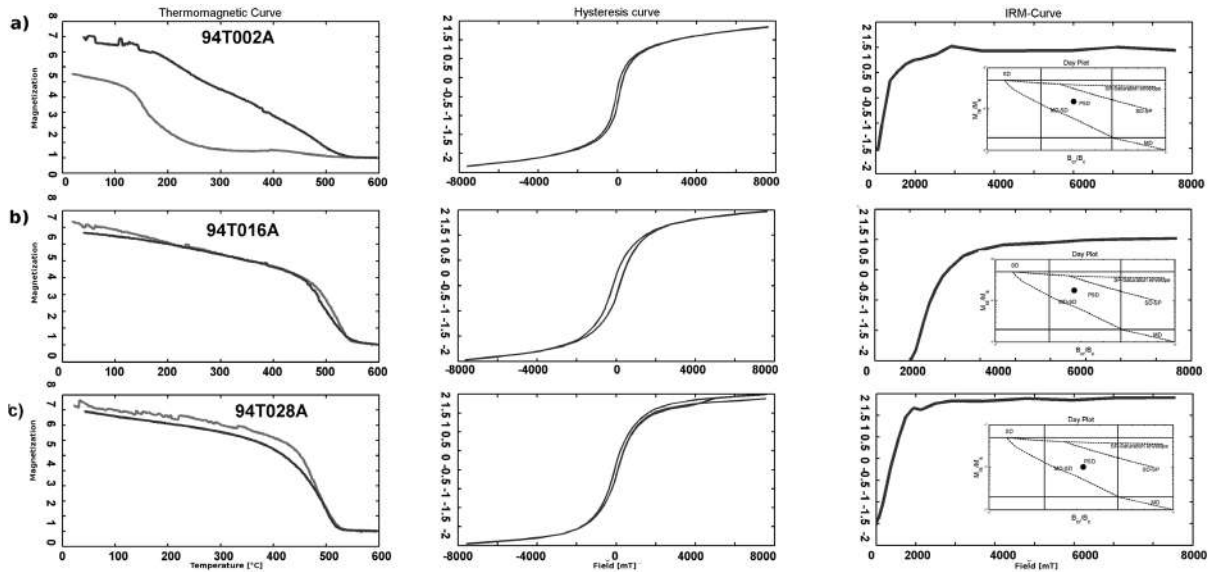


**Figure 3.** A summary of rock-magnetic experiments for the most representative samples: Temperature dependence of magnetization (magnetization), the red curve represent the heating process and the blue the cooling curve. Hysteresis loops for an induced magnetic field in blue (magnetization). Isothermal remanence magnetization acquisition curves (IRM) obtained with Variable Field Translation Balance with the respective Day Plot (Dunlop, 2002), to estimate the domain state of magnetic carriers and the relation of the ratios of the hysteresis parameters for the remained samples.

**Table 1.** Summary of all the data used in this article. Site: are the label of the sampled site; Dec and Inc: are the paleodirection treated in this study; k and a95: parameters of quality within the cone of 95%; N: Is the number of samples used to obtain the paleodirection; latitude and longitude are the coordinates for each one of the sampled sites. Age: represent the age obtained by the Ar-Ar method with its respective dispersion; VGP: are the virtual geomagnetic pole for latitude and longitude; Ref: Differentiate the paleo-direction of this study (T.S) and the paleodirection obtained by Maciel *et al.* (2009).

Site	Dec(°)	Inc(°)	k	a95(°)	N	lat(°)	long(°)	Edad(Ka)	ErrorEdad	VgpLon(°)	VgpLat(°)	Ref:
TAN_04	-	-	-	-	-	19.15	102.32	51	82	-	-	T.S.
TAN_08	350.15	24.79	117.35	5.28	6.00	19.40	102.22	70.00	0.00	159.61	78.59	T.S.
Tan10	1.20	32.80	69.00	7.30	7.00	19.16	102.20	82.00	24.00	60.80	88.27	Maciel <i>et al.</i> , 2009
TAN_02	7.51	46.00	109.17	5.06	7.00	19.16	102.48	110.00	33.00	321.09	79.28	T.S.
Tan11	349.30	43.60	198.00	4.30	7.00	19.01	102.07	163.00	37.00	227.09	78.19	Maciel <i>et al.</i> , 2009
Tan1	7.80	23.80	56.00	16.50	3.00	19.42	102.30	209.00	41.00	54.12	79.76	Maciel <i>et al.</i> , 2009
Tan2	353.50	43.50	199.00	3.90	8.00	19.42	102.30	209.00	41.00	238.28	81.54	Maciel <i>et al.</i> , 2009
Tan6	17.90	58.60	41.00	9.60	7.00	19.43	102.44	256.00	18.00	316.43	64.83	Maciel <i>et al.</i> , 2009
Tan5	348.50	41.20	-	-	2.00	19.39	102.41	269.00	22.00	-	-	Maciel <i>et al.</i> , 2009
Tan4	-	-	-	-	-	19.37	102.37	339.00	23.00	-	-	Maciel <i>et al.</i> , 2009
TAN_01	354.14	31.18	92.10	5.16	8.00	19.03	102.58	347.00	50.00	172.01	84.01	T.S.
Tan7	348.60	28.10	115.00	6.30	6.00	19.31	102.54	373.00	61.00	172.47	78.27	Maciel <i>et al.</i> , 2009
TAN_07	12.68	34.08	46.98	8.34	6.00	19.28	102.38	374.00	31.00	13.12	78.00	T.S.
Tan3	339.90	60.90	242.00	3.60	8.00	19.37	102.08	429.00	64.00	249.41	61.73	Maciel <i>et al.</i> , 2009
Tan8	2.50	27.70	359.00	2.90	8.00	19.26	102.56	612.00	41.00	74.47	84.86	Maciel <i>et al.</i> , 2009
Tan9	352.70	31.30	39.00	9.20	8.00	19.27	102.57	612.00	41.00	174.94	82.67	Maciel <i>et al.</i> , 2009
TAN_06	343.63	19.55	78.19	6.46	6.00	19.27	102.37	768.00	14.00	164.50	71.70	T.S.
TAN_03	10.40	51.21	17.35	7.94	6.00	19.13	102.40	925.00	135.00	311.04	76.30	T.S.
TAN_05	36.20	75.40	189.54	4.40	7.00	19.37	102.49	957.00	157.00	303.43	40.20	T.S.

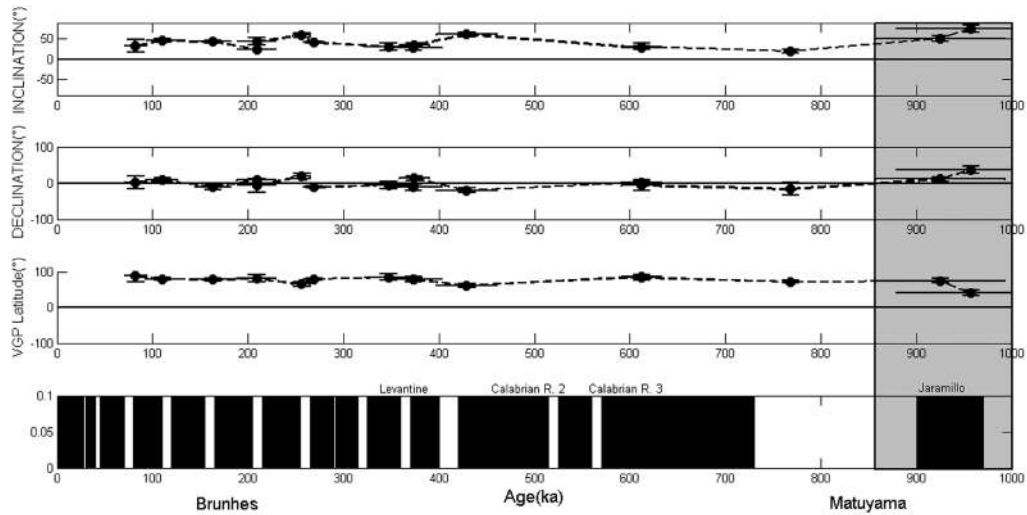


**Figure 4.** The corresponding VGP of the paleodirection with the mean VGP, and compared with the poles of reference for the last 5 Myr.

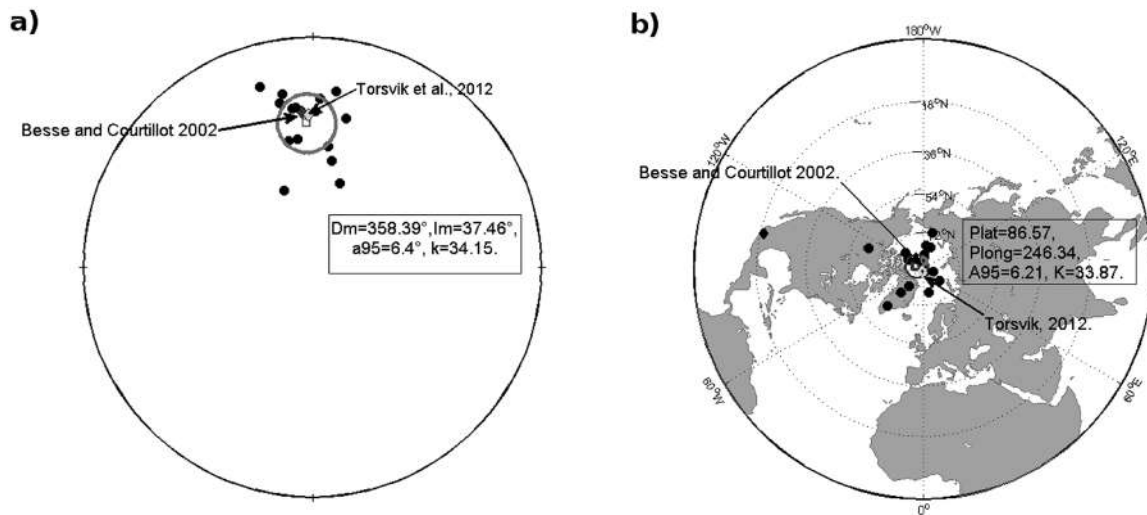


**Figure 5.** a) Projection of the paleodirection for the Tancitaro volcano with the respective mean paleodirection compared with the direction of reference for the Craton of North America provided by Besse and Courtillot (2002) and Torsvik *et al.*, 2012. b) The corresponding VGP of the paleodirection with the mean VGP, and compared with the poles of reference for the las 5 Myr.

The mean paleomagnetic direction obtained in this study is  $I = 37.46^\circ$ ,  $D = 358.39^\circ$ ,  $\alpha_{95m} = 6.4^\circ$ ,  $\kappa = 34.15$ ,  $N = 15$  and (Figure 5a). The corresponding paleomagnetic pole position is  $P_{lat} = 86.57^\circ$ ,  $P_{long} = 246.34^\circ$ ,  $A_{95m} = 6.21^\circ$  and  $K_m = 33.87$  (Figure 5b).

The mean paleodirection obtained was compared with the expected direction derived from the reference pole positions for North American Craton proposed by Besse and Courtillot (2002) and Torsvik *et al.*, (2012) yielding  $D_B = 356.1$ ,  $I_B = 33.1$  and  $D_T = 358.5$ ,  $I_T = 34.2$  respectively. The use of North

American reference poles is a common practise in almost all previous paleomagnetic surveys (García-Ruiz, *et al.*, 2016, 2017; Maciel *et al.*, 2009, 2014; Ruiz-Martínez *et al.*, 2010.) in order to avoid a kind of bias due to the neotectonic activity. For instance, the San Juanico Buenavista Fault located just beneath Tancitaro Volcano may potentially produce some minor tectonic rotations.

The mean direction agree with the expected directions within the uncertainty and this may be corroborated with the angle of deviation  $\delta_B = 4.54$  (with respect to Besse and Courtillot

(2002) reference pole) and  $\delta_T=3.34$  (with respect of Torsvik *et al.* (2012) poles). For each paleomagnetic study, it may result useful to calculate the Flattening and Rotation (Butler, 1991) parameters together with their corresponding statistics. These analysis indicate the absence of any important tectonic movement since the values are relatively low  $R_B=1.66\pm 7.22$ ,  $F_B=-4.44\pm 6.33$  (for Besse and Courtillot, 2002) and  $R_T=-0.73\pm 7.22$ ,  $F_T=-3.34\pm 6.33$  (for Torsvik, 2012). These values also agree to the study carried out by Ruiz-Martínez *et al.* (2010) at different areas within the TMVB, specially for the western and central sectors, where similar small values are obtained ( $|R| < 6^\circ$  and  $|F| < 5^\circ$ ).

Most paleomagnetic studies make the implicit assumption that when averaged over some time interval, the paleomagnetic directions are close to the geocentric axial dipole (GAD) for at least the last 5 Myr, as globally averaged paleopoles should reflect mainly the GAD field (Tauxe and Kent, 2004, Carlot and Courtillot, 1998). Under this assumption, we developed an analysis of TAF and a statistical comparison with the GAD. The mean direction of GAD was calculated for a mean latitude  $\lambda=19^\circ 16.08'$  obtaining  $D_{GAD}=0^\circ$ ,  $I_{GAD}=34.96^\circ$ , yielding a difference of  $\Delta I=2.48^\circ$  and  $\Delta D=2.32^\circ$ . These values are even lower than those found by Maciel *et al.* (2009) in previous studies and reasonably close to the GAD directions. The inclination anomaly found in this study is also compared with the value reported by Lawrence and Constable (2006), for similar latitudes  $\lambda=\pm 20^\circ$  as Hawaii, Mexico, South Pacific and Reunion. All these regions yielded statistically indistinguishable values (Figure 6).

PSV analyses are very important to estimate the paleofield location for any time known and when a multiple site sampling is collected the influence of the error is reduced. The PSV analysis was developed complementing the directions presented in this study with the directions of Maciel *et al.* (2009) and the use of angular standard deviation  $S_w = \frac{81^\circ}{\sqrt{k}}$ , to obtain  $S_w=14.09$ , the standard deviation as  $S_p^2 = (1/N-1)\sum_i \delta_i^2$  which result  $S_p=14.33$ , the root mean square of the angular deviation of VGP about the geographic axis  $S_B = \sqrt{(1/N-1)\sum_i (\delta_i^2 - s_{wi}/N)}$  result  $S_B=14.33$  with respective lower confidence limit of 13.6 and upper confidence limit 15.61, with the use of the Cox (1970) method.

These results were compared with the model G proposed by McElhinny and McFadden (1997 generated by global paleomagnetic data set of lava flows exclusively. This database was reanalyzed by Johnson *et al.* (2008) using the bootstrap method under the main assumption that the paleomagnetic field closely approximates with the GAD for the last 5 Myr (see also a simplified statistical model Tk03.GAD by Tauxe and Kent (2004). Our results show a good agreement with the model G proposed by McElhinny and McFadden (1997) (Figure 7) for a latitude of  $\lambda=20^\circ$  and a dispersion of  $S_M=14$  and it is close to the uncertainty limits of the dispersion for the of Johnson *et al.* (2008) model G, with a value of  $S_j=14.8$ , but when compared with the Tk03.GAD model some disagreement is observed since this model predicts a low value of  $S_T=12.9$  with respect to the  $\lambda=20^\circ$  latitude.

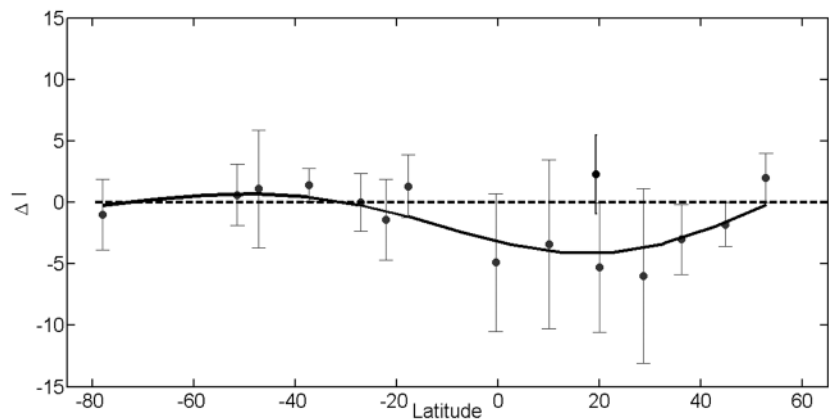


**Figure 6.** Curve of the best fit with respect of the anomalies of the inclination for several latitudes, with the average of the inclinations anomalies (blue dots) and the anomaly inclination of Tancitaro (Black dot).

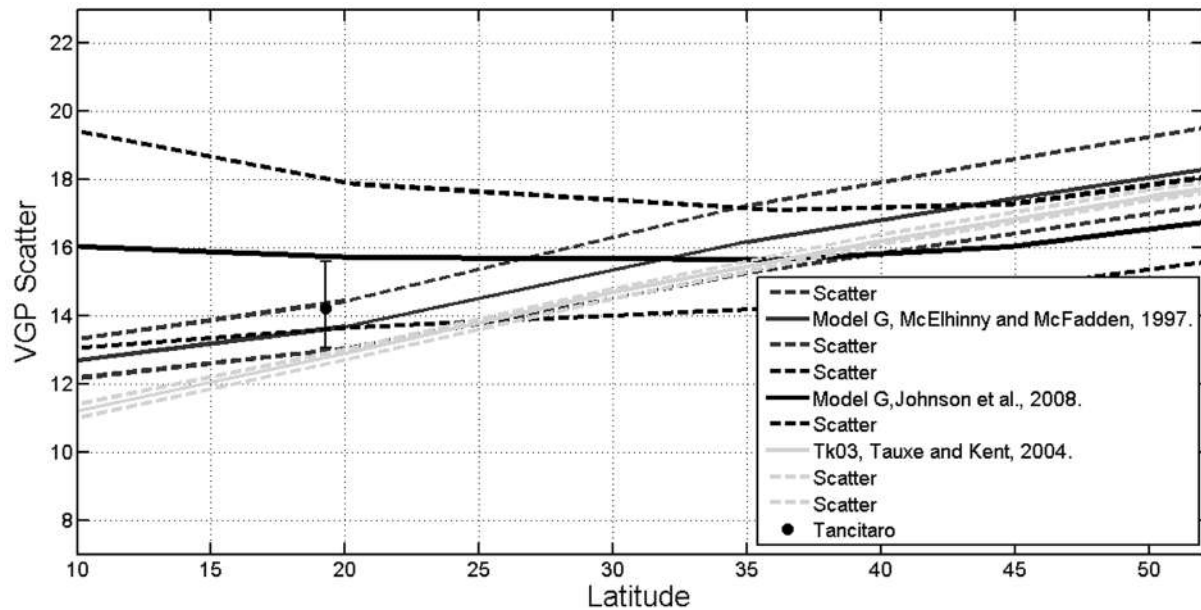


**Figure 7.** Scatter of the VGP as a function of the latitude for the last 5 Myr, compared with the curves of reference provided by the Model G proposed by McElhinny and McFadden (1997) and Johnson *et al.* (2008), also with the Tk03.GAD model of Tauxe and Kent (2004).

For the studies developed around of the TMVB, a dispersion  $S=15.06\pm 0.6^\circ$  and  $S=14.9^{14.8}$  was obtained for studies made by Lawrence and Constable (2006) and Ruiz-Martínez *et al.* (2010) respectively, with dispersion a little bit higher, due the biased to Brunhes Chron.

Two paleodirections obtained on sites Tan-3 and Tan-5 yielded normal polarity paleodirections within reverse polarity Matuyama Chron. They may be erupted during the worldwide observable Jaramillo event (Doell and Dalrymple, 1966; Mankinen and Dalryple, 1979; Laj and Channel, 2007).

Aeromagnetic data of Tancitaro volcano area was obtained by the Mexican Geological Survey (SGM) in 1999, using the following equipment: Islander Airplane BN2-A21; Geometrics magnetometer G-822A optically pumped cesium vapor with sensitivity of 0.001 nT; data acquisition system, Picodas P-101 AG; Base station magnetometer, GEM Systems GSM-19 Overhauser, sensitivity 0.01 nT; Radar altimeter, Sperry RT-220 Navigation system, GPS Ashtech CG24GPS + Glonass, 16m. Flight parameters were: contour flights at a height of 300 m; direction of flight lines North-South; distance between flight lines 1,000 m; distance between control lines (East-West) 10,000 m; electronic navigation (GPS). The data was

initially processed by a digital compilation for correcting the movement plane (magnetic compensation), and daytime drift. From total magnetic field data the International Geomagnetic Reference Field (IGRF, 1995) was subtracted obtaining the Residual Magnetic Field (RMF, Figure 8)

$TMF - IGRF (1995) = RMF$ . The data were leveled using the control lines and microlevelling. All the processes described above were carried out by the SGM.

From the digital aeromagnetic information of the SGM, we plotted the RMF using the Inclination and Declination data means, in order to calculate the Reduced to the Magnetic Pole (RMP, Figure 9) (Baranov and Naudy, 1964). Based on the RMP, the map of the Derivative in the Z direction was calculated (1 order, Figure 10) (Henderson and Ziets, 1949) and the Upward continuations (Henderson, 1970,) among others.

The location of magnetism sources associated with magmatic chambers is based on the analysis of the contour aeromagnetic map (López-Loera, 2002). This analysis consists the identification of normal bipolar magnetic anomaly near or under the volcanic structure. Once the anomaly is identified, the Baranov and Naudy (1964) algorithm (reduced

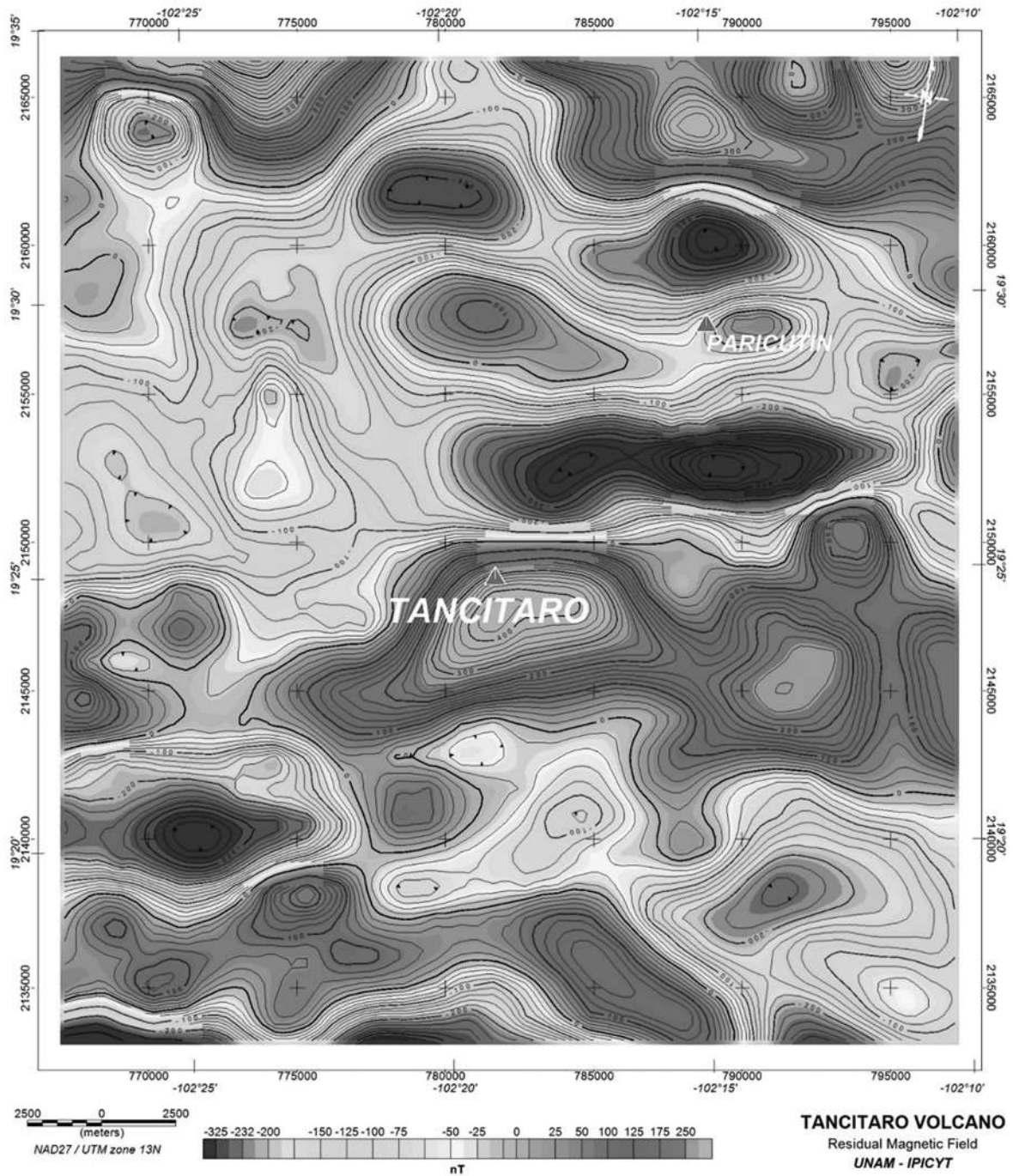


**Figure 8.** Map showing the calculated Residual Magnetic Field (RMF) of the Tancitaro volcano (TV). The RMF map represents the magnetic field strength with isovalue curves in nT and color range, indicating with red the magnetic highs and with blue the magnetic lows. Note the position of the of the TV with respect to the magnetic anomaly.

to magnetic pole) is used in order to locate precisely the anomaly within the studied body. The so called *Fast Fourier Transform* spectral analysis (Blakely, 1995) was used to estimate the depth of the source. This methodology of identification and association of aeromagnetic anomalies with magmatic chambers is based on the fact that the process of cooling of volcanic bodies start from the outside. In this way a crust is formed around the magmatic chamber that allows its identification.

The information processed was configured obtaining the Residual Magnetic Field (RMF, Figure 8). The mean values for the Magnitude in the aeromagnetic survey data (06/1999) was 41,725 nT, the Inclination  $46^{\circ}31'$  and declination  $7^{\circ}45'$ , which means that the RMF anomaly was displaced from the source associated with them. It is a common practice in the processing of aeromagnetic data to use a mathematical algorithm (Baranov and Naudy, 1964) whose application allows to locate the area with respect to the north pole, where the Inclination is  $90^{\circ}$  and the Declination is  $0^{\circ}$  and therefore the magnetism sources will be located below the magnetic anomaly.

Contour map of the RMP shows the existence of zones with different magnetization intensities (different colors in Figure 9). This enables to group them into what is called aeromagnetic domains (AMD), López-Loera, 200 TESIS QUITAR2) that can be associated with rocks having similar magnetic susceptibility values. This means that each AMD is associated with a different geological unit. At a regional scale, the entire study area correlates with one AMD, mainly associated with volcanic rocks. At more local scale three aeromagnetic subdomains (AMSD) can be differentiated as described below.

**AMSD I.** It is located in almost all the study area, it covers the entire central portion and most of the northern side, it is undefined to the E, W and N. It is characterized by the existence of the Tancitaro and Parícutin volcanoes (Figure 9a). It has two large aeromagnetic anomalies (8.8 km x 5 km) elongated in the E-W direction. The anomalies show intensity values of magnetization from 563 to -271.9 nT. One of these anomalies is correlated with the Tancitaro volcano, whose crater is located 1.4 km SW of the center of the aeromagnetic anomaly. In the contour map of the Residual Magnetic Field, this geological structure shows a normal aeromagnetic anomaly with a 5,450

m of polar distance. According to an analysis of Radial Average Spectrum (Figure 10) the host rock of the magma chamber associated with the Tancitaro volcano is located at depths nearly 2 km., and with the method of average width of the anomaly (Figure 11) it is estimated that the host rock of the magmatic chamber is between 2.6 and 3 km. The Tancitaro volcano shows alignments in all direction, which are associated with weakness zones correlated with faults and/or fractures. Topographically this AMSD I, shows altitudes between 2,031 and 3,792 m, with an average of 2,832 m. Its geological association is with rocks of high magnetic susceptibility such as basalts.

**AMSD II.** It is located across the southern part of the study area and is mainly characterized by a series of aeromagnetic anomalies associated with magnetic minima, showing values of magnetization intensity from -96 to -650 nT (Figure 1, Figure 11). It has an "E" lying form and is undefined to the S, E and W. Topographically it shows altitudes from 1,140 to 2,141m, with an average of 1,785 m. It correlates with rocks having a low magnetic susceptibility, such as volcanic breccia and pyroclasts.

**AMSD III.** This subdomain is located towards the NW portion of the studied area, and is undefined to N (Figure 12). It has a form tending to a half circle that shows, in its central portion, an anomaly associated with a magnetic high surrounded by magnetic lows. The values of magnetization intensity are between 197 and -257 nT. Topographically it has altitudes of 1,475 to 2,135 m with an average of 1.780 m. Geologically it correlates with rocks with mean magnetic susceptibilities such as andesitic rocks.

In summary, the aerial magnetometry on the map of Reduce to Magnetic Pole (RMP) shows the existence of three aeromagnetic subdomains all associated with volcanic rocks. The aeromagnetic anomaly associated with the Tancitaro volcano on the map of RMP is shifted 1.4 km to  $50^{\circ}$  NE and has an area of 5 km (N-S) x 8.8 km (E-W) and a magnetization intensity of 710 nT. The depth of the magmatic chamber correlated with the Tancitaro volcano is interpreted between 3.2 km and 5 km and its shape is elongated in the E-W direction. It is limited in all directions by alignments correlated with faults and/or fractures.

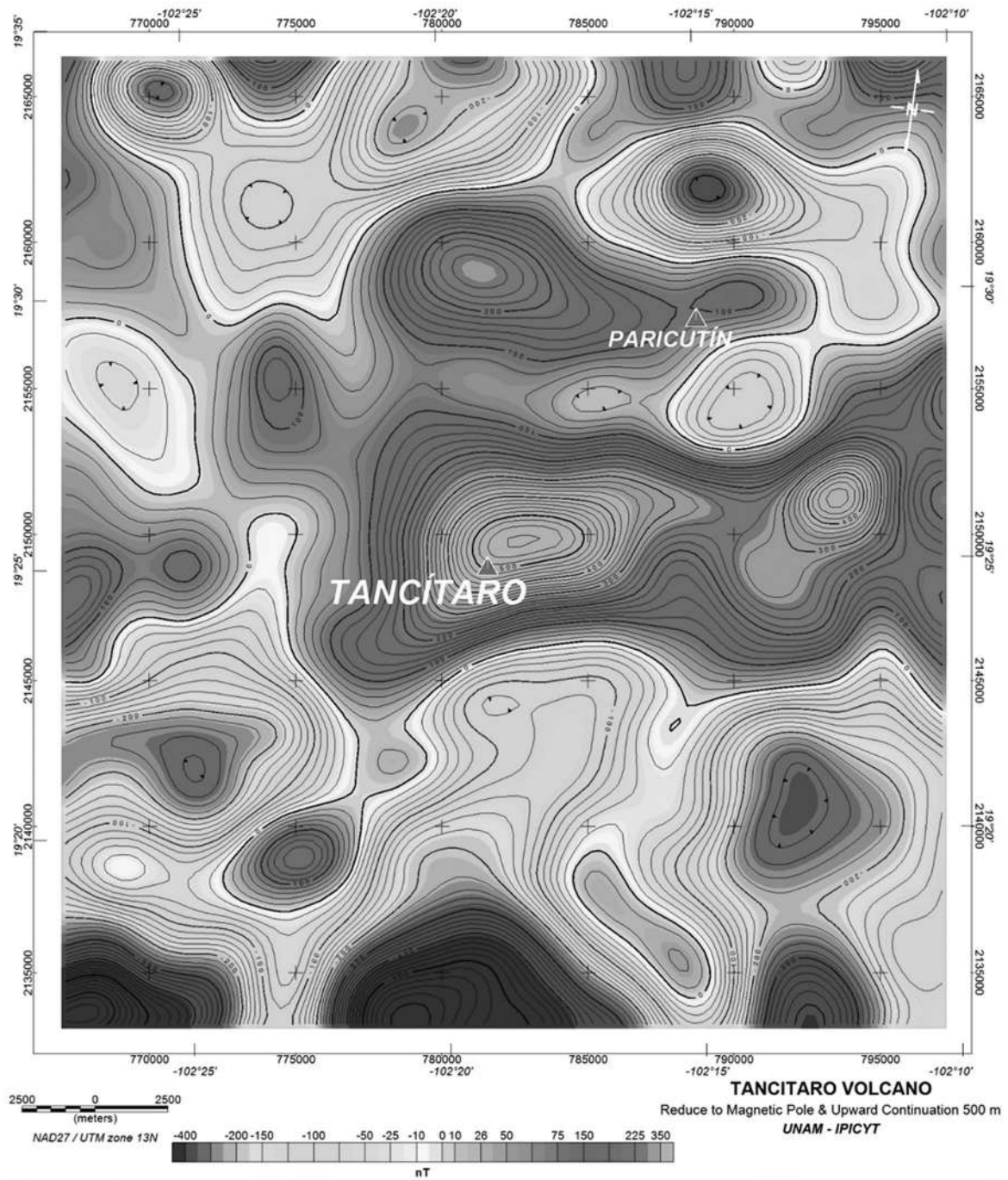


**Figure 9.** Map of the Reduced to Magnetic Pole (RMP) and Upward Continuation 500 m. The RMP map represents how the study area would be observed if it was located in the north pole, were Inclination =  $90^\circ$  and Declination =  $0^\circ$ . Note the position of the TV with respect to the magnetic anomaly. In this RMP the anomalies move to the north.

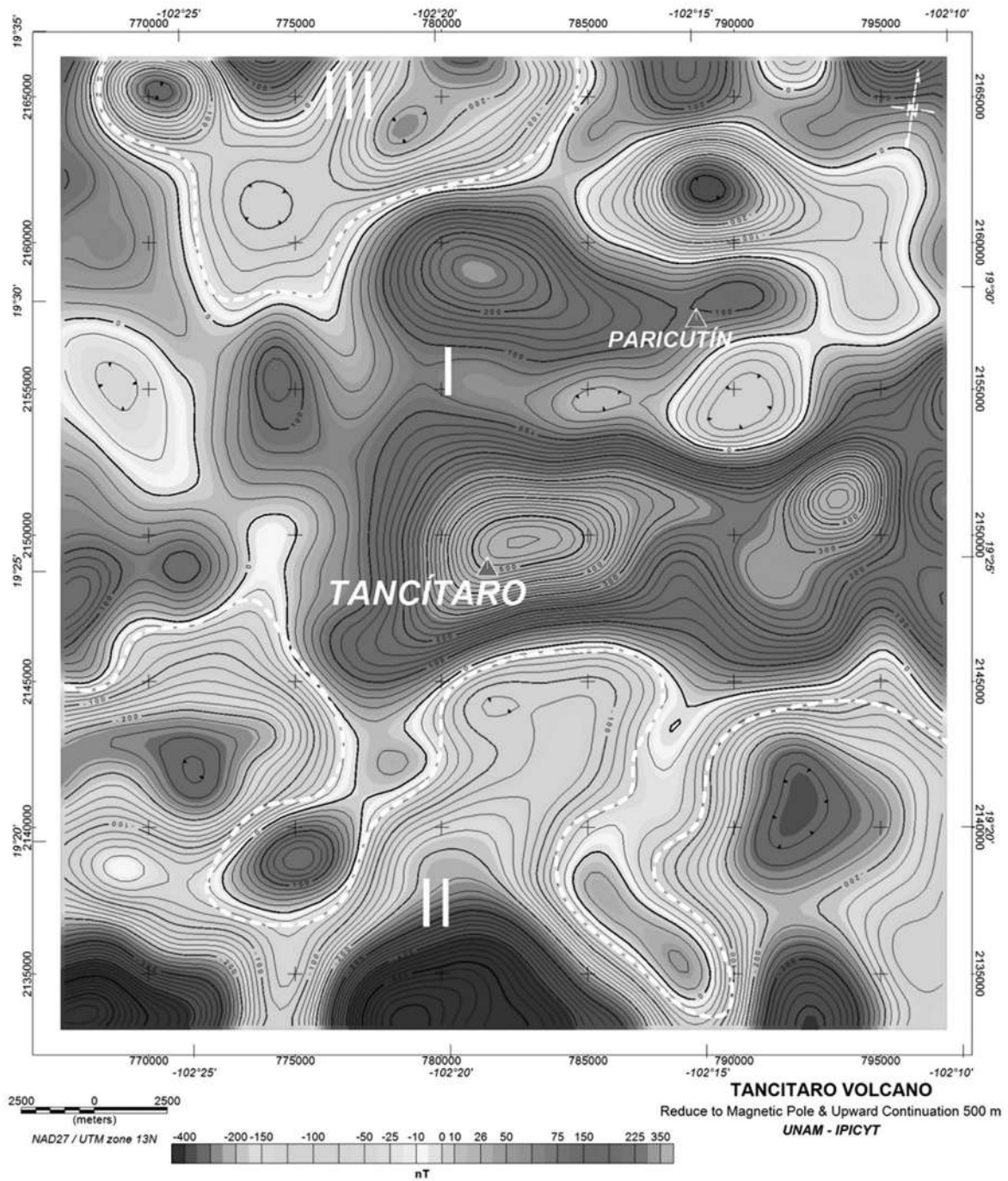


**Figure 9a.** Map of the Reduced to Magnetic Pole (RMP) and Upward Continuation 500 m and aeromagnetic subdomains AMSD (I, II and III) of the Tancitaro volcano (TV) and surrounding areas. The AMSD represents a zone with similar magnetic susceptibility.

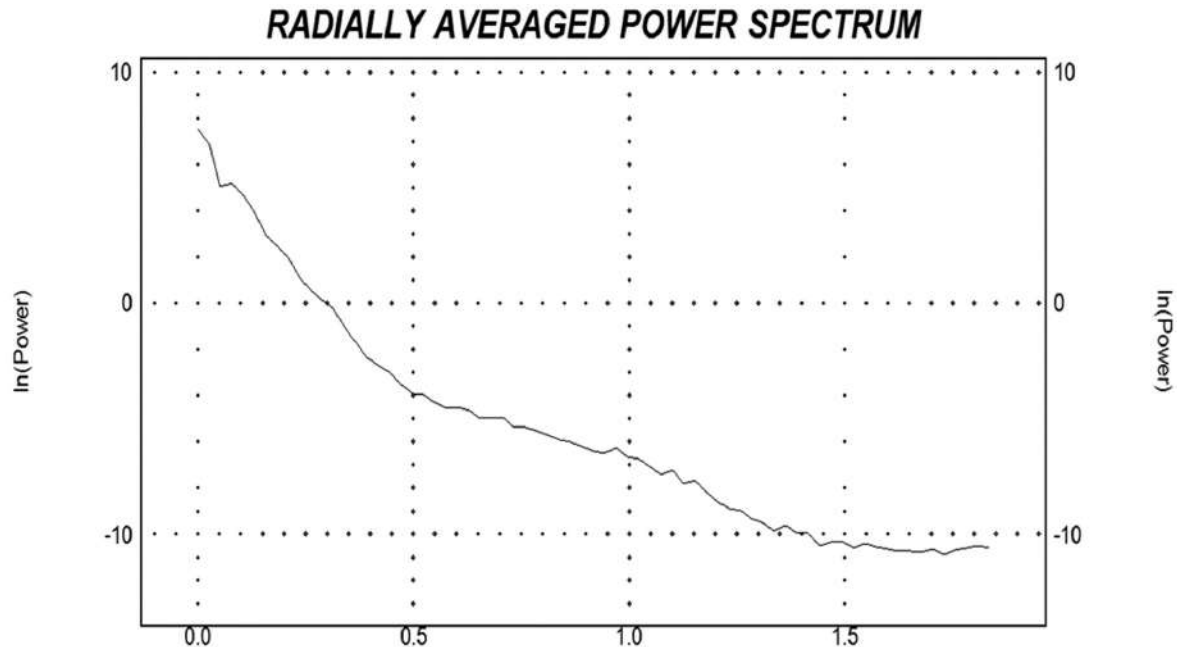


**Figure 10.** The profile represents the Radially Averaged Power Spectrum of the study area.

## Conclusions

A detailed rock-magnetic and paleomagnetic study was carried out on the lava flows associated to the Tancitaro volcano in order to contribute both to the new generation Time Averaged Paleomagnetic Field database and to estimate the latitudinal dependence of the paleosecular variation through the virtual geomagnetic pole scatter. The combined dataset incorporating previously reported paleodirections from the same area offer a detailed record of the Earth's Magnetic Field fluctuation for the last 1 My.

Mean paleodirections was found reasonably close to the Geomagnetic Axial Dipole directions and statistically indistinguishable from the expected directions derived from the stable North America which attest that there is no major tectonic deformations occurred during the last 1 My according to the previous studies. All samples yielded well defined normal polarity magnetization. Two flows are correlated to the Jaramillo polarity event, which provide a useful marker for the volcanic activity in the MGVF.

Combined aeromagnetic survey shows the existence of three magnetic subdomains all associated with volcanic rocks. The aeromagnetic anomaly associated with the Tancitaro volcano on the map of RMP is shifted 1.4km to the Northeast  $50^\circ$  and has an area of 5km (North-South) 8.8km (Est -West) and shows a magnetization intensity of  $710 \text{ nT}$ . The depth of the magmatic chamber correlated with the Tancitaro volcano is interpreted between 3.2km and 5km and the shape is elongated in the East-West direction. It is limited in all directions by alignments correlated with faults and/or fractures, but this could be inside the flows or formed after the events of interest in the geological maps of the Geological National Service, in the paleomagnetic results this relationship was not observed that could be reflected not being near the direction of reference or the GAD.

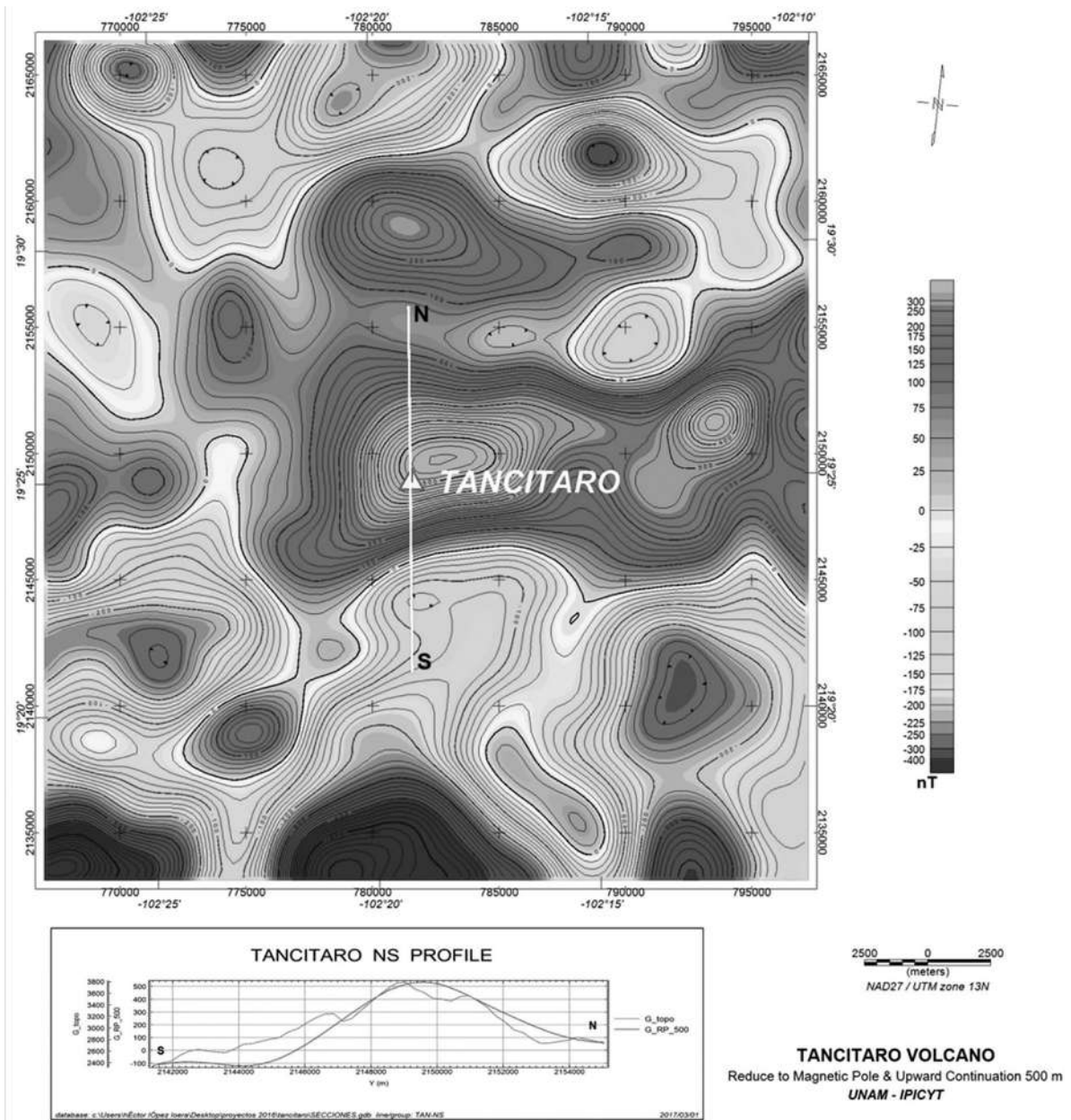


**Figure 11.** The profile observed with NS direction in the map of the RMP & Upward Continuation 500 m; the same as shown in the lower side of the map and that served as base to estimate the depth of the source of the magnetic anomaly with the average width method.

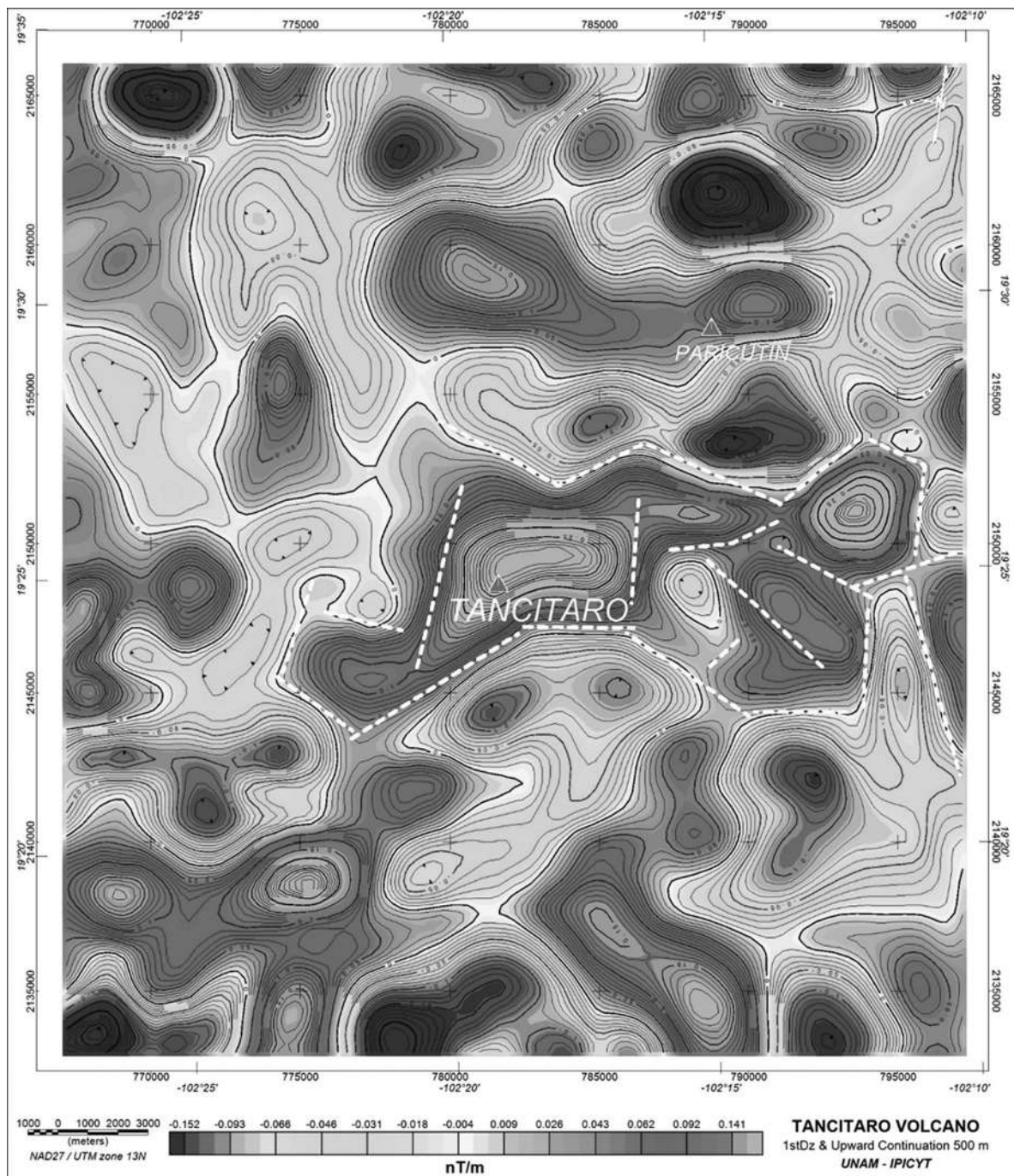


**Figure 12.** First derivative in Z direction and upward continuation 500 m map. This map shows the alignments (white color lines) associated with the anomaly of Tancitaro volcano. This alignments are correlated with faults and/or fractures.

## Acknowledgments

The authors are thankful for the financial support provided by UNAM-PAPIIT IN101717 while some partial funds were provided by CONACYT n° 252149 and 00131191. MC is grateful for the financial support given by UNAM-DGAPA-PAPIIT IA106517.

## References

- Blakely R.J., 1995, Potential theory in gravity and Magnetic applications. Cambridge Univ. Press, p. 441.
- Baranov V., Naudy H., 1964, Numerical calculation of the formula of reduction to the magnetic pole. *Geophysics*, 29, p. 67-79
- Besse J., Courtillot V., 2002, Apparent and true polar wander and the geometry of the magnetic field in the last 200 million years, *J. Geophys. Res.*, 107, B11, 2300.
- Butler R.F, 1991, Paleomagnetism: Magnetic Domain to Geologic Terranes., Book, Blackwell Science.
- Carlut J., Courtillot V., 1998, How complex is the time-averaged geomagnetic field over the past 5 Myr?, *Geophys. J. Int.*, 134, p. 527-544.
- Connor C.B., 1987. Structure of the Michoacán-Guanajuato volcanic field, Mexico. *J. Volcanol. Geotherm. Res.*, 33, p. 191-200.
- Chandra S., Khurshid H., Phan M.H., Srikanth H., 2012, Asymmetric hysteresis loops and its dependence on magnetic anisotropy in exchange biased Co/CoO core-shell nanoparticles, *Appl. Phys. Lett.*, 101, 23, 8-13, doi:10.1063/1.4769350.
- Connor C.B., 1990, Cinder cone clustering in the TransMexican Volcanic Belt: implications for structural and petrologic models. *J. Geophys. Res. Solid Earth*, 1978-2012, 95 B12, p. 19395-19405.
- Cox A., 1970, Confidence limits for the precision parameter k. *Geophys. J. Royal Astronom. Soc.*, 18, p. 545-549.
- Doell R.R., Dalrymple G.B., 1966, Geomagnetic polarity epochs: A new polarity event and the age of the Brunhes-Matuyama boundary. *Science*, 152, p. 1060-1061.
- Dunlop David J., 2002, Theory and application of the Day plot (Mrs/Ms versus Hcr/ Hc) 2. Application to data for rocks, sediments, and soils. *J. Geophys. Res.*, 107, B3, p 2057, doi: 10.1029/2001JB000487.
- Fisher R.A., 1953, Dispersion on a sphere. *Proceedings of the Royal Society of London A*, 217, p. 295-305.
- García-Ruiz R., Goguitchaichvili A., Cervantes-Solano M., Cortés-Cortés A., Morales-Contreras J., Maciel-Peña R., Rosas-Elguera J., Macías-Vázquez J.L., 2016, Secular variation and excursions of the Earth magnetic field during the Plio-Quaternary: New paleomagnetic data from radiometrically dated lava flows of the Colima volcanic complex (western Mexico), *Rev. Mexicana de Cien. Geológ.*, 33, 1, p., 72-80.
- García-Ruiz R., Goguitchaichvili A., Cervantes-Solano M., Morales J., Maciel-Peña R., Rosas-Elguera J., Cejudo-Ruiz R., Urrutia-Fucugauchi J., 2017, Rock-Magnetic and paleomagnetic survey on dated lava flows erupted during the Brunhes and Matuyama chrons: the Mascota Volcanic Field revisited (Western Mexico), *Stud. Geophys. Geod.*, 61, doi: 10.1007/s11200-016-0148-6 (in press).
- Hasenaka T., Carmichael, I.S., 1985, The cinder cones of Michoacán-Guanajuato, central Mexico: their age, volume and distribution, and magma discharge rate. *J. Volcanol. Geotherm. Res.*, 25, p. 105-124.
- Hasenaka T., Ban M., Delgado-Granados H., 1994, Contrasting volcanism in the Michoacán-Guanajuato Volcanic Field, central Mexico: Shield volcanoes vs. cinder cones. *Geophys. Int.*, 33, 1, pp.125- 138.
- Hasenaka T., 1994, Size, distribution, and magma output rate for shield volcanoes of the Michoacán-Guanajuato volcanic field, Central Mexico. *J. Volc. Geot. Res.*, 63, p.13-31.
- Henderson R.G., 1970, On the Validity of the use of Upward Continuation Integral for Total Magnetic Intensity Data. *Geophysics*, 35, 5, 916-919.
- Henderson R.G., Zietz I., 1949, The computation of second vertical derivatives of geomagnetic fields, *Geophysics*, 14, p. 508-516.

- IGRF, 1995, International Geomagnetic Reference Field. *IAGA Division V-Mod, Geomagnetic Field Modeling*.
- Jhonson C.L., Constable C.G., Tauxe L., Barendregt R., Brown L.L., Coe R.S., Lauer P., Mejia V., Opdyke N.D., Singer B.S., Staudigel H., Stone D.B., 2008, Recent investigations of the 0-5 Ma geomagnetic field recorded by lava flows, *Geochem., Geophys., Geosys.*, 4, p. 1525-2027, doi: 10.1029/2007GC001696.
- Kirschvink J.L., 1980, The least-square line and plane and analysis of paleomagnetic data. *Geophys. J. Inter.*, 62, 3, p. 699-718.
- Laj C., Channell, J.E.T., 2007, Geomagnetic excursions, *Treatise on Geophysics, Geomagnetism*, Elsevier, 5, p. 373 - 416.
- Lawrence K.P., Constable C.G., 2006, Paleosecular variation and the average geomagnetic field at latitude., *Geochemistry Geophysics Geosystems, J. Earth Sci.*, 7, 7.
- Leonhardt R., 2006, Analyzing rock magnetic measurements: The RockMagAnalyser 1.0 software, *Computer and Geosciences*, 32, p. 1420-1431.
- López-Loera H., 2002, Estudio de las Anomalías Magnéticas y su relación con las Estructuras Geológicas y Actividad Eruptiva de los Complejos Volcánicos Activos de Colima e Izta-Popocatepetl, México. Tesis Doctoral, Instituto de Geofísica, UNAM. Pp 235.
- Maciel P.R., Goguitchaichvili A., Garduño Monroy V.H., Ruiz Martínez V.C., Reyes Aguilar B., Morales J., Alva-Valdivia L., Miranda Caballero C., Urrutia-Fucugauchi J., 2009, Paleomagnetic and rock-magnetic survey of Brunhes lava flows from Tancitaro volcano, México, *Geophys. Inter.*, 48, 4, pp. 375-384.
- Maciel P.R., Goguitchaichvili A., Marie-Noëlle G., Ruiz-Martínez V.C., Calvo R.M., Siebe C., Aguilar R.B., Morales J., 2014, Paleomagnetic secular variation study of Ar-Ar dated lavas flows from Tacambaro área (Central Mexico): Possible evidence of Intra-Jaramillo geomagnetic excursion in volcanic rocks, *Phys. Earth Planet. Inter.*, 299, p. 98-109.
- Mankinen E.A., Dalrymple G.B., 1979, Revised Geomagnetic polarity time scale for the interval 0-5 m.y.b.p. *J. Geophys. Res.*, 84, p. 615-626.
- Mankinen E., Cox A., 1988, Paleomagnetic investigation of some volcanic rocks from the McMurdo volcanic province, Antarctica, *J. Geophys. Res.*, 93, B10, p. 11599-11612, doi: 10.1029/JB093iB10p11599.
- McElhinny M.W., McFadden P.L., 1997, Paleosecular variation over the past 5 Myr based on a new generalized database. *Geophys. J. Inter.*, 203, 2, 240-252.
- Merril R., McFadden P., 2003, The geomagnetic axial dipole field assumption, *Phys. Earth Planet. Inter.*, 139, p. 171-185.
- Moskowitz B.M., 1981, Methods for estimating Curie temperatures of titanomagnemites from experimental Js-T data., *Earth and Planet. Sci. Lett.*, 53, 1, p. 84-88.
- Ownby S.E., Delgado-Granados H., Lange R.A., Hall C.M., 2007, Volcan Tancitaro, Michoacan, Mexico, 40ar/39ar constraints on its history of sector collapse. *J. Volcanol. Geother. Res.*, 161, 1-2, p. 1-14.
- Ownby S.E., Lange R.A., Hall C.M., Delgado-Granados H., 2010, Origin of andesite in the deep crust and eruption rates in the Tancitaro-Nueva Italia Region of the central Mexican arc., *Geolog. Soc. Am. Bull.*, 123, 1-2, p. 274-294.
- Prévot M., Mankinen E.A., Gromme S.C., Coe R.S., 1985, How the geomagnetic field vector reverses polarity. *Nature*, 316, 6025, p. 230-234.
- Rodríguez-Ceja M., Goguitchaichvili A., Calvo-Rathert M., Morales-Contreras J., Alva-Valdivia L., Rosas E.J., Urrutia F.J., Delgado G.H., 2006, Paleomagnetism of the Pleistocene Tequila Volcanic Field (Western Mexico), *Earth Planets Space*, 58, p. 1349-1358.
- Ruiz-Martínez V.C., Urrutia-Fucugauchi J., Osete M.L., 2008, Palaeomagnetism of the Western and Central sectors of the Trans-Mexican volcanic belt-implications for tectonic rotations and palaeosecular variation in the past 11 Ma, *Geophys. J. Inter.*, 180, p. 577-595, doi:10.1111/j.1365-246X.2009.04447.x.
- Tauxe L., 1998, *Paleomagnetic Principles and Practice*. Dordrecht: Kluwer Academic Publishers.
- Tauxe L., Kent D.V., 2004, *A Simplified Statistical Model for the Geomagnetic Field and*

Detection of Shallow Bias in Paleomagnetic Inclinations: Was the ancient Magnetic Field Dipolar?: *Wiley Online Library*, pp. 101-113.

Torsvik T.H., van der Voo R., Preeden U., Mac Niocail C., Steinberger B., Hinsbergen B., Doubrovine P.V., van Hinsbergen D.J.J., Domier M., Gaina C., Tohver E., Meert J.G., McCausland P.J.A., Cocks L.R.M., 2012, Phanerozoic polar wander, palaeogeography and dynamics, *J. Earth-Science Rev.*, 114, pp. 325-368.

## Evaluation of geochemical data by two different XRF spectrometers in sediments from the Santiaguillo Basin (state of Durango, Mexico)

Jesús David Quiroz-Jiménez and Priyadarsi D. Roy\*

Received: October 17, 2016; accepted: April 28, 2017; published on line: July 01, 2017

### Resumen

La espectrometría de Fluorescencia de Rayos-X (FRX) es uno de los métodos más usados para medir datos geoquímicos y aplica técnicas tanto destructivas como no destructivas en la preparación de muestras. Se evaluó la calidad de 12 diferentes elementos usados comúnmente en la investigación de sedimentos calculando la precisión y exactitud de las concentraciones obtenidas en un espectrómetro portátil de FRX por dispersión en energía (Niton FXL 950), a partir de un método de preparación de muestras no destructivo. Los diferentes modos de medida del espectrómetro y la matriz de las muestras no influyeron significativamente en la precisión, aunque ambos influenciaron los valores de la exactitud. La concentración elemental en sedimentos con textura y matriz variables, colectados de la cuenca de Santiaguillo (estado de Durango, México), medida en el FRX por dispersión en energía mostraron correlaciones positivas altas ( $r \geq 0.8$ ) con respecto a las concentraciones obtenidas en un espectrómetro convencional FRX para Si, Ti, Al, Fe, Mn, Ca, K, Sr y Zr. Las correlaciones bajas para Mg, P, y Rb ( $r \leq 0.7$ ) fueron causadas probablemente por la matriz. Los resultados de elementos con correlaciones altas se corrigieron usando las ecuaciones de regresión lineal entre los datos de ambos espectrómetros.

Palabras clave: fluorescencia de rayos-X, comparación, precisión, exactitud, sedimento, matriz.

### Abstract

XRF spectrometry is one of the commonly used methods to measure geochemical data and it involves both destructive and non-destructive sample preparation techniques. We evaluated data quality of 12 different regularly used elements in sedimentary research by calculating precision and accuracy of data generated in a portable ED-XRF (Niton FXL 950) and by applying a non-destructive sample preparation method. Different measuring modes of the spectrometer and matrix of the samples did not significantly influence the precision but influenced the accuracy. In sediments of variable matrix collected from the Santiaguillo Basin (state of Durango, Mexico), concentrations of Si, Ti, Al, Fe, Mn, Ca, K, Sr and Zr measured using the portable ED-XRF showed strong and positive correlations ( $r \geq 0.8$ ) with concentrations obtained using a conventional WD-XRF. The matrix-effect possibly caused lower correlations ( $r \leq 0.7$ ) for Mg, P and Rb. Concentrations of elements with stronger correlations were corrected using the linear regression equations generated after comparing results of both spectrometers.

Key words: X-ray fluorescence, comparison, precision, accuracy, sediment, matrix.

---

J. D. Quiroz-Jimenez  
Posgrado en Ciencias de la Tierra  
Universidad Nacional Autónoma de México  
Ciudad Universitaria  
Delegación Coyoacán, 04510  
México CDMX, México

P. D. Roy\*  
Instituto de Geología  
Universidad Nacional Autónoma de México  
Ciudad Universitaria  
Delegación Coyoacán, 04510  
México CDMX, México

\*Corresponding author: roy@geologia.unam.mx

## Introduction

In multi-disciplinary research ambits, chemical composition of the geological deposits (e.g. sediment, soil and rock) has a variety of applications. Abundance and mobility of different inorganic elements provide useful information about the source of volcanic products (Roy *et al.*, 2012; Arce *et al.*, 2015), identification of provenance and tectonic settings of sedimentary basin (McLennan, 1989; Armstrong-Altrin *et al.*, 2012; Nagarajan *et al.*, 2014; Zhang *et al.*, 2016), estimation of diagenesis, chemical weathering, physico-chemical conditions of depositional environment (Nesbitt and Young, 1982; Cox *et al.*, 1995; Fedo *et al.*, 1995; El-Shafeiy *et al.*, 2016), and evaluation of the degree of contamination by anthropogenic activity (Kibria *et al.*, 2016; Retama *et al.*, 2016). Inductively coupled plasma mass spectrometry (ICP-MS), scanning electron microscopy (SEM), atomic absorption spectrometry (AAS) and X-ray fluorescence (XRF) spectrometry are some of the techniques that are used to obtain geochemical data. However, XRF spectrometry is relatively economic and quicker compared to all other earlier mentioned techniques and hence it is one of the commonly used methods in geosciences.

In XRF spectrometry, the primary X-rays interact with a sample and generate secondary X-rays (fluorescence) depending upon chemical composition of the geological material. Intensity of this fluorescence is used to determine concentration of different elements present in the sample (Lozano-Santacruz and Bernal, 2005). Presently, XRF spectrometers can measure wavelength or energy of the reflected X-rays and hence they can be grouped as wavelength dispersive XRF (WD-XRF) and energy dispersive XRF (ED-XRF). The conventional or traditional XRF spectrometers (generally WD-XRF) can measure concentrations of a large number of major and minor elements in fused discs and trace elements in pressed pellets. They do not allow recovery of the analyzed samples. However, the portable XRF spectrometers (generally ED-XRF) measure concentration of a limited number of elements in relatively less time. They require smaller amounts of sample and apply simpler preparation techniques. Hence, the samples can be completely recovered for other geochemical and mineralogical analyses.

Over the last couple of decades, several studies were focused on stratigraphic variation of elemental concentrations in sedimentary deposits in order to reconstruct the paleo-environmental conditions of a location or region

(Cheshire *et al.*, 2005; Metcalfe *et al.*, 2010; Roy *et al.*, 2013; Lozano-García *et al.*, 2015; Noble *et al.*, 2016) and also to evaluate the anthropogenic influences in different environments (Ruiz-Fernández *et al.*, 2007; Ontiveros-Cuadras *et al.*, 2014). The temporal variations in elemental contents provide information about varying precipitation/evaporation ratio, strength of aeolian activity, and rate of contaminant inflow. All such research is carried out with sediments recovered through cores and hence the sample size is relatively small. Thus, it is required to reuse the same sample for multiple chemical analyses preferably with application of non-destructive methodologies.

In the present study, we evaluate the data quality of twelve different commonly used elements (Si, Ti, Al, Fe, Mn, Mg, Ca, K, P, Rb, Sr and Zr) in sedimentary research by calculating precision and accuracy of the data generated using a portable ED-XRF (Niton FXL 950). Elemental concentrations were measured in 36 samples of a core collected from the Santiaguillo Basin (state of Durango, Mexico) by two different XRF spectrometers (portable and conventional) that apply two different methodologies (non-destructive and destructive). The main objective is to estimate the difference between data obtained in the portable ED-XRF and conventional WD-XRF using samples of variable matrix (i.e. grain size, texture, carbonate and organic matter content) from the Santiaguillo Basin as a case study.

## Study site and sample

The Santiaguillo Basin (24° 44' N, 104° 48' W, 1960 m asl) is located at foothills of the Sierra Madre Occidental Mountains in the state of Durango. It is present at a distance of ~800 km northwest of Mexico City (Figure 1). Catchment of this basin mainly comprises igneous rocks. Both ignimbrite and rhyolite outcrops are present in the surrounding ~2500-3000 m high mountains (Nieto-Samaniego *et al.*, 2012). Outcrops of andesite and basalt are exposed to the east and west of the basin, respectively. Additionally, the eastern catchment also hosts smaller outcrops of metamorphic and sedimentary rocks (Munguía-Rojas *et al.*, 1998, not seen in Figure 1). Erosion of all the above-mentioned rocks provides sediments to the basin. A total of 36 different samples were selected from a 10.26 m long previously studied sediment core from this basin. Different grain size (i.e. silty-clay, silt, silty-sand, fine-sand, fine-medium-sand and medium-coarse-sand), 0.3-2.0% of organic carbon (OC) and 2.3- 45.5% of calcite

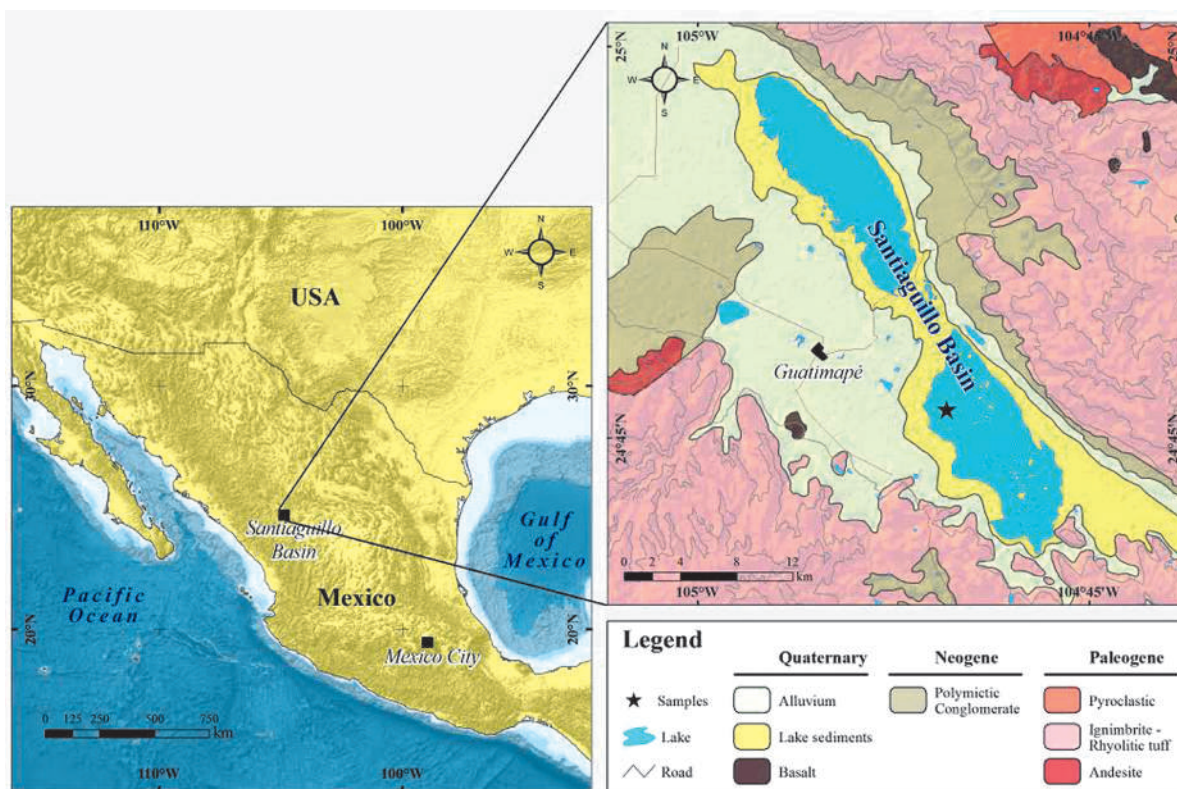


**Figure 1.** Map showing location of the Santiaguillo Basin and geology of the catchment.

( $\text{CaCO}_3$ ) characterize the variable matrix of the samples (Table 1, Quiroz-Jiménez *et al.*, 2017)

### Methodology

Samples were oven dried at  $50^\circ\text{C}$ , homogenized and grounded with an agate pestle till a texture similar to clay was achieved. Concentrations of 12 different elements (Si, Ti, Al, Fe, Mn, Mg, Ca, K, P, Rb, Sr and Zr) were measured in two different XRF spectrometers (i.e. portable Niton FXL 950 and conventional Siemens SRS 3000) following different sample preparation techniques. Three different geological reference materials (SRM-2702, SdAR-M2 and SRM-2709a) were measured only in the portable Niton FXL 950 XRF spectrometer.

#### *Conventional Siemens SRS 3000 XRF*

SRS 3000 is a WD-XRF with X-ray tube made of Rh. Analysis of major and minor elements like Si, Ti, Al, Fe, Mn, Mg, Ca, K and P was carried out using a destructive sample preparation method. It involved mixing 0.8 g dry and powder sediments with 7.2 g of (1:1)  $\text{LiBO}_2$  and  $\text{Li}_2\text{B}_4\text{O}_7$  mixture and this mixture was fused in a Pt/Au (95:5) alloy crisol as per Lozano-

Santacruz *et al.* (1995). Concentrations of trace elements like Rb, Sr and Zr were measured after preparing pressed pellets from the mixture of 4 g of powder sediment and binder following the instructions of Lozano-Santacruz *et al.* (1995) and Verma *et al.* (1996). The loss on ignition was estimated by a gravimetric method after heating 1 g of sample up to  $950^\circ\text{C}$  in porcelain crucible for 1 hour. The measured major elements have precision of <5% and trace elements have precision of <10% (Lozano and Bernal, 2005).

#### *Portable Niton FXL 950 XRF*

Niton FXL 950 is an ED-XRF with a 50 kV X-ray tube made of Ag and a Geometrically Optimized Large area Drift Detector (GOLDD). Analysis of elemental concentration was carried out using a non-destructive sample preparation method. Approximately  $\sim 5$  g dry and powdered sediment was placed in a plastic capsule and it was covered using  $4\ \mu\text{m}$  thick polypropylene X-ray film. Samples were analyzed in three different modes (designed for soil sample and metal enriched mining samples) of the equipment and each mode has different filters (i.e. soil mode: main, high and

**Table 1.** Texture of sediments collected from the Santiaguillo Basin and abundances of organic carbon (OC) and calcite ( $\text{CaCO}_3$ ).

sample	depth (cm)	texture	OC (%)	$\text{CaCO}_3$ (%)
1	40	silt	0.6	12.5
2	56	silty-sand	0.9	9.3
3	66	silt	0.6	13.7
4	106	silty-sand	0.9	7.8
5	126	silt	2.0	18.1
6	136	silty-sand	0.8	12.1
7	204	silty-sand	0.9	9.2
8	244	silty-sand	0.6	9.2
9	274	medium-coarse-sand	0.9	3.2
10	304	silty-sand	0.7	6.8
11	314	silt	0.4	29.4
12	404	silt	0.6	12.5
13	414	silty-clay	1.0	7.7
14	444	fine-medium-sand	0.5	4.1
15	474	fine sand	0.8	11.3
16	494	silty-sand	0.9	6.0
17	504	fine sand	0.8	5.0
18	524	silty-sand	1.0	12.1
19	554	silt	1.0	4.2
20	582	silty-sand	0.9	13.2
21	599	fine sand	0.7	3.3
22	639	fine sand	0.9	2.3
23	659	silty-sand	1.0	17.6
24	679	silt	1.3	4.2
25	696	silty-clay	0.7	5.9
26	726	fine sand	0.3	45.5
27	836	silty-sand	1.2	23.1
28	856	silt	0.6	9.1
29	886	silty-sand	0.6	18.3
30	896	silty-sand	0.5	6.2
31	916	silty-sand	0.7	6.0
32	936	silty-sand	1.3	12.8
33	976	silty-sand	1.3	6.9
34	986	silty-sand	0.9	13.7
35	1006	silty-sand	0.9	5.4
36	1016	silty-sand	0.7	20.1

low range filters; mining Cu/Zn mode: main, high, low and light range filters; mining Ta/Hf: main, high, low and light range filters). We measured each sample for 60 seconds in each filter of the three different modes. Principal difference between the modes is sensibility to different range of elements. For example, the soil mode does not detect lighter elements like Si, Al, Mg and P. However, the mining modes (Cu/Zn and Ta/Hf) can measure all the 12 elements including the lighter elements.

Both the precision and accuracy of the measured elements were determined after measuring elemental concentrations in three different reference materials (SRM-2702, SdAR-M2 and SRM-2709a) in seven repetitions, in all the modes of Niton FXL 950. National Institute of Standards and Technology (NIST) created the reference material SRM-2702 by using inorganic marine sediments and it does not present concentrations of Si, Fe and Zr (NIST, 2016). The United States Geological

Survey (USGS) created SdAR-M2 using metal rich soil (IAG, 2015) and NIST designed SRM-2709a as a reference material for soil, sediment and other geological samples of similar matrix (NIST, 2009).

## Results and Discussion

### Precision (%RSD)

Precision was obtained from Relative Standard Deviation (%RSD) of each element measured in three different reference materials (SRM-2702, SdAR-M2 and SRM-2709a) in three different modes of Niton FXL 950. It was calculated using the formula  $\%RSD=100 \times (s/X)$ , where  $s$  is the standard deviation and  $X$  is the mean concentration of each element in seven repetitions. Soil mode did not measure concentrations of Si, Al, Mg, and P, whereas both the mining modes (mining Cu/Zn and mining Ta/Hf) analyzed concentration of all the 12 different elements (Table 2). Independent of matrix of the reference materials, Mg (%RSD=12-35.2) and P (%RSD=2.4-4.3) were the less precise elements in both the mining modes. Ca (%RSD=0.3-1.4) showed variable values of precision in mining Cu/Zn mode and both Ca (%RSD=0.2-1.9) and Al (%RSD=1.0-2.3) had variable precision in mining Ta/Hf mode. All the other elements had precision of  $\leq 1.1$  in the three different modes of analyses.

Soil mode: Fe (%RSD $\leq$ 0.3) and K (%RSD $\leq$ 0.4) were the most precise elements, whereas Mn (%RSD=1.4-1.8) was comparatively less precise. All other elements (Ti, Ca, K, Rb, Sr, Zr) had %RSD $\leq$ 1.0.

Mining Cu/Zn mode: Si and Fe (%RSD $\leq$ 0.4) were the most precise elements and Mg was the least precise element (%RSD $>$ 12). Compared to Ti, Al, Mn, Ca, K, Rb, Sr and Zr (%RSD $\leq$ 1.4), P (%RSD $>$ 2.9) exhibited less precision.

Mining Ta/Hf mode: In general, precisions calculated in this mode were comparable to precision calculated for mining Cu/Zn mode. Fe (%RSD=0.2) was the most precise element and Mg (%RSD $>$ 15.3) was the less precise. P showed a precision of 2.4 and all other elements had precision of  $<$ 1.9. Al showed relatively lower precision in this mode (%RSD=1.0-2.3) compared to the mining Cu/Zn mode (%RSD=1.0-1.2).

### Accuracy (%ACC)

Accuracy of elements in three different modes of Niton FXL 950 was obtained by calculating  $\%ACC=(X - X_{std} / X_{std}) \times 100$ , where  $X$  is the mean concentration of an element measured in seven repetitions of a geological reference material and  $X_{std}$  is the certified concentration of that element. Table 3 presents certified

**Table 2.** Precision of elements calculated for three different modes of Niton FXL 950. It was estimated from Relative Standard Deviation (%RSD) of elemental concentrations measured in three different reference materials.

element	% RSD = 100 × ( $\sigma/X$ )								
	Soil mode (n=7)			Mining Cu/Zn mode (n=7)			Mining Ta/Hf mode (n=7)		
	SRM-2702	SdAR-M2	SRM-2709a	SRM-2702	SdAR-M2	SRM-2709a	SRM-2702	SdAR-M2	SRM-2709a
Si				0.4	0.3	0.2	0.7	0.5	0.2
Ti	0.3	0.5	0.4	0.6	0.9	0.5	0.5	0.8	0.6
Al				1.0	1.2	1.1	2.2	2.3	1.0
Fe	0.3	0.3	0.2	0.2	0.4	0.3	0.2	0.2	0.2
Mn	1.8	1.7	1.4	0.7	0.6	1.0	1.1	0.9	1.2
Mg				21.8	32.1	12.0	15.3	35.2	16.6
Ca	0.7	0.6	0.3	1.4	1.4	0.3	1.9	1.1	0.2
K	0.4	0.4	0.3	0.6	0.3	0.4	0.8	0.4	0.5
P				2.9	3.0	3.9	2.7	4.3	2.4
Rb	0.6	0.9	0.7	0.6	0.4	0.8	1.0	0.9	1.0
Sr	1.0	0.8	0.6	1.0	0.5	0.5	1.0	0.7	0.6
Zr	0.5	0.4	0.8	0.4	0.8	0.8	0.8	0.7	1.0

values of elemental concentration in 3 different reference materials and accuracy of 12 different elements calculated for three different modes. The positive values indicate overestimation of an element with respect to the certified value and negative values represent underestimation of an element compared to the certified value.

Depending upon the geological reference materials, each element showed different values of accuracy even though the analysis was carried out in the same mode. Mg (%ACC up to 252.5) and P (%ACC up to 264.9) showed the highest error in both the mining modes and soil mode did analyze both the elements. Similarly, both the mining modes reported the exact concentration of Mn as reported in the literature (%ACC=0) for the reference material SdAR-M2.

Soil mode: Ti (%ACC=1.8-24.4), K (%ACC=1.7-15.7), Ca (%ACC=6.7-24.2), Rb (%ACC=4.3-15.5) and Sr (%ACC=1.5-15.4) showed variable accuracy. Depending upon the geological reference material, both Ti (%ACC=24.4; SdAR-M2) and Mn (%ACC=24.5; SRM-2702) were the least accurate elements. Ti and K were the more accurate elements (%ACC<10) in reference material SRM-2702, Rb, Sr and Zr were accurately measured in SdAR-M2 and Ti, Ca, Sr and Zr were the more accurate elements measured in SRM-2709a.

Mining Cu/Zn mode: Both Mg (%ACC=87.9-252.5) and P (%ACC=51.9-138.8) were the least accurate elements. Ti (%ACC=0.7-30.2), Mn (%ACC=0-25.2), Ca (%ACC=5.1-17.9) and Sr (%ACC=2.3-17.5) showed variable accuracy. Si, Fe, Mn, Ca, K, Sr and Zr were accurately measured in SdAR-M2 and Ti, Fe, Mn, Ca, K and Sr were the more accurate elements measured in SRM-2709a. All these elements exhibited %ACC<10 and none of the elements in reference material SRM-2702 showed %ACC<10.

Mining Ta/Hf mode: Both Mg (%ACC=112.4-264.9) and P (%ACC=50.8-138.1) were the least accurate elements. Ti (%ACC=0.9-28.8), Al (%ACC=8.7-28.1), Mn (%ACC=0-24.7) and Sr (%ACC=0.1-16.6) showed variable accuracy. Al was the most accurate element (%ACC < 10) measured in reference material SRM-2702, Si, Fe, Mn, Ca, K, and Sr were measured with less error in SdAR-M2 and Ti, Fe, Mn, Ca, K and Sr were the more accurate elements measured in SRM-2709a.

*Comparison of portable FRX vs. conventional XRF*

Elemental concentrations of sediments collected from the Santiaguillo Basin were measured as a case study and the results obtained both in the portable as well as conventional XRF were compared in order to

**Table 3.** Accuracy of elements calculated for three different modes of Niton FXL 950. Mean of the measured values and certified value of three different geological reference materials are used for the accuracy (%ACC) calculation.

element	certified value			% ACC = 100 × (X - Xstd)/Xstd								
	concentration (%)			soil mode (n=7)			mining Cu/Zn mode (n=7)			mining Ta/Hf mode (n=7)		
	SRM-2702	SdAR-M2	SRM-2709a	SRM-2702	SdAR-M2	SRM-2709a	SRM-2702	SdAR-M2	SRM-2709a	SRM-2702	SdAR-M2	SRM-2709a
Si		35.3	30.3					-5.7	-14.3		-6.6	-14.7
Ti	0.9	0.2	0.3	1.8	-24.4	-5.7	30.2	-13.3	0.7	28.9	-13.1	0.9
Al	8.4	6.0	7.4				10.9	31.2	16.2	8.7	28.1	14.8
Fe		1.8	3.4		-21.6	-11.6		-8.8	-2.8		-8.6	-3.0
Mn	0.2	0.1	0.1	24.5	-18.7	-11.1	25.2	0.0	-3.6	24.7	0.0	-2.3
Mg	1.0	0.3	1.5				87.9	252.5	149.6	112.4	264.9	159.0
Ca	0.3	0.6	1.9	-24.2	-21.4	-6.7	17.9	-5.1	7.0	19.3	-4.1	6.7
K	2.1	4.3	2.1	-1.7	-15.7	-14.4	34.5	-1.1	-4.4	33.3	-0.8	-4.5
P	0.2	0.0	0.1				51.9	138.8	78.9	50.8	138.1	79.4
Rb	0.013	0.015	0.001	-13.1	-4.3	-15.5	-19.9	-11.9	-21.5	-18.5	-11.1	-21.5
Sr	0.012	0.014	0.024	-15.4	1.5	-6.6	-17.5	-2.3	-7.9	-16.6	-0.1	-7.8
Zr		0.027	0.020		-3.5	-7.1		-9.4	-16.4		-14.2	-17.7

evaluate the matrix effect (Figures 2 and 3). Samples were powdered and homogenized in order to remove the texture influence. However, different abundances of organic carbon (OC: 0.3-2.0%) and calcite ( $\text{CaCO}_3$ : 2.3-45.5%) suggest matrix of the sediment samples remained variable even after grinding and homogenizing the bulk samples.

Evaluation of the data obtained with Niton FXL 950 XRF indicates precision of  $<5$  for all the elements except for Mg (%RSD $>12$ ) (Table 2). We did not observe significant influences of either the measuring modes of spectrometer or matrix of the sample on precision. Independent of the mode or matrix, the precision remained homogeneous. For example, Ti had precision of 0.3-0.6 and Ca of 0.7-1.9 in reference material SRM-2702 in all the three different modes. Similarly, Ti (0.3-0.5) and Ca (0.3-0.7) exhibited homogenous precision for all the geological reference materials with different matrix in soil mode. However, the measuring modes as well as matrix influenced the accuracy. Ti had an accuracy of 1.8-30.2 in the reference material SRM-2702 in all the three different modes. Concentration of Ca was underestimated in one mode and overestimated in another mode for the same reference material (Table 3).

Accuracies of Ti (0.7-30.2) and P (51.9-138.8) remained heterogeneous for the different geological reference materials with distinct matrices in the mining Cu/Zn mode.

Except for Mg, P and Rb, all other elements exhibited positive and stronger correlation coefficients between concentrations measured using both the XRF spectrometers. Si, Ti, Al, Fe, Mn, Ca, K and Sr ( $r \geq 0.9$ ) had relatively higher correlations compared to Zr ( $r=0.8$ ) (Figures 2 and 3). Correlation coefficients of Mg, P, and Rb remained  $\leq 0.7$ . In sediments from the Santiaguillo Basin, concentrations of Mg (0.29-1.87 %), P (0.01-0.04 %) and Rb (18-188 ppm) were relatively lower compared to many other elements (e.g. Si and Ca). Lower abundances of Mg, P and Rb might have caused the lower correlations. However, some elements with lower concentrations showed higher correlations. For example, concentrations of Ti and Ca were 0.1% and 0.4% in some samples and both of them exhibited higher correlations. Similarly, Mn (0.01-0.02%) exhibited better correlation compared to P (0.01-0.04%) even though both had comparable concentrations. Thus, we rule out the influence of abundance on different correlation coefficients exhibited by the elements. The non-linearity of X-ray

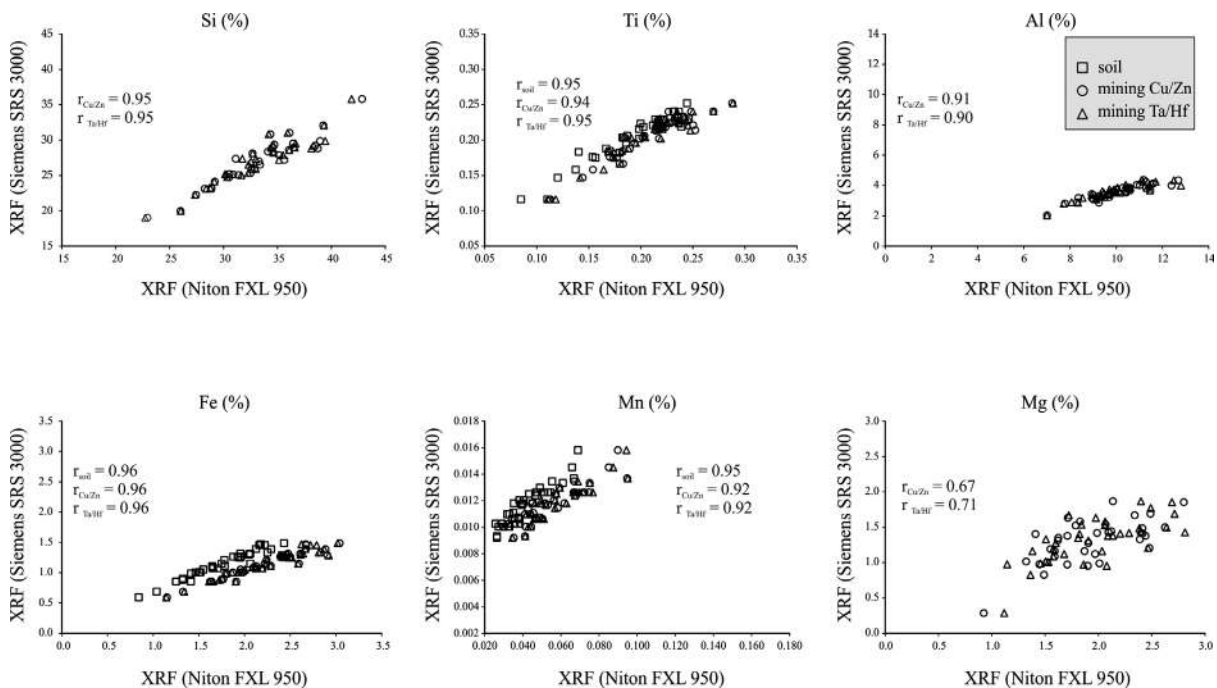


**Figure 2.** Comparison of concentrations of Si, Ti, Al, Fe, Mn and Mg measured in three different modes of portable (Niton FXL 950) and conventional (Siemens SRS 3000) XRF spectrometers.

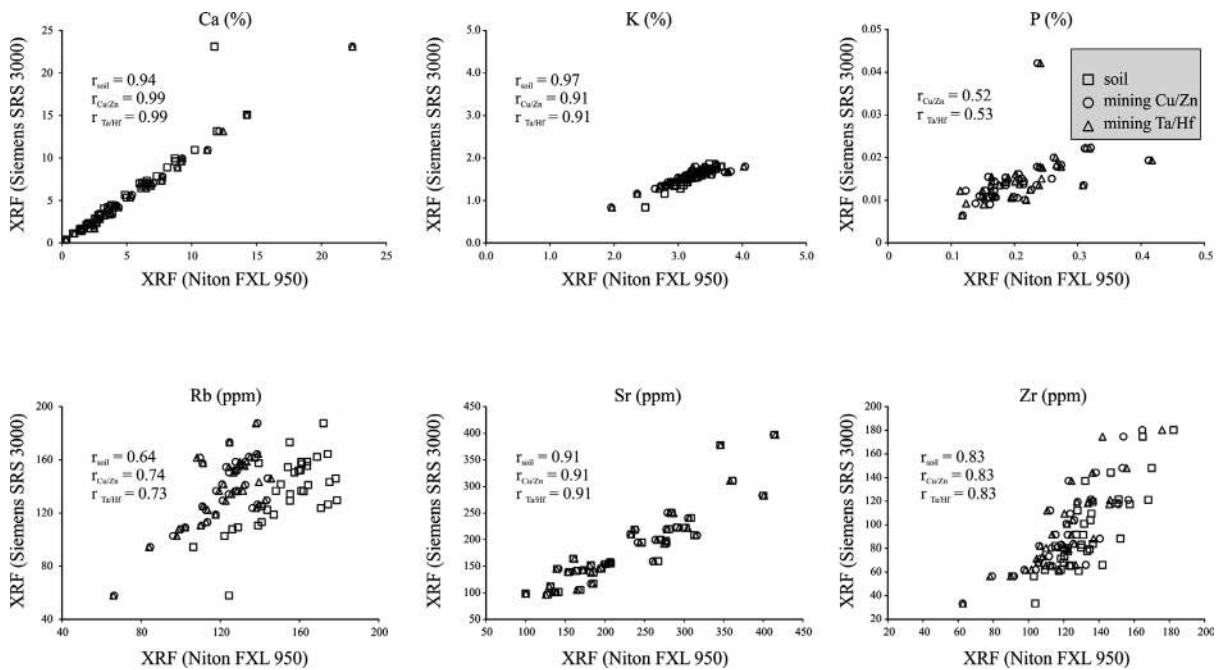


**Figure 3.** Comparison of concentrations of Ca, K, P, Rb, Sr and Zr measured in three different modes of portable (Niton FXL 950) and conventional (Siemens SRS 3000) XRF spectrometers.

intensity with concentration of an element is associated with both absorption and enhancement related to the matrix effect (Birks and Harris, 1962; Mitchell and Kellam, 1968). Based on the characteristics of matrix (lighter, heavy and neutral), X-ray intensity of an element can increase, decrease or remain neutral (Mitchell and Kellam, 1968). Birks and Harris (1962) studied Fe and Cr in a chromite-olivine mineral system and observed that X-ray intensity of Fe decreased as absorption coefficient of Cr increased in a matrix with more Cr compared to Fe.

We estimated the difference between results obtained using both the XRF spectrometers by calculating  $\%change = (X_{FXL} - X_{SRS3000} / X_{SRS3000}) \times 100$ , where  $X_{FXL}$  is elemental concentration in the portable XRF and  $X_{SRS3000}$  is concentration of the same element measured in conventional XRF (Table 4). The portable Niton FXL950 XRF overestimated concentrations of some elements and underestimated concentrations of others compared to the conventional XRF. Positive values represent overestimation of an element in portable XRF (in %) and negative values suggest underestimation of an element (in %) compared to the results of conventional XRF. Irrespective of the sample matrix, estimation of the %change was similar for each element in

both the mining modes. Estimated difference for the soil mode was distinct compared to both the mining modes. For example, Ti was underestimated in the soil mode and overestimated in both the mining modes. Similarly, Rb was overestimated in soil mode and underestimated in both the mining modes. Fe and Zr were overestimated in all the three modes of analysis. However, the soil mode overestimated Fe to a lesser degree and Zr to a higher degree compared to results obtained in both the mining modes.

**Soil mode:** Average values suggest underestimation of Ti (%change=5.2) and Ca (%change=11.2) and overestimation of Mn (%change=246.9) and K (%change=112.1). Concentrations of Fe, Rb, Sr and Zr were overestimated with %Change between 15 and 54.2.

**MiningCu/Zn:** Except for Rb, all other elements were overestimated. Both Ti (%change=1.5) and Ca (%change=0.4) showed the least differences and P (%change=1401.6) exhibited the highest difference. Concentrations of Al, Mn and K (%change=103.6-362.5) were more overestimated compared to Si, Mn, Sr and Zr (%change=24.1-54.6).

Mining Ta/Hf: Differences calculated for this mode is similar to the %change estimated for all the elements in the mining Cu/Zn mode (Table 4). Concentrations of Ti and Ca measured in both the mining modes of the portable XRF were almost similar to concentrations obtained in the conventional XRF. Similarly, the concentration of P obtained in portable XRF was overestimated by almost 14 times with respect to the conventional XRF.

We generated linear regression equation for each element after comparing results obtained in both spectrometers and corrected only the concentrations of elements (Si, Ti, Al, Fe, Mn, Ca, K, Sr and Zr) with stronger correlations ( $r > 0.8$ ). Concentrations of elements (Mg, P and Rb) with lower correlations ( $r \leq 0.7$ ) were not rectified.

## Conclusions

Concentrations of twelve different commonly used elements (Si, Ti, Al, Fe, Mn, Mg, Ca, K, P, Rb, Sr and Zr) in sedimentary research were measured in sediments from the Santiaguillo Basin (state of Durango, Mexico) with variable matrix using a portable ED-XRF (Niton FXL 950) and non-destructive sample preparation technique. This study suggests that concentrations of Si, Ti, Al, Fe, Mn, Ca, K, Sr and Zr can be quickly and economically analyzed in a portable Niton FXL 950 XRF

spectrometer and subsequently corrected. Additionally, the use of non-destructive sample preparation technique can be useful to reuse the same sample for multiple other chemical analyses. The main conclusions of our research are:

Except for Mg and P, all other elements had precisions of  $< 2.3$ . Precision remained homogeneous independently of the measuring mode or matrix. Among the less precise elements, P (%RSD=2.4-4.3) showed better precision compared to Mg (%RSD=12-35.2).

Accuracy was influenced by both the measuring mode as well as matrix. For example, accuracies for Ti (%ACC=0.7-30.2) and P (%ACC=51.9-138.8) were heterogeneous for different geological reference materials with distinct matrices in the mining Cu/Zn mode.

In sediments of the Santiaguillo Basin with variable matrix, concentrations of Mg, P, and Rb measured in the portable XRF exhibited relatively lower correlations for ( $r \leq 0.7$ ) with the results obtained in a conventional XRF. Si, Ti, Al, Fe, Mn, Ca, K and Sr showed higher ( $r \geq 0.9$ ) correlation coefficients compared to Zr ( $r = 0.8$ ). We rule out the influence of abundance on lower correlation coefficients of some elements. However, the variable matrix of sediments might have caused the lower correlations for Mg, P and Rb.

**Table 4.** Estimation of degree of difference (%change) of elemental concentrations of 36 samples from the Santiaguillo Basin measured in portable Niton FXL 950 XRF compared to conventional XRF (Min=minimum, Max=maximum and avg= average).

$$\% \text{ change} = (\text{XFXL950} - \text{xSRS3000} / \text{xSRS3000}) \times 100$$

element	soil mode			Mining Cu/Zn			Mining Ta/Hf		
	Min	Max	Avg	Min	Max	Avg	Min	Max	Avg
Si				11.4	45.8	24.1	10.9	45.5	23.7
Ti	-27.0	9.2	-5.2	-8.8	18.0	1.5	-8.0	15.8	1.6
Al				156.2	244.4	183.4	154.0	244.2	180.8
Fe	41.8	87.4	54.2	81.7	125.9	97.0	78.5	127.1	96.7
Mn	63.1	388.2	246.9	125.3	592.4	362.5	109.0	594.6	362.2
Mg				0.5	223.1	54.6	3.2	290.1	55.9
Ca	-49.1	31.9	-11.2	-21.0	45.7	-0.4	-25.4	47.5	-0.7
K	87.4	197.0	112.1	82.5	133.5	103.6	79.9	134.6	103.4
P				461.3	2184.0	1401.6	471.3	2175.2	1370.0
Rb	-14.9	114.8	15.0	-32.0	14.5	-10.1	-33.1	14.0	-9.6
Sr	-8.5	67.9	26.8	-8.5	63.7	25.7	-8.4	64.7	25.9
Zr	-5.6	210.9	54.1	-11.9	100.8	37.2	-18.7	92.4	36.5

Elements were either underestimated or overestimated in the portable XRF and we used the linear regression equations to reduce difference between results obtained in both the spectrometers. Elements (Si, Ti, Al, Fe, Mn, Ca, K, Sr and Zr) with stronger and positive correlations were rectified. However, concentrations of Mg, P and Rb with lower correlations suffered from the matrix effect and hence were not corrected.

### Acknowledgements

Data generated for this paper formed part of the basic science project (CB-237579) financed by CONACyT. JDQJ was awarded a scholarship from CONACyT (235509) for his doctoral study. This manuscript was drafted during the sabbatical of PDR with a scholarship from DGAPA-UNAM. Jose Luis Sanchez Zavala helped in sample collection and Patricia Girón-García helped in geochemical analysis. Suggestions and comments from both the anonymous reviewers are thankfully acknowledged.

### References

- Arce J.L., Muñoz-Salinas E., Castillo M., Salinas I., 2015, The ~2000yr BP Jumento volcano, one of the youngest edifices of the Chichinautzin Volcanic Field, Central Mexico. *J. Volc. Geoth. Res.*, 308, 30-38.
- Armstrong-Altrin J.S., Lee Y.I., Kasper-Zubillaga J.J., Carranza-Edwards A., Garcia D., Eby G.N., Balaram V., Cruz-Ortiz N. L., 2012, Geochemistry of beach sands along the western Gulf of Mexico, Mexico: implication for provenance. *Chemie der Erde-Geochemistry*, 72, 4, 345-362.
- Birks L.S., Harris D.L., 1962, Unusual matrix effects in fluorescent X-ray spectrometry. *Analyt. Chem.*, 34, 943-945.
- Cheshire H., Thurow J., Nederbragt A.J., 2005, Late Quaternary climate change record from two long sediment cores from Guaymas Basin, Gulf of California. *J. Quat. Sci.*, 20, 5, 457-469.
- Cox R., Lowe D.R., Cullers R.L., 1995, The influence of sediment recycling and basement composition on evolution of mudrock chemistry in the southwestern United States. *Geochimica et Cosmochimica Acta*, 59, 2919-2940.
- El-Shafeiy M., El-Kammar A., El-Barkooky A., Meyers P.A., 2016, Paleo-redox depositional conditions inferred from trace metal accumulation in two Cretaceous-Paleocene organic-rich sequences from Central Egypt. *Marine and Petroleum Geology*, 73, 333-349.
- Fedo C.M., Nesbitt H.W., Young G.M., 1995, Unraveling the effects of potassium metasomatism in sedimentary rocks and paleosols, with implications for paleoweathering conditions and provenance. *Geology* 23, 921-924.
- IAG. International Association of Geoanalysts, 2015. Reference Material Data Sheet, SdAR-M2, Metal Rich Sediment.
- Kibria G., Hossain M.M., Mallick D., Lau T.C., Wu R., 2016, Trace/heavy metal pollution monitoring in estuary and coastal area of Bay of Bengal, Bangladesh and implicated impacts. *Marine pollution bulletin*, 105, 393-402.
- Lozano Santa Cruz R., Verma S.P., Girón P., Velasco F., Morán Zenteno D., Viera F., Chávez G., 1995, Calibración preliminar de Fluorescencia de Rayos-X para análisis cuantitativo de elementos mayores en rocas ígneas. *Actas INAGEQ*, 1, 203-208.
- Lozano Santa Cruz R., Bernal J.P., 2005, Assessment of a new set of geochemical reference materials for XRF major and trace element analysis. *Revista Mexicana de Ciencias Geológicas*, 22, 3, 329-344.
- Lozano-García S., Ortega B., Roy P.D., Beramendi-Orosco L., Caballero, M., 2015, Climatic variability in the northern sector of the American tropics since the latest MIS 3. *Quat. Res.*, 84, 2, 262-271.
- McLennan S.M., 1989, Rare earth elements in sedimentary rocks: influence of provenance and sedimentary processes, in: Lipin, B.R., McKay, G.A. (Eds.), *Geochemistry and Mineralogy of Rare Earth Elements*. *Rev. Mineral.*, 21, 169-200.
- Metcalf S., Jones M.D., Davies S.J., Noren A., Mackenzie A., 2010, Climate variability over the last two millennia in the North American Monsoon region, recorded in laminated lake sediments from Laguna Juanacatlán México. *The Holocene* 20, 1195-1206.
- Mitchell B.J., Kellam J.E., 1968, Unusual matrix effects in X-ray spectroscopy: A study of the range and reversal of absorption enhancement. *Appl. Spect.*, 22, 742-748.

- Munguía-Rojas P., García-Padilla J.L., Armenta-Román R., Cruz-Pérez R., Camacho J. M., Céspedes J.S., 1998, Carta Geológico-Minera, Durango G13-11, escala 1:250000 con texto explicativo. Secretaría de Comercio y Fomento Industrial, Servicio Geológico Mexicano.
- Nagarajan R., Roy P.D., Jonathan M.P., Lozano R., Kessler F.L., Prasanna M.V., 2014, Geochemistry of Neogene sedimentary rocks from Borneo Basin, East Malaysia: Paleo-weathering, provenance and tectonic setting. *Chemie der Erde-Geochemistry*, 74, 139-146.
- National Institute of Standards and Technology NIST, 2009. Certificate of Analysis, Standard Reference Material 2709a, San Joaquin Soil.
- NIST, National Institute of Standards and Technology, 2016. Certificate of Analysis, Standard Reference Material 2702, Inorganics in Marine Sediments.
- Nesbitt H.W., Young G.M., 1982, Early Proterozoic climates and plate motions inferred from major element chemistry of lutites. *Nature*, 299, 715-717.
- Nieto-Samaniego A.F., Barajas-Gea C.I., Gómez-González J.M., Rojas A., Alaniz-Álvarez S.A., Xu S., 2012, Geología, evolución estructural (Eoceno al actual) y eventos sísmicos del Graben de Santiaguillo, Durango, México. *Revista Mexicana de Ciencias Geológicas*, 29, 115-130.
- Noble P.J., Ball G.I., Zimmerman S.H., Maloney J., Smith S.B., Kent G., Adams K.D., Karlin R.E., Driscoll N., 2016, Holocene paleoclimate history of Fallen Leaf Lake, CA., from geochemistry and sedimentology of well-dated sediment cores. *Quat. Sci. Rev.*, 131, 193-210.
- Ontiveros-Cuadras J.F., Ruiz-Fernández A.C., Sanchez-Cabeza J.A., Pérez-Bernal L.H., Sericano J.L., Preda M., Wee Kwong L.L., Páez-Osuna F., 2014, Trace element fluxes and natural potential risks from 210 Pb-dated sediment cores in lacustrine environments at the Central Mexican Plateau. *Sci. Total Environ.*, 468, 677-687.
- Quiroz Jiménez J.D., Roy P.D., Beramendi-Orosco L., Lozano-García S., Vázquez-Selem L., 2017, Orbital-scale droughts in the central-northern Mexico during the late Quaternary and comparison with other subtropical and tropical records. *Geolog. J.*, DOI: 10.1002/gj.2888.
- Retama I., Jonathan M.P., Roy P.D., Rodríguez-Espinosa P.F., Nagarajan R., Sarkar S.K., Morales-García S.S., Muñoz-Sevilla N.P., 2016, Metal concentrations in sediments from tourist beaches of Huatulco, Oaxaca, Mexico: an evaluation of post-Easter week vacation. *Environ. Earth Sci.*, 75, 375.
- Roy P.D., Arce J.S., Lozano R., Jonathan M.P., Centeno-García E., Lozano-García S., 2012, Geochemistry of a tephra-paleosol sequence from north-eastern Basin of Mexico: implications to tephrochronology and chemical weathering during Quaternary. *Revista Mexicana de Ciencias Geológicas*, 29, 24-38.
- Roy P.D., Quiroz-Jiménez J.D., Pérez-Cruz L.L., Lozano-García S., Metcalfe S.E., Lozano-Santacruz R., López-Balbiaux N., Sánchez-Zavala J.L., Romero F.M., 2013, Late Quaternary paleohydrological conditions in the drylands of northern Mexico: a summer precipitation proxy record of the last 80 cal ka BP. *Quat. Sci. Rev.*, 78, 342-354.
- Ruiz-Fernández A.C., Hillaire-Marcel C., Páez-Osuna F., Ghaleb B., Caballero-Miranda M., 2007, 210 Pb chronology and trace metal geochemistry at Los Tuxtlas, Mexico, as evidenced by a sedimentary record from the Lago Verde crater lake. *Chin. J. Geochem.*, 67, 181-192.
- Verma S.P., Lozano-Santa Cruz, R., Girón-García, P., Velasco, F., 1996, Calibración preliminar de Fluorescencia de Rayos-X para análisis cuantitativo de elementos traza en rocas ígneas. *Actas INAGEQ*, 2, 237-242.
- Zhang X., Zhao G., Eizenhöfer P.R., Sun M., Han Y., Hou W., Zhu C.Y., 2016, Tectonic transition from late carboniferous subduction to early Permian post-collisional extension in the eastern Tianshan, NW China: Insights from geochronology and geochemistry of mafic-intermediate intrusions. *Lithos*, 256-257, 269-281.